

Plasma based assembly and engineering of advanced carbon nanostructures

Ana Inês Vieitas de Amaral Dias

► **To cite this version:**

Ana Inês Vieitas de Amaral Dias. Plasma based assembly and engineering of advanced carbon nanostructures. Plasma Physics [physics.plasm-ph]. Université d'Orléans; Universidade técnica (Lisbonne), 2018. English. NNT : 2018ORLE2019 . tel-02436761

HAL Id: tel-02436761

<https://tel.archives-ouvertes.fr/tel-02436761>

Submitted on 13 Jan 2020

HAL is a multi-disciplinary open access archive for the deposit and dissemination of scientific research documents, whether they are published or not. The documents may come from teaching and research institutions in France or abroad, or from public or private research centers.

L'archive ouverte pluridisciplinaire **HAL**, est destinée au dépôt et à la diffusion de documents scientifiques de niveau recherche, publiés ou non, émanant des établissements d'enseignement et de recherche français ou étrangers, des laboratoires publics ou privés.



ÉCOLE DOCTORALE ENERGIE, MATERIAUX, SCIENCES DE LA TERRE ET DE L'UNIVERS
UNIVERSIDADE DE LISBOA, INSTITUTO SUPERIOR TÉCNICO

Laboratoire GREMI UMR 7344, CNRS - Université d'Orléans, France
Instituto de Plasmas e Fusão Nuclear, Instituto Superior Técnico - Universidade de Lisboa,
Portugal

THÈSE EN COTUTELLE INTERNATIONALE présentée par :
Ana Inês VIEITAS DE AMARAL DIAS

soutenue le : 4 Octobre 2018

pour obtenir le grade de :
**Docteur de l' Université d'Orléans
et de l' Universidade de Lisboa - Instituto Superior Técnico**

Discipline : Physique

**PLASMA BASED ASSEMBLY AND ENGINEERING OF ADVANCED CARBON
NANOSTRUCTURES**

THÈSE dirigée par :

M. BERNDT, Johannes	[Chercheur CDI – HDR – GREMI UMR 7344, CNRS / Université d'Orléans]
Mme. TATAROVA, Elena	[Chercheuse avec Habilitation – Instituto Superior Técnico / Universidade de Lisboa]
M. HENRIQUES, Júlio	[Chercheur – Instituto Superior Técnico / Universidade de Lisboa]

RAPPORTEURS :

M. CVELBAR, Uros	[Associate Professor – Jozef Stefan Institute, Slovenia]
M. TEODORO, Orlando	[Associate Professor – Faculdade de Ciências e Tecnologia / Universidade Nova de Lisboa]

JURY:

M. LEMOS ALVES, Luís	Full Professor – Universidade de Lisboa, Portugal Président du jury
M. CVELBAR, Uros	Professeur – Jozef Stefan Institute, Slovenia
Mme. KOVACEVIC, Eva	Professeure des Universités - GREMI UMR 7344, CNRS / Université d'Orléans
Mme. BOULMER-LEBORGNE, Chantal	Professeure des Universités – Université d'Orléans
M. Soares GONÇALVES, Bruno Miguel	Chercheur – Universidade de Lisboa, Portugal
Mme. TATAROVA, Elena	Directeur de Recherche – Universidade de Lisboa, Portugal
M. TEODORO, Orlando	Professeur Associé à Service Temporaire – Universidade Nova de Lisboa, Portugal



**UNIVERSIDADE DE LISBOA
INSTITUTO SUPERIOR TÉCNICO
UNIVERSITÉ D'ORLÉANS
ÉCOLE DOCTORALE DE ENERGIE, MATERIAUX,
SCIENCES DE LA TERRE ET DE L'UNIVERS**

**Plasma based assembly and engineering of advanced carbon
nanostructures**

Ana Inês Vieitas de Amaral Dias

Supervisors: Doctor Elena Stefanova Tatarova
Doctor Júlio Paulo dos Santos Duarte Vieira Henriques
Doctor Johannes Ernst Helmut Berndt

**Thesis approved in public session to obtain the
PhD Degree in Technological Physics Engineering**

Jury final classification: Pass with Distinction and Honour

2018



**UNIVERSIDADE DE LISBOA
INSTITUTO SUPERIOR TÉCNICO
UNIVERSITÉ D'ORLÉANS
ÉCOLE DOCTORALE DE ENERGIE, MATERIAUX, SCIENCES DE LA
TERRE ET DE L'UNIVERS**

Plasma based assembly and engineering of advanced carbon nanostructures

Ana Inês Vieitas de Amaral Dias

Supervisors: Doctor Elena Stefanova Tatarova
Doctor Júlio Paulo dos Santos Duarte Vieira Henriques
Doctor Johannes Ernst Helmut Berndt

**Thesis approved in public session to obtain the
PhD Degree in Technological Physics Engineering
Jury final classification: Pass with Distinction and Honour**

Jury:

Chairperson: Doctor Luís Paulo da Mota Capitão Lemos Alves Instituto Superior Técnico,
Universidade de Lisboa

Members of the committee:

Doctor Eva Kovacevic GREMI UMR 7344, CNRS/Université d'Orléans, France
Doctor Chantal Boulmer-Leborgne GREMI UMR 7344, CNRS/Université d'Orléans, France
Doctor Uroš Cvelbar Jozef Stefan Institute, Slovenia
Doctor Orlando Manuel Neves Duarte Teodoro Faculdade de Ciências e Tecnologia,
Universidade Nova de Lisboa
Doctor Bruno Miguel Soares Gonçalves Instituto Superior Técnico, Universidade de Lisboa
Doctor Elena Stefanova Tatarova Instituto Superior Técnico, Universidade de Lisboa

Funding Institutions

Fundação para a Ciência e Tecnologia

2018

Resumo

Os plasmas são um ambiente único que permite a criação de materiais inovadores e o melhoramento de materiais já existentes que, de outra forma, não seriam alcançáveis. O potencial do plasma deriva de sua capacidade de fornecer simultaneamente elevados fluxos de partículas carregadas, moléculas quimicamente ativas, radicais, calor, fótons que podem influenciar fortemente os mecanismos que induzem a criação das nanoestruturas à escala atômica.

Nesta tese de doutoramento, métodos baseados em plasmas de micro-ondas foram usados para a síntese de nanomateriais de carbono complexos, nomeadamente grafeno, N-grafeno e estruturas tipo diamante.

Deste modo, um dos principais objetivos desta tese consistiu na otimização do processo de síntese de nanoestruturas de carbono 2D, tais como grafeno e N-grafeno, através da elaboração e aperfeiçoamento do método baseado em plasmas de micro-ondas desenvolvido no *Plasma Engineering Laboratory* (PEL). O processo de produção a grande escala de grafeno de alta qualidade, usando plasmas de ondas de superfície a pressão atmosférica com mistura de árgon-etanol, foi alcançado com sucesso.

Além disso, N-grafeno foi produzido usando dois métodos diferentes, método direto (processo com uma única etapa) e indireto (processo de duas etapas). Para a síntese de N-grafeno pelo método direto, adicionou-se azoto à mistura de árgon-etanol. Por outro lado, para o processo de duas etapas, as folhas de grafeno previamente sintetizadas foram expostas a um tratamento de plasma de árgon-azoto a baixa pressão. Os átomos de azoto foram incorporados com sucesso na estrutura hexagonal do grafeno, formando principalmente ligações “pyrrolic”, “pyridinic” e “quaternary”. Um nível de dopagem de cerca de 25 at.% foi alcançado.

Diferentes tipos de nanoestruturas de carbono, incluindo grafeno e estruturas tipo diamante, foram sintetizados usando metano e dióxido de carbono como precursores de carbono num plasma de árgon.

Adicionalmente, plasmas capacitivos de radiofrequência também foram usados para a funcionalização de grafeno e síntese de nanocompósitos, i.e. compósitos poliméricos de polianilina (PANI) - grafeno. Possíveis aplicações destes materiais foram estudadas e ambos mostraram características promissoras para o respetivo uso em biossensores.

Palavras chave:

Nanoestruturas de carbono, Plasmas de baixa temperatura, nanocompósitos polímero-grafeno, Nanodiamante, Grafeno.

Acknowledgements

Firstly, I would like to express my sincere gratitude to my supervisor Elena Tatarova, who guided and supported me along the whole project, without whom this work would not be possible to accomplish.

I would also like to extend my appreciation to my two other supervisors Júlio Henriques and Johannes Berndt. Thank you Júlio for all the support and useful discussions and for your contribution with the theoretical model results for the chapter, and article, concerning N₂-Ar plasma post treatment of graphene sheets as well as N-doped graphene direct synthesis. Thank you to my supervisor Johannes Berndt for all his support and guidance specially in the secondment year that I worked in GREMI, for all the good discussions on finding ways to use graphene for several applications, specially by functionalizing it and synthesising graphene-polymer nanocomposites.

I would like also to thank my PhD committee members Luís Lemos Alves, Eva Kovacevic, Chantal Boulmer-Leborgne, Uros Cvelbar, Orlando Teodoro, Bruno Gonçalves as well as Elena Tatarova, my supervisor, for accepting to be part of the committee, reading the thesis and participating in the defence ceremony.

I would like to give a special thanks to APPLAuSE governing board for the given opportunity to participate in this broadened doctoral program that allowed me to develop this outstanding hot topic both in IPFN (Instituto de Plasmas e Fusão Nuclear), at IST (Instituto Superior Técnico), Portugal, and in GREMI (Groupe de Recherches sur l'Energétique des Milieux Ionisés), at Université d'Orléans, France.

This PhD thesis was carried out in the framework of a co-tutelle protocol between Universidade de Lisboa and Université d'Orléans. Thus, I would like to thank both parties and all of those involved for their agreement in joining this collaboration and for their engagement and commitment in making it possible. I would also like to thank Júlia Oliveira for helping me, by answering all the questions that I had concerning the co-tutelle protocol.

I would like to acknowledge my colleagues from the Plasma Engineering Laboratory from N-PRiME group, in IPFN. Thank you to Marques Dias and Inácio Dionísio for the valuable help at the laboratory, mainly in the experimental setup conception. I would like to acknowledge my colleagues Neli Bundaleska and Edgar Felizardo for your help specially when I was in my

secondment year abroad. Neli thanks for your contributions in papers and chapters, especially in the obtained results concerning the direct synthesis of doped graphene. Edgar thanks for your help specially in the obtained results concerning the chapter that covers the diamond-like structures formation.

Furthermore, I would like also to acknowledge the members of GREMI for welcoming me so well in your group. My gratitude to Eva Kovacevic for the helpful collaboration, for extremely important guidance and huge support during the secondment year abroad, where I had the opportunity to work with a capacitively coupled plasma used for graphene functionalization and monomers polymerization. Thanks for all the great discussions about different material diagnostics that I learned how to use and analyse the outcoming data, specially the discussions that we had about NEXAFS results which I was fortunate to perform in Bessy II under your supervision. I would also like to acknowledge Cedric, Shahzad, Agnes, Ramzi, Hervé, Nadjib, Arnaud, Philippe, Olivier and Chantal for their helpful contribution while I was working in the lab, for all the background given concerning several material and plasma diagnostics that I worked with. Sylvie and Corinne, thank you for welcoming me so well and for all the administrative and personal support that you gave me.

I would like to extend my appreciation to all the collaborators and co-authors. Thanks to D. Tsyganov for his contribution with the theoretical model results for the chapter, and article, concerning hydrocarbons decomposition process in microwave argon plasmas. Thank you to T. Strunskus for his support while I was performing NEXAFS and XPS analysis at synchrotron Bessy II in HZB, Germany. Thank you to U. Cvelbar for his contribution in HRTEM diagnostic, to A. Rego, A. Ferraria, N. Bundaleski and O. Teodoro for XPS, to C. C. Luhrs and J. Phillips for HRTEM and SEM, to I. Nogueira for SEM, A. Almeida for XRD and M. Abrashev for Raman spectroscopy.

A very special thanks to Carla Reis, Anabela Gonçalves and Carmo Nunes, for always taking good care of me. You have been a great support in the past four years.

This work was funded by the Portuguese FCT—Fundação para a Ciência e a Tecnologia, under Project UID/FIS/50010/2013 (PD-F APPLAuSE) and partially supported by French National Research Agency through the project ANR PlasBioSens. This work was also partially supported by PEGASUS (Plasma Enabled and Graphene Allowed Synthesis of Unique nano Structures)

project. PEGASUS project is funded by European Union's Horizon research and innovation programme under grant agreement No. 766894.

I would also like to thank my friend Susana Espinho for the partnership, which has started in my final year of master student and continued in this journey that I took when we entered in APPLAuSE doctoral program. Thanks a lot for all the laughs and good discussions that we had. I would also like to extend this acknowledgement to my colleagues from the first cohort of APPLAuSE, Jayanath, João, Norberto, Diogo, Shah and Alex for all the great and fun gatherings that we had. I am rooting for your success.

Last but not the least, I would like to thank my family and friends. *Gostaria de agradecer à minha família, especialmente à minha mãe Maria Isabel Pereira Vieitas e ao meu pai António José Amaral Dias, e amigos pelo apoio incondicional que sempre me deram durante toda a minha vida e por sempre acreditarem em mim. Especialmente durante estes últimos anos, obrigada pelo vosso amor e carinho e pelos momentos que passámos juntos (infelizmente não tão frequentes quanto o desejado) recheados de períodos de descontração, reflexão, bom humor e claro de grandes gargalhadas, que nos é característico.*

Index

Chapter I.	Introduction	1
I.1.	Motivation.....	1
I.2.	Objectives.....	2
I.3.	Main Contributions	5
I.4.	Dissertation Outline	11
I.5.	State of the Art.....	13
I.5.1.	Graphene.....	14
I.5.2.	Doped and functionalized graphene	24
I.5.3.	Nanodiamonds.....	27
I.6.	Material characterization techniques.....	35
I.6.1.	SEM and TEM.....	35
I.6.2.	SAED	35
I.6.3.	X-Ray.....	36
I.6.4.	Raman.....	39
I.6.5.	FTIR.....	39
Chapter II.	Experiments, results and discussion	43
II.1.	Microwave plasma-based method used for 2D and 3D carbon nanostructures synthesis	43
II.1.1.	Mass production of high-quality free-standing graphene and N-graphene sheets using an Argon-Ethanol microwave plasma.....	49
II.1.2.	Synthesis of complex carbon structures using different precursors	73
II.2.	N-doping of graphene using a Ar-N ₂ microwave remote plasma treatment.....	92
II.2.1.	Experimental setup	92
II.2.2.	Plasma characterization	94
II.2.3.	Material characterization	98
II.2.4.	Summary.....	115

II.3. Graphene applications using plasma-based methods	117
II.3.1. Samples preparation for plasma treatment/polymerization	118
II.3.2. Polymer-graphene nanocomposites using a plasma polymerization method.....	124
II.3.3. Graphene functionalization for biosensing applications.....	129
Chapter III. Conclusions.....	137
References	143
List of Abbreviations.....	173

Chapter I. Introduction

I.1 - Motivation

I.2 - Objectives

I.3 - Main Contributions

I.4 - Dissertation Outline

I.5 - State of the Art

I.5.1 - Graphene

I.5.2 - Doped and functionalized graphene

I.5.3 - Nanodiamonds

I.6 - Material characterization techniques

I.6.1 - SEM and TEM

I.6.2 - SAED

I.6.3 - X-Ray

I.6.4 - Raman

I.6.5 - FTIR

I.1. Motivation

A critical requirement for mass production is the control on the processes of synthesis and engineering of targeted nanostructures, such as rigid control on the number of atomic monolayers and their structural qualities. To this end, knowledge about methods of synthesis is essential because the final properties strongly depend on the assembly pathway. So far, the most well-known and used methods for 2D materials synthesis, include mechanical and chemical exfoliation that are common methods used to separate individual sheets from stacked 2D layered crystals by breaking weak van der Waals bonds between layers, surface segregation, and chemical vapor deposition (CVD), among others[1]. However, these techniques present several drawbacks such as degradation of nanostructure properties due to interference from transition metal catalysts, very high processing temperatures, lengthy and complex synthesis procedures, use of hazardous chemicals, and importantly the quite limited control on the assembly process [2]. In this respect, low-temperature and catalyst-free synthesis are highly desirable for practical applications. Plasma-based technology has evolved as one of the most promising innovative technologies for synthesis and engineering of complex materials. Plasma environments constitute powerful tools in materials science by allowing the creation of innovative materials and the enhancement of long existing materials that would not otherwise be achievable. The outstanding capabilities of plasma-based processes are widely recognised [3]–[6]. The remarkable plasma potential derives from its ability to simultaneously provide dense fluxes of charged particles, chemically active molecules, radicals, heat, photons and electric fields in sheath domains, which may strongly influence the assembly pathways across different temporal and space scales, including the atomic ones. The unique chemically active plasma environment provides suitable conditions to dissociate/atomize molecules in order to synthesize extraordinary 2D nanostructures in a way that no other techniques are able to reproduce.

Using graphene as a starting point, new isolated atomic planes can be assembled and reassembled into designed nanostructures. Given the uniqueness of 2D structures one may expect that such materials will reveal new and unexpected extraordinary properties, providing a number of innovative opportunities. Graphene, one-atom-thick layer of sp^2 hybridized carbon tightly packed into a 2D hexagonal lattice structure, has attracted strong interest from academia and industry

due to its unique physical properties and high application potential in many fields, such as energy storage and conversion devices, sensors, electronics, composite materials etc [2], [7]–[13]. Additionally, graphene can be considered as an atomic-scale scaffold, on the basis of which new 2D crystals can be created. Successful doping of graphene with nitrogen, denominated as N-graphene, was already demonstrated [2], [8], [9], [11], [14]–[18]. It is noteworthy that nitrogen functional groups covalently attached to the graphene scaffold and the specific properties of graphene lead to an extraordinary electrochemical performance [2], [8], [11].

Applications of N-graphene in direct electrochemistry of glucose oxidase and glucose biosensing were studied by Wang et al[19]. The promising potential of N-graphene as counter electrode for dye-sensitized solar cells (DSSCs) was demonstrated by Yang’s group[20]. Three times higher energy conversion efficiency for N-graphene as counter electrodes in DSSCs than for pristine graphene (PG) was obtained. N-graphene as well as polymer-graphene nanocomposites have shown great potential for energy conversion and storage applications, and in particular for supercapacitors and electrochemical biosensors, due to its extraordinary mechanical, thermal, electrical, optical, and chemical properties[21], [22]

The work presented in this thesis relies on optimizing the 2D carbon nanostructures production by further elaboration of the microwave-plasma based method[3], [4], [23] for graphene synthesis developed in PEL. Graphene functionalization and doping is one of the main objectives of this thesis, being the focus in fabrication of N-doped graphene. Moreover, in this work very interesting advancements have been done on finding a plasma method able to synthesize graphene-based nanocomposites, in order to subsequently use them in a wide range of applications, including biosensing [24], [25] and coating inks [26], [27].

I.2. Objectives

The work presented in this thesis results from a combination of plasma physics and materials science.

One of the main goals of this work lies on further betterment of the plasma-based method for free-standing graphene synthesis that has been already developed in PEL [3], [4], [23]. The novelty of plasma approach used is based on the process scale-up using large-scale configuration of wave driven microwave discharges and complimentary engineering to control morphologies and

structural qualities of targeted nanostructures via synergistic tailoring of the plasma environment and the “cold” outlet gas flow, where in-situ infrared (IR) and ultraviolet (UV) radiation are applied. The possibility to tune the density and energy of the building units, i.e., C₂ radicals and C atoms, in the high energy-density plasma environment, which translates in an effective control over the energy and material fluxes towards growing nanostructures in the assembly zone of the reactor, constitutes the most crucial advantage of this method. The plasma properties have been tailored to achieve selective synthesis of free-standing graphene and N-graphene sheets.

The second part of this work was focused on the understanding of the plasma processes for the synthesis of different 2D and 3D carbon nanostructures, like graphene, carbon-onions and nanodiamonds, using different precursors such as methane, and methane gas mixtures with hydrogen and carbon dioxide. For this propose the method mentioned before was applied. Further investigation on the influence of the gas temperature spatial profile, gas flow and type of precursors was performed. Complex numerical models along with in-situ plasma techniques were performed to tune particles and energy fluxes to optimize the synthesis process.

The third part of the work is focused on N-graphene synthesis, where an innovative microwave N₂-Ar plasma treatment at reduced pressure conditions is used. Experimental and theoretical investigation of fundamental physical issues in what concerns the control of the nitrogen dissociation degree was carried out.

The last part of the project will be focused on finding a way to use graphene in a variety of applications. For that purpose, materials such as graphene-polymer nanocomposites, as well as functionalized graphene were synthesised by means of a capacitively coupled RF plasma (CCP) in GREMI/CNRS facilities. In this case plasma diagnostics such as Mass spectrometry, in-situ FTIR and Microwave interferometry were used to better understand the film deposition phenomena over graphene, as well as thin film diagnostics, including near edge x-ray absorption fine structure (NEXAFS) and X-ray photoemission spectroscopy (XPS), among other material characterization techniques to analyse the morphology as well as the elemental composition of the produced nanocomposites.

It was also important to perform visible and infrared spectroscopy to detect the different species radiation as a measure of precursor species densities and measurements of the main plasma

parameters (electron density, gas temperature etc) to tailor the process of carbon nanostructures growth.

Several material characterization techniques such as Fourier transform infrared (FTIR) spectroscopy, X-Ray photoelectron spectroscopy (XPS), Near-Edge X-Ray Absorption Fine structure (NEXAFS), Raman and X-Ray diffraction (XRD) spectroscopy, scanning and high-resolution transmission electron microscopy (SEM, HRTEM), selected area electron diffraction (SAED), energy-dispersive X-Ray spectroscopy (EDS) were used to study the morphological and microstructural features of the synthesized nanostructures.

I.3. Main Contributions

The work that led to this thesis has contributed in the following scientific output:

Peer-reviewed publications under the scope of this work:

- **A. Dias**, N. Bundaleski, E. Tatarova, F.M. Dias, M. Abrashev, U. Cvelbar, O. M. N. D. Teodoro and J. Henriques. "Production of N-graphene by microwave N₂-Ar plasma". J. Phys. D: Appl. Phys. 49 (2016) 055307 (9pp) [doi:10.1088/0022-3727/49/5/055307]
- E. Tatarova, **A. Dias**, J. Henriques, M. Abrashev, N. Bundaleska, E. Kovacevic, N. Bundaleski, U. Cvelbar, E. Valcheva, B. Arnaudov, A. M. Botelho do Rego, A. M. Ferraria, J. Berndt, E. Felizardo, O. M. N. D. Teodoro, Th. Strunskus, L. L. Alves & B. Gonçalves "Towards large-scale in free-standing graphene and N-graphene sheets". Scientific Reports 7 (2017) 10175 [doi: 10.1038/s41598-017-10810-3]
- N. Bundaleska, D. Tsyganov, **A. Dias**, E. Felizardo, J. Henriques, F. M. Dias, M. Abrashev, J. Kissovski, E. Tatarova. "Microwave plasma enabled synthesis of free-standing carbon nanostructures at atmospheric pressure conditions" Physical Chemistry Chemical Physics 20 (2018) pp. 13810-13824. [doi:10.1039/C8CP01896K]
- S. Hussain, E. Kovacevic, R. Amade, J. Berndt, C. Pattyn, **A. Dias**, C. Boulmer-Leborgne, M-R Ammar and E. Bertran-Serra. "Plasma synthesis of polyaniline enrobed carbon nanotubes for electrochemical applications". Electrochimica Acta 268 (2018) pp. 218-225. [10.1016/j.electacta.2018.02.112]
- C. Pattyn, E. Kovacevic, S. Hussain, **A. Dias**, T. Lecas, and J. Berndt. "Nanoparticle formation in a low pressure argon/aniline RF plasma". Applied Physics Letters 112 (2018) 013102. [doi:10.1063/1.5019926]
- D. Tsyganov, N. Bundaleska, E. Tatarova, **A. Dias**, J. Henriques, A. M. Botelho do Rego, A. M. Ferraria, M. Abrashev, F. M. Francisco, C. C. Luhrs, J. Phillips. Plasma Sources Sci. Technol. 25 (2016) 015013 (22pp) [doi:10.1088/0963-0252/25/1/015013]
- E. Tatarova, **A. Dias**, J. Henriques, A. M. Botelho do Rego, A. M. Ferraria, M. V. Abrashev, C. C. Luhrs, J. Phillips, F. M. Dias and C. M. Ferreira. "Microwave plasmas applied for the synthesis of free-standing graphene sheets". Journal of Physics D: Applied Physics 47 (2014) 385501 (11pp) [doi:10.1088/0022-3727/47/38/385501]

Chapters in books:

- E. Tatarova, **A. Dias**, E. Felizardo, N. Bundaleski, M. Abrashev, J. Henriques, Z. Rakočević and L.L. Alves. Book Title: “Atmospheric Pressure Plasmas: Processes, Technology and Applications Book Chapter” (Book ID: 8985). Book Chapter: “Microwave Plasmas Applied for Synthesis of Free-Standing Carbon Nanostructures at Atmospheric Pressure Conditions” (Chapter ID: 39815). Nova Science Publishers, 2016. [ISBN: 978-1-63485-214-2]
- **A. Dias**, E. Felizardo, D. Tsyganov, N. Bundaleska, M. Abrashev and E. Tatarova. “Assembling and engineering of 2D carbon nanostructures by microwave plasmas”. Book Chapter - Microwave Discharges: Fundamentals and Applications. Edited by A. Gamero and A. Sola. UCO Press, Editorial Universidad de Córdoba, 2015. [ISBN: 978-84-9927-187-3]

Communications in scientific meetings (Oral communications; Posters in conferences):

- **A. Dias**, J. Henriques, N. Bundaleska, E. Felizardo, F.M. Dias and E. Tatarova. “Fabrication of free-standing graphene and derivatives via a microwave plasma-based method”. Encontro Ciência 2018. July 2-4, 2018. Lisbon, Portugal. (invited talk)
- E. Kovacevic, C. Pattyn, I. Stefanovic, S. Hussain, C. Leborgne, **A. Dias**, E. Tatarova and J. Berndt. “Complex polymers, graphenes and composites”. 8th International Workshop on Polymer Metal Nanocomposites. September 12-15, 2017. Prague - Czech Republic. (invited talk)
<http://www.nanoworkshop.org/program.pdf>
- **A. Dias**, J. Berndt, E. Kovacevic, C. Pattyn, T. Strunskus, J. Henriques and E. Tatarova. “Free-standing graphene: synthesis and functionalization using plasma-based methods”. XXXIII ICPIG. Estoril, Lisbon - Portugal. July 9-14, 2017. (talk)
<http://icpig2017.tecnico.ulisboa.pt/wp-content/uploads/2017/05/ICPIG2017-booklet.pdf>
- N. Bundaleska, **A. Dias**, E. Felizardo, J. Henriques, F. M. Dias, N. Bundaleski, O. Teodoro, M. Abrashev, J. Kissovski, U. Cvelbar and E. Tatarova. “Plasma based N-

graphene synthesis – in-situ and post treatment approaches”. XXXIII ICPIG. Estoril, Lisbon - Portugal. July 9-14, 2017. ([poster](#))

<http://icpig2017.tecnico.ulisboa.pt/wp-content/uploads/2017/05/ICPIG2017-booklet.pdf>

- **A. Dias**, E. Felizardo, M. Abrashev, A. Almeida, J. Henriques and E. Tatarova. “Direct Synthesis of Nanodiamonds by Ar-H₂-CH₄ Microwave Discharges”. XXXIII ICPIG. Estoril, Lisbon - Portugal. July 9-14, 2017. ([poster](#))
<http://icpig2017.tecnico.ulisboa.pt/wp-content/uploads/2017/05/ICPIG2017-booklet.pdf>
- **A. Dias**, C. Pattyn, J. Berndt, E. Kovacevic, J. Henriques, E. Tatarova. “Graphene synthesis and applications using plasma-based methods”. 44th EPS Conference on Plasma Physics. Belfast – U.K. June 26-30, 2017. ([talk](#))
- C. Pattyn, E. Kovacevic, T. Lecas, S. Perrot, I. Stefanovic, **A. Dias**, T. Strunskus, J. Berndt. “Investigation of nanoparticle synthesis and thin film deposition in a aniline containing RF discharge” 44th EPS Conference on Plasma Physics. Belfast – U.K. June 26-30, 2017. ([talk](#))
- E. Kovacevic, S. Hussain, J. Berndt, C. Pattyn, T. Strunskus, M-R Ammar, A. Canizarès, P. Simon, E. Tatarova, **A. Dias**, P-Y Tessier and C. Boulmer-Leborgne. "Plasma Synthesis of Conductive Carbon-Based Nanomaterials" ECS Trans. 77 (3) 37-39, 2017. [doi: 10.1149/07703.0037ecst] ([invited lecture](#))
<http://ecst.ecsdl.org/content/77/3/37.full.pdf+html>
- E. Tatarova, **A. Dias**, J. Henriques et al “Microwave Plasmas Applied for Synthesis of Free-Standing Carbon Nanostructures” iPlasmaNano-VII 2016. 16-20 October 2016. Vravrona - Greece ([invited lecture](#)).
<http://www.athens2016.iplasmanano.org/index.php>
- J. Henriques, E. Tatarova, **A. Dias** et al. “Production of N-graphene by surface wave discharges, Julio Henriques” iPlasmaNano-VII 2016. 16-20 October 2016. Vravrona - Greece ([invited lecture](#)).
<http://www.athens2016.iplasmanano.org/index.php>

- J. Henriques, E. Tatarova, **A. Dias**, F.M. Dias, N. Bundaleski, M. Abrashev, E. Felizardo, U. Cvelbar. “Production of n-graphene by microwave N₂-Ar plasmas”. 7th IWSSPP. 26-June to 2-July, 2016. Kiten, Bulgaria. (lecture) http://iwsspp.deo.uni-sofia.bg/wp-content/uploads/2017/01/book_final.pdf
- E. Kovacevic, J. Berndt, C. Pattyn, Sh. Hussain, **A. Dias**, I. Stefanovic and Ch. Boulmer-Leborgne. “Plasma synthesis and functionalization of carbon based nanomaterials”. 7th IWSSPP. 26-June to 2-July, 2016. Kiten, Bulgaria. (lecture) http://iwsspp.deo.uni-sofia.bg/wp-content/uploads/2017/01/book_final.pdf
- **A. Dias**, E. Tatarova, J. Henriques, F. M. Dias, E. Felizardo, M. Abrashev, N. Bundaleski, Uros Cvelbar. “Synthesis of N-graphene using microwave plasma-based methods”. 69th Annual Gaseous Electronics Conference. October 10-14, 2016. Bochum, Germany (poster) <http://meetings.aps.org/Meeting/GEC16/Session/MW6.142>
- C. Pattyn, **A. Dias**, S. Hussain, T. Strunskus, I. Stefanovic, Ch. Leborgne, T. Lecas, E. Kovacevic and J. Berndt. "Nanoparticle formation and thin film deposition in aniline containing plasmas." 69th Annual Gaseous Electronics Conference. October 10-14, 2016. Bochum, Germany (poster) <http://meetings.aps.org/Meeting/GEC16/Session/MW6.109>
- **A. Dias**, E. Tatarova, J Henriques, S. Hussain, A. Petit, Ch. Leborgne, E. Kovacevic, J Berndt. “Graphene production and functionalization using plasma-based methods”. 27th Symposium on Plasma Physics and Technology. June 20-23, 2016. Prague, Czech Republic (**EPS Poster Prize**)
- **A. Dias**. “Plasma based assembly and engineering of 2D and 3D carbon nanostructures”. 1st annual meeting of the External Supervisory Committee of APPLAuSE (Advanced Program in Plasma Science and Engineering). Instituto Superior Técnico / ULisboa. November 2015. Lisbon, Portugal (lecture)
- **A. Dias**. "Plasmas for High Quality Graphene Production". “A Portugal Ventures e as StartUps Inovadoras dirigidas à Indústria” – Instituto Superior Técnico / ULisboa. November 2015. Lisbon, Portugal (invited pitch)

- **A. Dias**. "Plasmas for advanced carbon nanostructures synthesis". PhD Open Days – Instituto Superior Técnico/ULisboa. November 9-12, 2015. Lisbon, Portugal (**invited pitch – Best Pitch**)
- **A. Dias**, E. Tatarova, J. Henriques, F.M. Dias and M. Abrashev. “Microwave plasma-based method applied to carbon nanostructures production”. 9th International microwave discharges workshop. September 7-11 2015. Córdoba, Spain. https://www.uco.es/md-9/Booklet_Web-1.pdf (poster)
- E. Tatarova, J. Henriques, F.M. Dias, D. Tsyganov, **A. Dias**, A. M. Rego, A. Ferraria, M. Abrashev, E. Kovacevic, J. Berndt and Th. Strunskus. “Assembling and engineering of 2D carbon nanostructures by microwave plasmas”. 9th International microwave discharges workshop. September 7-11 2015. Córdoba, Spain. https://www.uco.es/md-9/Booklet_Web-1.pdf (lecture)
- F. M. Dias, E. Tatarova, J. Henriques, **A. Dias**, M. Abrashev, U. Cvelbar, G. Filipič, Zh. Dimitrov and Zh. Kissovski. “N-doping of graphene by N₂-Ar remote plasma”. 9th International microwave discharges workshop. September 7-11 2015. Córdoba, Spain. https://www.uco.es/md-9/Booklet_Web-1.pdf (lecture)
- J. Henriques, E. Tatarova, F. M. Dias, **A. Dias**, N. Todorov, N. Bundaleski and O. Teodoro. “Nitrogen Doped Graphene Sheets Synthesized by Surface Wave Plasmas”. 32nd ICPIG. July 26-31 2015. Iași, Romania http://www.icpig2015.net/Content/Posters/id158_Julio_HENRIQUES.pdf (poster)
- E. Tatarova, J. Henriques, F.M. Dias, D. Tsyganov, **A. Dias**, A.M. Rego, A. Ferraria, M. Abrashev, E. Kovacevic, J. Berndt and Th. Strunskus. “Microwave Plasmas Applied for Synthesis of 2D Carbon Nanostructures”. 42nd EPS Conference on Plasma Physics. Lisbon, Portugal. June 22-26 2015. <http://ocs.ciemat.es/EPS2015ABS/pdf/I4.009.pdf> (general lecture)
- **A. Dias**, E. Tatarova, J. Henriques, F.M. Dias, M. Abrashev, Uroš Cvelbar, Gregor Filipič, Zh. Dimitrov and Zh. Kissovski. “N-graphene synthesis using N₂-Ar remote plasmas”. 42nd EPS Conference on Plasma Physics. Lisbon, Portugal. June 22-26 2015. <http://ocs.ciemat.es/EPS2015ABS/pdf/O4.301.pdf>

I.4. Dissertation Outline

This thesis is organized in function of the plasma setups under investigation combined with the different structures produced.








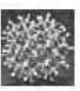

The first chapter will cover the theory concerning the concepts and the methods used to both produce and characterize the experimental data, with the description of the experimental setup being in detail on the subsequent chapter.

The second chapter will be dedicated to experiments, results and discussion. This chapter is divided in three subchapters, and within the first two subchapters we will have five sections. The first two sections will be dedicated to experimental setup and basic workings of the apparatus, respectively. Furthermore, the two subsequent sections will present the plasma and material characterization results and respective discussion. The third subchapter will be focused on the graphene applications, which is divided in three sections. One is dedicated to the preparation of the graphene samples and the other two are related with the preliminary studies concerning the usage of graphene for a particular application. Each of the three subchapters contain respective summary of the analysed data.

The third and final chapter resumes the important results of the previous chapter.

I.5. State of the Art

Carbon-based nanomaterials are potential candidates for various applications in medicine such as drug delivery, biosensing and bioimaging but also in nanoelectronics, for semiconductors, transistors, display panels, etc. A simple way to summarize the diversity of carbon nanostructures present in the market nowadays Table I-1 is presented.

Schematic view	Entity	Comments, characteristic sizes (experiment)
	Fullerene	Smallest:* C ₂₀ [72] Most abundant: C ₆₀ Largest: C ₃₂₀ [73]
	Carbon onions	Outer diameter (max): 70 shells [51] Inner diameter: 0.7–1 nm (–C ₆₀) [50] From detonation nanodiamond: 5–8 shells [74]
	Single wall nanotubes (SWNTs)	Diameter: typically 1–10 nm [56] Range of diameters: 0.4–100 nm Length: typically 50 nm to 1 μm
	Multiwall nanotubes (MWNTs)	Length: 10 nm to 1 μm Outer diameter: typically 2.5–30 nm [56]
	SWNT ropes SWNT single crystals [62]	Typically 10–100 tubes in a rope (synthesized by laser ablation) Typical length: tens of microns In strands: thousands of NTs
	Single Graphene sheet	Size: 10–15 nm [75] at distance from the substrate: 0.35–0.37 nm
	Diamondoids	Largest molecule currently extracted from crude oil: undecamantane (11 cages) [70]
	UNCD particles	Average size after purification of detonation diamond: 4–5 nm Min size: 1.8 nm [5]
	UNCD films	Average grain size: 2–5 nm [1]; sharp grain boundaries (mostly twist GBs)

* The smallest possible fullerene had been produced from dodecahedrane C₂₀H₂₀ by replacing the hydrogen atoms with bromine atoms followed by gas-phase debromination.

Table I-1 - Range of geometrical characteristics of selected carbon entities and their simplest assemblies observed at the nanoscale. Table taken with original references from [28].

Besides the materials mentioned in the previous table numerous others exist namely triply periodic minimal surfaces (TPMS)[29] exhibited in schwarzites, carbon nanofoams[30] and the theorized hollow diamond[31].

I.5.1. Graphene

Graphene is a two-dimensional hexagonal single sheet of carbon atoms as it can be seen in Figure I.1. arranged in a honeycomb lattice. The unit cell spanned by the following two vectors:

$$\vec{a}_1 = \frac{a}{2}(3, -\sqrt{3}), \quad \vec{a}_2 = \frac{a}{2}(3, \sqrt{3}) \quad (1)$$

contain two atoms, one of type A and the other of type B, which represents the two triangular lattices. The corresponding reciprocal lattice vectors are:

$$\vec{g}_1 = \frac{2\pi}{3\sqrt{3}a}(\sqrt{3}, -3), \quad \vec{g}_2 = \frac{2\pi}{3\sqrt{3}a}(\sqrt{3}, 3) \quad (2)$$

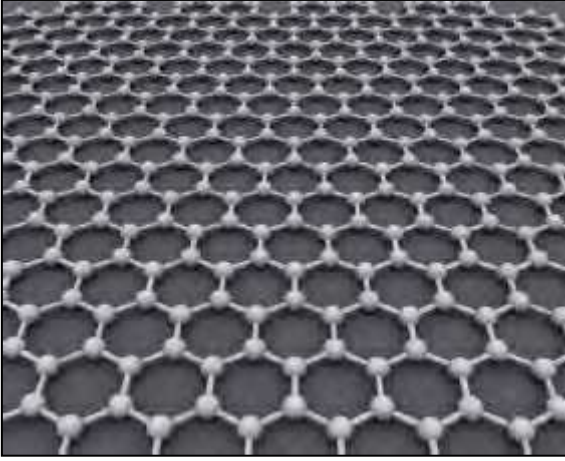


Figure I.1 - Graphene structure [2] and graphene lattice structure and first BZ.

In Figure I.1 the first BZ has a hexagonal structure with a side length of $4\pi/3\sqrt{3}a$ and the two points $K = \frac{2\pi}{3a}(1, \frac{1}{\sqrt{3}})$ and $K' = \frac{2\pi}{3a}(1, -\frac{1}{\sqrt{3}})$.

Carbon atom electronic configuration is ${}^6C = 1s^2 2s^2 2p^2$. Each carbon atom has four valence electrons in ground state, two in the 2s subshell and two in the 2p subshell. These 2s, 2p_x, 2p_y and 2p_z orbitals can mix each other to form different hybrid orbitals, leading to different forms of carbon structures. For example:

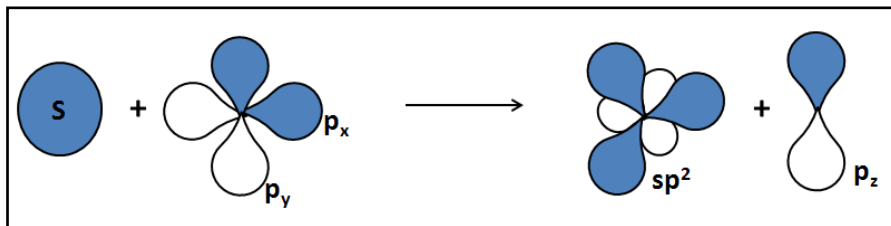


Figure I.2 - Graphene orbitals configuration

The bonds between carbon atoms are done via sp hybrid (sp , sp^2 and sp^3). Therefore the graphene is formed by the bonds between the nearby carbon atoms with sp^2 hybrid orbitals, i.e. $2p$ orbitals hybridize with one s orbital to form three sp^2 orbitals, leaving an unoccupied $2p_z$ orbital perpendicular to the plane of the two-dimensional sheet of graphene. The planar orbitals form is stable and contains σ -bonds with the three nearest carbon atoms in the honeycomb lattice. These bonds are responsible for most of the binding energy and for the elastic properties of the graphene sheets. The σ -bonds are energetically very stable and localized and due to that they do not contribute to electrical conduction. The remaining free $2p_z$ orbitals overlap neighbouring carbon atoms play a major role in the electronic properties of graphene.

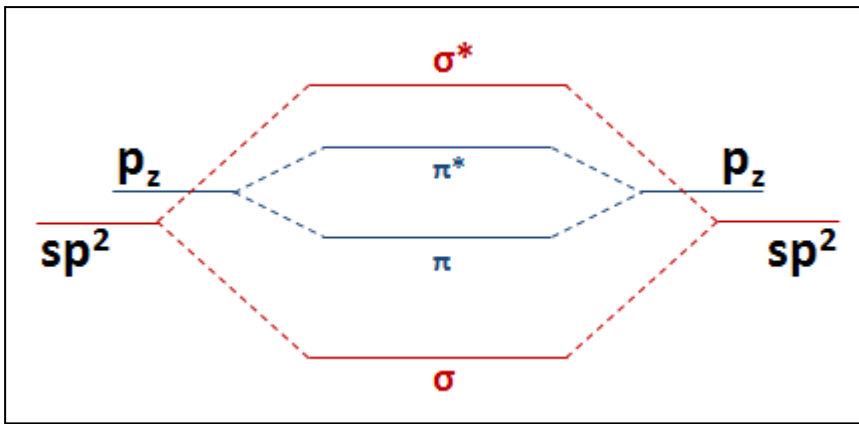


Figure 1.3 - σ and π -bonds configuration in a metal

The exceptional electronic properties are due to the formation of π -bonds by the overlapped p_z orbitals. Graphene is composed of two bands, in which the first one is the valence band formed by π bonding states and the other one is formed by π^* anti-bonding states. The band structure of graphene has been calculated using the tight-binding approximation by considering the p_z orbitals only for each of the two atoms in every primitive shell. The calculation involves the construction of the wave function which is a linear function for superposition of wave functions for A and B atoms and the use of variational principle to obtain eigen functions and eigen states. The energy dispersion of π and π^* band is given by:

$$E(k) = \pm \gamma_0 \sqrt{1 + 4 \cos\left(\frac{3}{2} k_x a\right) \cos\left(\frac{\sqrt{3}}{2} k_y a\right) + 4 \cos^2\left(\frac{\sqrt{3}}{2} k_y a\right)} \quad (3)$$

Where k_x and k_y are the components of \vec{k} in the (k_x, k_y) plane, $\gamma_0 = 2.75$ eV is the nearest-neighbor hopping energy and the \pm stands for upper (π^*) and lower (π) band, respectively. The

3D electronic dispersion and energy contour lines in k-space (two cones) can be seen in Figure I.4. Near the k and k' points, the energy dispersion has a circular cone shape which is given by:

$$E(k) = \pm \hbar v_F |k| \quad (4)$$

Here $v_F = \left(\frac{3\gamma_0 a}{2\hbar} \right) \approx 10^6 \text{ m.s}^{-1}$ is the Fermi velocity ($v_F = c/300$).

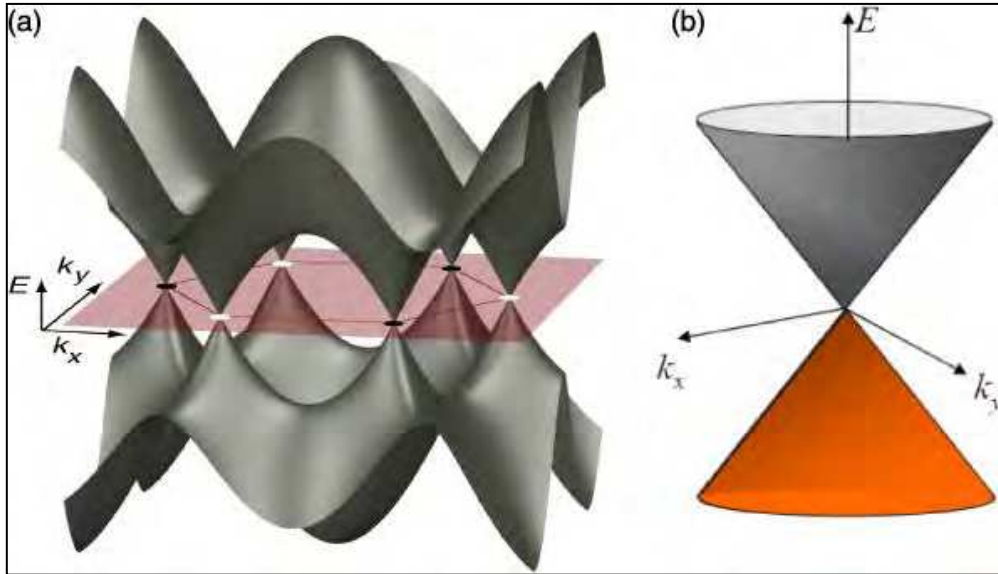


Figure I.4 - Graphene band structure. a) Three-dimensional band structure. Adapted from Beenakker [32]. b) Zoom into low energy dispersion at one of the K points shows the electron-hole symmetric Dirac cone structure.

To better understand the differences between graphene and conventional 2D electron system basic features of electronic band structure can be compared (see Figure I.5). In the 2D conventional electronic system the electron is confined in the z direction by electrostatic potential, leading to quantization of k_z and thus discrete energy steps. Each energy step is a sub-band with a parabolic energy dispersion curve. Due to the energy quantization the density of states is given by a sum of steps function. In contrast, graphene is a perfect 2D system; therefore, there are no sub-bands energies from the confinement in the z direction. The single band has a linear dispersion in the (k_x, k_y) plane, instead of parabolic. The π bond, valence band, and π^* anti-bond, conduction band, are separate, but the band gap is so minimal that it is considered to be zero. The Fermi level is located in the band gap leading to the cones (see Figure I.4 and

Figure I.5). The bottom cone represents the electrons and the top inverse cone represents the “holes”, meaning the area not occupied by an electron.

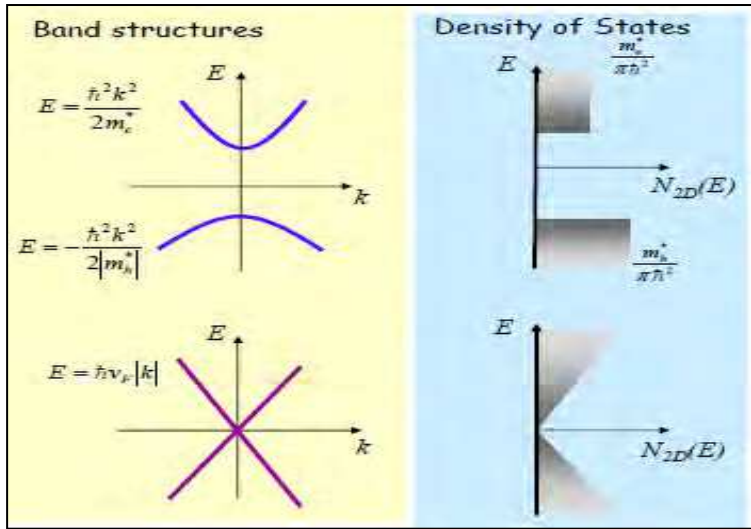


Figure I.5 - Band structures and density of states (DOS) for graphene.

The energy bands depend only on in-plane momentum because the electrons are restricted to motion in a two-dimensional plane. Graphene’s unique electron structure is characterized by conical valence and conduction bands that meet at a single point in momentum space (the Dirac crossing energy). Valence and conduction band have equal energies at six points, which are located on the corners of the Brillouin zone (see Figure I.4). These points are called k valleys or Dirac points. At these points, the electrons always move at a constant speed, i.e. $v_F \approx 10^6 \text{ m.s}^{-1}$. The interaction between graphene’s 2D honeycomb lattice and its electrons causes the electrons to move as massless electrons, described by Dirac-type equation, which is the quantum mechanical description of electrons moving in terms of Einstein’s theory of relativity. For this reason, graphene’s electrons are called Dirac fermions (spin $\frac{1}{2}$). They can travel large distances without being scattered, up to $25000 \text{ cm}^2(\text{v.s})^{-1}$ and can be controlled using electromagnetic field (behaving more as waves than as particles) and carry one unit of electric charge. Some of the characteristics founded in graphene are the unconventional integer quantum Hall effect [33], [34], Klein tunnelling [35], [36], valley polarization [37], universal minimum conductivity [7], [38], weak localization (WAL)[7], [39], ultrahigh mobility [7], [40], specular Andreev reflection at the graphene-superconductor interface [41], [42], etc.

In respect of the quantum Hall effect of graphene there has been done some research work by Novoselov et al.[33] in which it was firstly observed the Hall Effect. The Hall conductivity is given by[33], [34]:

$$\sigma_{xy} = \pm 4(l + 1/2) \frac{e^2}{h} \quad (5)$$

Where $|l|=0, 1, 2, 3, \dots$, is the Landau index. At higher energies the plateaus appear at half integers of $4e^2/h$. In presence of magnetic field, the spectrum of massless Dirac electrons has a Landau level with energy precisely at the Dirac point, that is half-filled in neutral graphene[43], which leads to the $1/2$ in the Hall effect referred previously[44] in eq. (5). Due to the transition across the Fermi “edge” spans a small range of energies, the waveform is square rather than sinusoidal.

Concerning the electrostatic confinement[45] and tunnelling property[45] of graphene does not have the same behaviour that the usual 2D electron system has, more specifically in respect of the lateral confinement. The confinement in one direction can lead to a quantum wire, and its energy levels are given by the following equation:

$$E_{n_y n_z} = \frac{(\hbar k_x)^2}{2m^*} + \frac{\hbar^2}{2m^*} \left(\frac{n_y \pi}{L_y} \right) + \frac{\hbar^2}{2m^*} \left(\frac{n_z \pi}{L_z} \right) \quad (6) [45]$$

Where n_y, n_z are integers, m^* is the effective mass, k_x is the wave vector in the x direction and L_y, L_z are the dimensions of the quantum wire in the y and z direction, respectively. The nano wire weakness is the graphene nanoribbon, because not only its width but also its electronic spectrum depends on the edge’s nature. Using methods like tight-binding method[46], [47], Dirac equation[48], [49] or first-principles calculations[50], [51] to calculate the energy dispersion of the nanoribbons it’s possible to conclude that nanoribbons with armchair edges can be metallic or semiconducting material depending on their width, and nanoribbons with zigzag edges are always metallic with peculiar edge or surface states. Chiral electrons are not able to be confined effectively by electrostatic potential barriers even though they can be confined effectively in nanoribbons through the boundaries.

In respect of weak(-anti) localization (WAL)[45] it consists on weakly disorder systems where scattering events occur, like elastic and inelastic processes, which affect electron transport. In the elastic processes electron energy does not change, and as a result its phase evolution can be traced, on the other hand, in the inelastic processes the electrons forget their phases but it's possible to know the probability of losing phase memory ($Probability = \frac{1}{\tau_\phi}$), where τ_ϕ is the phase relaxation time. When τ_ϕ is much bigger than momentum of relaxation time (τ), i.e. $\tau_\phi \gg \tau$, quantum interference correction (QIC) to electrical resistance manifests in WL. The momentum of relaxation time is inherent to the quantum interference between self-retained and multiply scattered paths of electrons on the scale of coherent length ($L_\phi = v_F \cdot \tau_\phi$)[52], [53]. When the magnetic field applied is bigger than $\frac{\hbar}{2L_\phi^2}$, the WL is broken because of the electrons that travel in different directions. Usually WL is associated to negative magnetoresistance effect. In graphene and general 2D system WL is affected by inelastic and some elastic scattering and also by spin-flip (related with strong spin-orbit coupling)[39], [54], [55]. Graphene has wave function envelop of electrons around k point, therefore the overlapping between functions can happen and that leads to suppression of long-range scatters (intravalley backscattering), subsequently WAL appears[54], [56]. WL and WAL can be observed in graphene depending on the ratio $\tau_\phi/\tau_{intervalley}$ when inter valley scattering (when graphene has sharp defects or edges in narrow ribbons) is dominant. If $\tau_\phi \gg \tau_{intervalley}$, WL is observed, but on the other side, if $\tau_\phi \ll \tau_{intervalley}$, WAL occurs[54]. At high temperature and low carrier density WAL prevails WL[57], which is in conformity with theoretical predictions[39]. All the defects present in graphene, like long range distortions, non-planarity of the layers and slow variation of electrostatic potential lead to large differences in QIC of measured conductivity[55]. It is possible to conclude with recent results from Yan and Ting[58] research work that QIC of conductivity depends on the sample size, carrier concentration and temperature. Morozov et al.[59] and Novoselov et al.[33] ruled out the possibility of the WL suppression its due to the short phase-breaking length and magnetic impurities, instead they think that mesoscopic corrugations in graphene sheets can induce a nominal random magnetic field which could lead to WL suppression. There are some results that indicate the possibility to occur a total suppression of WL in samples where inter valley scattering is negligible.

Minimum conductivity of e^2/h is reached even at the lowest temperature possible when density of states at Dirac points in graphene is zero[33], [34]. Some studies reveal that minimum conductivity depends on geometry of the structures and it is relatively constant, approximately 3.3 to $4.7 \times \frac{4e^2}{\pi h}$. Measurements were made in relatively large devices with a length of more than $1\mu\text{m}$ and areas above $3\mu\text{m}^2$. But for small devices, with lengths and areas below 500 nm and $0.2\mu\text{m}^2$, respectively, the minimum conductivity varies with the ratio $\text{width}/\text{length} \equiv W/L$, decreasing from $4 \times \frac{4e^2}{\pi h}$ at $\frac{W}{L} = 1$ to $\frac{4e^2}{\pi h}$ at $\frac{W}{L} = 4$, saturating at this value [55], [60]. For large samples the theoretical predictions confirm that the minimal conductivity not only depends on the geometry of graphene but also on the microscopic details of the edges[61]. In perfect graphene samples the electrical conductivity is done by evanescent waves[61], but for non-perfect graphene samples the minimal conductivity is affected by scattering with centres coming from impurities, defects and phonons[62]. Chen et al.[63] have done some research and reached a conclusion that for an increasing of doping concentrations in the samples, which could come from charge impurities from the substrate or from the vicinity of graphene, the minimum conductivity and mobility decrease. It was demonstrated by Ostrosky et al.[64] that away from Dirac point for strong scatters exists a linear relationship between conductivity and carrier concentration (n), nevertheless for weak scatters exists a logarithmic relationship between the same physical quantities. To reduce scattering from charged impurities there are two possibilities, which are removing substrate from the graphene samples or using high-k dielectrics[42], [65]–[68]. Some research done showed for suspended graphene sheets high values of mobility, approximately $2 \times 10^5\text{ cm}^2\text{V}^{-1}\text{s}^{-1}$, for n below $5 \times 10^9\text{ cm}^{-2}$, minimum conductivity at low temperatures of approx. $1.7 \times \frac{4e^2}{\pi h}$ [42]. The effect of impurities absorbed on the graphene sheets surface was studied by Bolotin et al.[66] and in respect of electrical transport dirty samples have low mobility (approx. $28000\text{ cm}^2\text{V}^{-1}\text{s}^{-1}$) which increases up to $170000\text{ cm}^2\text{V}^{-1}\text{s}^{-1}$ when the sample is cleaned with UHV. For ultraclean graphene sheets resistivity depends on the temperature in a range $5\text{--}240\text{K}$, and the relationship between these two physical quantities becomes linear when the temperature is above 50K and the carrier concentration is above $5 \times 10^{11}\text{ cm}^{-2}$. As a result, scattering from acoustic phonons dominates electrical transport[45].

I.5.1.1. Methods of synthesis

One of the greatest challenges on the path towards graphene commercialization is the production of high quality material on a large scale at low cost and in a reproducible manner[69]. A large number of methods have been developed to synthesize graphene, including mechanical exfoliation of natural or synthetic graphite[7], [45], thermal decomposition of SiC[70], wet chemistry reduction techniques that employ graphite oxide (GO)[45], [71], liquid-phase exfoliation[72] and chemical vapor deposition (CVD)[73], [74]. Generally, these methods allow the synthesis of large-area graphene films and micron/submicron sized graphene sheets.

Mechanical exfoliation was developed by Geim group[7], the precursor used is highly oriented pyrolytic graphite (HOPG). The technique begins with a plasma etching to produce deep mesas, to press it afterwards into a photoresist layer. After the photoresist have been baked and HOPG been cleaved from the resist, part of the samples is removed with tape, obtaining consequently pieces of graphite. Therefore, the removed material is dissolved in acetone and captured on the surface of Si/SiO₂ wafer. In this experiment one of the important results was the fabrication of few and single-layer graphene which reached 10 μ m of length. The clear disadvantages of this method rely on the fact on non-scalability and selectivity of graphene synthesis process.

Thermal deposition of SiC[70] is a technique based on heating SiC in ultrahigh vacuum reaching temperatures between 1000 °C and 1500 °C in a way to Si sublimate from the material and leave behind a carbon rich surface, which is graphitic in nature, being possible to be used in graphene production.

This technique is good to produce wafer-scale graphene layers, meanwhile there are some difficulties to be overcome such as controlling the number of layers produced, repeatability of large areas growths and interface effects with the SiC substrate.

Molecular beam deposition was used by Zhan et al.[75] to produce layer-by-layer graphene. As the name says with this method it's possible to produce graphene with multiple layers and the number of layers does not depend of the cooling rates, so consequently the carbon is not absorbed into the bulk of nickel[75]/cobalt[76]. This technique starts with a gas with carbon in its composition (eg. ethylene), molecules are then broken at 1200°C using a thermal cracker and afterwards the fabricated material relay on a nickel substrate. CVD[73], [74] allows the production of large area sheets (currently of interest for low power graphene-based electronics

and optical devices[77]), but its efficiency depends on the quality of the underlying polycrystalline metallic film (catalyst) and it requires multiple processing steps to obtain transferable sheets[45], [73], [74], [78], a big disadvantage also shared by molecular beam deposition method. It is worth noting that the presence of metal impurities can affect the real performance of the synthesized material.

I.5.1.2. Plasma-based methods

The unique chemically active plasma environment provides suitable conditions to dissociate molecules in order to synthesize unique structures in ways that are not otherwise possible. Many applications exploit the ability of plasmas to break down complex molecules considering that plasma systems provide simultaneously high temperatures and highly reactive environment. The plasma systems comprise thermal and chemical reactor functions, as well as catalytic properties. Therefore, plasma assisted growth of nanostructures can be achieved without using catalysts at lower substrate temperatures due to the plasma's unique ability to activate the surface, thus creating favourable conditions for nucleation and growth processes[11].

Unique aligned growth of vertical graphene on Ni foam and silicon support has been achieved[12], [79]. Many of the current plasma techniques aimed at synthesizing carbon nanostructures involve plasma enhanced CVD (PECVD). PECVD can be done with different kinds of plasma, including radio frequency (RF)[80], [81], microwave and DC[82] which have been used to produce mainly carbon nanosheets and carbon nanowalls, respectively. Quartz substrates are used in DC PECVD method while in microwave PECVD[83], [84] the nanostructures are usually grown on metallic substrates.

However, PECVD methods typically require low-pressure environments (<10 Torr) with the synthesis and growth of the structures occurring as in a conventional CVD proceed via reactions on the surface which depend on the substrate properties, often with low growth rates[85]. These methods struggle in producing high quality continuous and uniform graphene films on large areas. Many applications, including supercapacitors, batteries, nanocomposites, etc, require graphene nanosheets in the form of free-standing graphene sheets consisting of a few atomic monolayers[8], [86], [87]. Such self-standing graphene sheets are an alternative to surface-supported horizontal graphene because both surfaces can be utilized, while surface bound counterparts can effectively

only use one, and allow the use of at least three open edges in applications. To the best of our knowledge, only a couple of examples in the literature focus on the production of isolated free-standing graphene sheets using plasmas at atmospheric pressure conditions. In the work of Dato[88], [89] free-standing graphene sheets synthesis using microwave plasma is reported without justification for the process that is simply referred as gas-phase synthesis. Moreover, the synthesized carbon material contains a large amount of amorphous carbon along with some individual graphene sheets as described in a related patent[89].

Another method for freestanding carbon materials synthesis was firstly developed by MacKinnon et al.[90], [91], Aerosol-Through-Plasma (ATP) method. Although this method allows the production of reduced-state nanoparticles and creation of different kinds of nanostructures, the respective disadvantages of this method rely on the lack of selectivity synthesis, i.e just one carbon allotrope. It is also important to mention that it could be a disadvantage the presence of oxygen during the process because it could oxidize the sample but, in some cases, the oxidize nanostructure can be used to other important applications.

Further on, Timothy Lambert and Claudia Luhrs et al.[92] improved ATP method to synthesize graphene-like materials. Basically, the technique consisted on obtaining graphene by firstly thermally exfoliate and reduce graphene oxide by passing it through low power microwave aerosol plasma, using in this case argon as the carrier gas. This method shows the potential of microwave plasmas for carbon-based materials, nevertheless the lack of control on the type of the synthesized material still remains. Selective synthesis of only high-quality free-standing graphene sheets has been reported in [3], [4], [23], [93], but this was at the expense of quantity, i.e. at very low yield of about 0.01 mg/min.

Part of the work developed in this thesis intend to provide substantial evidence that microwave plasma technologies, and in particular the ones based on wave-driven plasmas, can be used as a competitive and disruptive alternative to chemical methods in the controllable fabrication of free-standing graphene sheets. The novelty of the plasma approach used is based on the process scale-up using large-scale configuration of microwave driven discharges and complementary engineering to control morphologies and structural qualities of targeted nanostructures.

I.5.2. Doped and functionalized graphene

Graphene can be considered as an atomic-scale scaffold, on the basis of which new 2D crystals can be created. It is noteworthy that nitrogen functional groups covalently attached to the graphene scaffold and the specific properties of graphene lead to an extraordinary electrochemical performance[8], [11], [94]. A promising way to tune and control the electronic properties of graphene is by doping it with heteroatoms. Hence, nitrogen doping allows graphene transformation into n- or p-type semiconductor respectively, accompanied by the opening of a bandgap[95]. By simple replacement of some of the carbon atoms with nitrogen atoms in the lattice structure, N-graphene capacitors are capable of holding 99.8% of the nominal capacitance even after 100,000 cycles[8], [96]. Preserving graphene's large electric double-layer capacitance, N-graphene offers improved wettability and pseudocapacitance[78]. N-graphene is also a very promising material for the development of metal-free, carbon-based catalysts with even a better performance than commercially available Pt-based electrodes for oxygen reduction reaction in fuel cells[11], [94], since N atoms create "activate sites" on the graphene scaffold that can participate in catalytic reaction directly. Recently, lithium-sulfur batteries with a very high theoretical energy density (2600 Wh kg^{-1}) appeared as one of the most promising candidates for next-generation energy storage devices[97], [98]. However, several difficulties impeding the practical use of lithium-sulfur batteries, including the 'shuttle effect' and the irreversible loss of active materials, need to be addressed. To this end, incorporating graphene into the flexible sulfur containing electrodes as a scaffold material would greatly improve electrode performance. Nitrogen-doped graphene exhibits strong-couple interactions for anchoring sulfur-containing species, thus achieving higher stability and reversibility when compared with pristine graphene[86], [99].

Graphene doping with nitrogen tailors not only the electronic properties but also the chemical and structural ones. Generally, several bond configurations such as Pyridinic-N, Pyrrolic-N and Graphitic-N are expected to be found within the carbon lattice while doping graphene with nitrogen atoms[100].

Pyridinic-N (N-6) and Pyrrolic-N (N-5) consist on nitrogen atoms bonded with two carbon atoms at the edges or defects of graphene, where N-6 donates one p-electron to the aromatic π system, and N-5 contribute with two p-electrons to the π system[95], [101] (see Figure I.6). In Quaternary-

N (N-Q) nitrogen atoms substitute for carbon atoms in the hexagonal lattice of graphene. Among these nitrogen bond configurations, pyridinic-N and quaternary-N are sp^2 hybridized and pyrrolic-N is sp^3 hybridized. Some N-oxides are also very common also to be found in nitrogen doping[19], [100], [102]–[104].

Figure I.6 – (a) Schematic representation of N-doped graphene. Gray for the carbon atom, blue for the nitrogen atom, and white for the hydrogen atom. A possible defect structure is shown in the middle of the ball-stick model[19]. (b) Schematic of nitrogen bonding configuration. Pyridinic-N (N-6), Pyrrolic-N (N-5), Quaternary-N (N-Q).

I.5.2.1. Methods of synthesis

Numerous methods have been developed to synthesize graphene, including, mechanical and chemical exfoliation, chemical vapor deposition, reduction of graphene oxide among many others[11]. However, only a few methods have been developed to produce N-graphene.

Nitrogen doping of graphene applying high power electrical annealing, thermal annealing[15], [16], and CVD of methane in the presence of ammonia[17] were reported. Plasma assisted doping of graphene has also been demonstrated. It should be noted that plasma-based methods for engineering graphene properties can be considered superior to the chemical ones, since the former ensure high level of controllability, good quality and reduced environmental risks[6], [11], [105]. On top of this, plasma methods have many idiosyncratic features which place them uniquely and very competitively in the nanoscale science and technologies domain[8], [106]. These methods are superior to other approaches due to the possibility of modifying only a nano-thick region without affecting bulk properties of the material. Under reactive plasma surface interaction, a wide variety of functional groups and foreign atoms can be attached covalently to form different atomic planes,

depending on the chemical nature of the gas and plasma parameters. Hence, dramatic changes in the correlation of electronic and atomic constituents in nanostructures and unique properties of matter can occur due to plasma assisted doping and functionalization. By tuning the plasma environment, i.e. the amount of nitrogen radicals, thermal velocity of heavy species, electron density and temperature, the doping can be controlled and optimized. Plasma treatment is also compatible with standard microfabrication procedures and can, therefore, be easily incorporated into device fabrication protocols. Successful doping of graphene with nitrogen by means of NH_3 plasma exposure, for instance, was already reported[14]. N-graphene has also been produced using a DC arc discharge between pure graphite electrodes using NH_3 or pyridine vapour as the nitrogen precursor[9]. Although achieving a high yield, the method lacks doping controllability (reaching only 1 % in a pure NH_3 plasma), relies on the use of graphite electrodes and produces N-graphene containing metal impurities. N-graphene was also obtained by exposing graphene to RF nitrogen plasma environment[15]. The obtained material exhibited much higher electrocatalytic activity toward oxygen reduction than pure graphene and had much higher durability and selectivity than standard Pt catalyst used for oxygen reduction. However, the mechanisms responsible for the unique properties exhibited by plasma-created N-graphene nanostructures are still to be understood. Most of the works reported rely on "trial-and-error" empirical approaches where plasma is treated as a "black box". Essential information about main plasma characteristics is missing. Despite the great progress made so far, it remains a challenge to precisely control the doping process and to provide sustainability at high processing temperature. In this respect, the strategy to synthesize N-doped graphene through plasma treatment presents significant advantages. The work shown in this thesis demonstrates successful nitrogen doping of free-standing graphene sheets applying microwave plasma treatment[107].

In the present thesis a microwave N_2 -Ar plasma-based method for production of N-graphene is presented. Free-standing graphene sheets synthesized by a microwave plasma in a single step and at atmospheric pressure conditions, as described in[107], are subjected to the remote region of a low pressure N_2 -Ar plasma for different exposure times and different concentrations of nitrogen in the plasma gas mixture. Direct N-graphene synthesis is presented as well and serious advances have been achieved. The method is rapid, highly cost-efficient and environmentally friendly, since it does not require the use of catalysts and harmful chemicals. It is also versatile and

customizable, enabling the synthesis of different 2D nanostructures, i.e. graphene and N-graphene, in the same reactor. Furthermore, the high energy density of the generated plasma environment allows the use of gaseous or liquid precursors.

I.5.3. Nanodiamonds

Diamond particles are interesting in both academic and industrial worlds due to their extreme and in many cases superlative properties. Though regular diamonds are fascinating by their brilliance and prettiness, they exhibit excellent properties such as the highest hardness, thermal conductivity and the widest optical transparency window. Likewise, nanodiamonds (NDs) possess a distinct combination of outstanding unique mechanical, chemical, biological, magneto-optical and electronic properties, which can be improved when enriched with functional groups. Diamond is a 3D structure composed by sp^3 bonded carbon atoms arranged in a tetrahedral symmetry. Although it has been reported a variety of diamond-like structures in the literature only some of them have been observed, such as bucky-diamonds that consists on core-shell hybrid nanocarbon particles[108], characterized by an sp^3 -bonded diamond core and a partial or complete sp^2 -bonded fullerenic outer shell[109], as well as the hexagonal 2H (lonsdaleite)[110], 6H[111], 8H[112], and rhombohedral 9R[110] and 15R[113]. Some of these structures have been considered as nanoparticles[110], [114], [115] that are mostly imbedded in a matrix. Nanoparticles of n-diamond, i-carbon, and x-diamond have also been observed, being n-diamond a metallic (fcc) form of carbon with a lattice constant of 3.59 Å and 8-13 nm of diameter[116], i-carbon a cubic structure with a lattice constant of 4.32 Å and 15-40 nm of diameter[116] and x-diamond a fcc structure with a lattice constant of 3.57 Å[117]. Free-standing NDs consist on nanometer-sized diamond crystals that possess the favourable properties and structure of diamond, nonetheless, provide additional advantages due to their confined size. NDs average size range from 1 up to hundreds of nm, but they can be divided in four large groups, i.e. zero, one, two and three-dimensional diamonds, according to the dimensionality of the diamond constituents. Zero-dimensional diamonds are structures in the form of isolated particles and particles embedded within a matrix of other material which includes nanocrystalline diamonds (NCDs), i.e. nanodiamonds with less than 100 nm of diameter, ultrananocrystalline diamonds (UNCDs), where primary particle size is smaller than 10 nm[28] and diamondoid molecules that are well-defined hydrogen terminated molecular

forms consisting of several tens of carbon atoms[28]. On the other hand, one-dimensional diamonds comprise polycrystalline and single crystal diamond rods/cylinders/whiskers with diameters spanning the range of several tens of nm [118]–[124]. The 2-D diamonds consist basically on single diamond nanoplatelets that grow usually on polycrystalline diamond structures[125]. And finally, we have the 3-D diamonds that include UNCD films, carbide-derived diamond-structure carbon and bulk-sintered UNCD particles of detonation origin [28]. UNCD films with 2–5nm grains have been discovered in the 90’s[126], [127]. Selective etching of carbides has been used for the synthesis of nanocrystalline diamond[128], being commonly used in coating. ND composite [129], [130], which consists of UNCD particles connected by a pyro-carbon matrix and is characterized by a high porosity, between 50 and 70 %, and demonstrates a quite high Young’s modulus of 30 GPa and a maximum pore size of 20–30 nm. Due to the high density of nanopores, the material possesses a high absorption activity, mostly for large biomolecules[131]. The UNCDs are of great interest for biomedical applications, besides the biocompatibility that is inherent to these structures also their dimensions are very promising. The high stability, biocompatibility, genotoxicity, selectivity in binding biological materials and outstanding electrochemical properties of NDs make them suitable for biosensors[132], [133]. Nevertheless, they are also being used as substrates in coating for biomedical implants, replacing silicon, platinum and quartz due to their low cytotoxicity, dense structure, high surface roughness, sp^2 structural boundaries and surface dangling bonds[134]–[136]. UNCDs films can be used for microelectromechanical devices considering their robustness, high Young’s modulus, high acoustic velocity, high resistance to fracture, and low friction coefficient (between 0.01 and 0.1 approximately)[137], [138]. Other promising applications of NDs includes also drug delivery and gene therapy making it a very powerful weapon in cancer treatment, tissue scaffolds and surgical implants and in bioimaging using modified nanodiamond with nitrogen vacancy centres, however, purified, “free” state, and single digit (5 nm) nanodiamonds are required[139]. The photoluminescent and optical scattering properties of NDs, enhanced when functionalized[140] with nitrogen groups, combined with their biocompatibility, envision their usage for bioimaging materials in animals and humans[141]–[143]. Additionally, nanodiamonds when excited by laser, defect centres within NDs emit photons that are capable of penetrating tissue, making them well suited for bio-applications[140], [144], [145]. Some studies reveal that the photostability of

fluorescent NDs (FNDs) enable three-dimensional tracking of a single particle within the cell by means of two-photon-excited fluorescence microscopy[143]. FNDs have major advantages over the generally used quantum dots[146], [147] and fluorescent beads[148], namely exceptional stable emission and no photobleaching or fluorescence intermittency under continuous high energy excitation conditions, even for a single nitrogen vacancy (N-V) defect centre[149], [150]. ND particle containing a single N-V centre demonstrates ultrasensitive to electric and magnetic fields, temperature and strain[151], [152].

NDs structure consists on sp^3 hybridized carbon atoms that form a rigid diamond structure with tetrahedral symmetry, where all the four valence electrons of the carbon atom form a σ bond with the neighbouring carbon atoms. The inertness of the diamond comes from the general lack of free electrons in the bulk structure. On the other hand, the surface structure of the material is completely different from the bulk, due to the need to terminate the bonds and the relaxation at the surface. Therefore, the terminating structure on nanodiamond surfaces involves univalent species such as H or OH (hydrogen or hydroxyl) or any deliberate terminating groups to confer stabilization of the nanostructure. Another way of doing it is by converting sp^3 carbons of the surface in sp^2 [136], [153], [154]. (see Figure I.7).

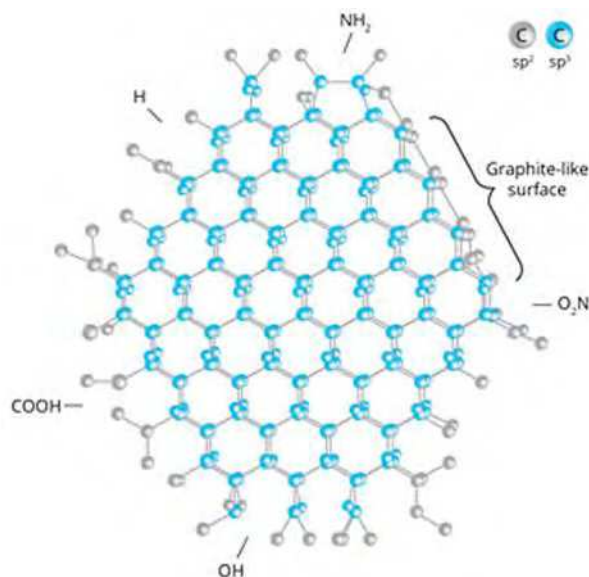


Figure I.7 - Detonation nanodiamond with surface functional groups[155]

Materials harder than conventional cubic diamonds have been developed such as wurtzite boron nitride, with a similar lattice to diamond, that has 18 % stress more than cubic diamond. Nevertheless, there is a far harder material than any other ever known, hexagonal diamond.

Simulations show that hexagonal diamonds, as lonsdaleite, withstand 58 % more stress than cubic diamond [156]. In nature, these hexagonal diamonds can be formed when the meteorites containing graphite hit the Earth. Meteoritic nanodiamonds are likely produced in a variety of sources, and several different theories have been put forth for their origins, being a very interesting example NDs formation in supernovae. Several mechanisms have been proposed for lonsdaleite formation in supernovae, including low-pressure condensation, similar to chemical vapor deposition (CVD), in expanding gas ejecta[157]; shock metamorphism of graphite or amorphous-carbon grains driven by high velocity collisions in ejecta shock waves[158]; annealing of graphite particles by intense UV radiation[159] and irradiation-induced transformation of carbonaceous grains by energetic ions[160]. It has been lately proposed nanodiamond condensation by CVD mechanisms in circumstellar atmospheres of carbon stars[161] and in nebulas[28].

Most of the applications of NDs, namely diagnostic, imaging, single-spin sensors in nanomagnetometry[151], [152] and therapeutic agents in biomedicine[132] for cryptography and quantum computing in quantum information processing, are possible to be accomplished due to the unique optical and magnetic properties associated with point defects in diamond. Since NDs have a wide bandgap atomic defect or impurities can often appear, make them highly luminescent being therefore possible to use them as cathodoluminescent, photoacoustic or fluorescent imaging agents[132].

Nitrogen is one of the impurities most commonly incorporated into the crystal lattice as isolated substitutional N atoms or two nearest-neighbor substitutional N atoms, among other numerous N-containing defects (see Figure I.8). Vacancies trapped by nitrogen atoms form different colour centres, depending on the type of N state in diamond. N-V centre consists of a defect formed in the diamond by one substitutional nitrogen atom and an adjacent vacancy (see Figure I.8(a)), which is responsible for diamond's red/near-infrared fluorescence, while a N-V-N colour centre, also designated as H3, is a nitrogen-vacancy-nitrogen complex (see Figure I.8(b)) with bright green photoluminescence[28], [162].

N-V-N colour centres can be easily generated by radiation damage of diamond with 1–2 MeV electron beams, followed by heat treatment at temperatures around 800°C¹²⁷. Defect centre

carrying a negative charge (N-V)⁻ can result from thermal annealing with radiation of nanodiamonds with a size between 35-140 nm at temperatures above 800 °C[163].

Figure I.8 – ND particles containing (a) N-V-N centres and (b) N-V configurations.

In conclusion, NDs containing colour centres have bright fluorescence and no photobleaching, which combined with their facile surface functionalization and biocompatibility turn NDs into ideal bioprobes for cell labelling and molecular imaging.

I.5.3.1. Methods of synthesis

Nanodiamonds are allotropes of carbon that have obtained significant interest in the last few years from scientific and industrial world and due to their outstanding characteristics. Nowadays nanodiamonds, namely hexagonal ones, exist in nature in very small amounts, therefore, lab synthesis methods have been widely developed. The commercial interest of NDs is accompanied by the challenge of finding industrial level, controllable and reproducible synthesis processes.

The most common technique used for diamond production is detonation synthesis technology[164], discovered for the first time by the Russian scientists in the 1960s, where charges of explosive substances are employed and subsequently detonated in high strength around hermetically sealed chambers. Several drawbacks exist in this method, very high pressures are achieved (approximately 200k atm) and temperatures rise to 3500 °C. Besides, the detonation products, also called “detonation soot” comes in aggregate form and is contaminated with impurities that include metals and other carbon allotropes, being necessary to submit them to a chemical and/or physical purification process. The products of the detonation are diverse and must then be treated to obtain pure NDs. The range of detonation UNCDs produced in the

market goes from cubic diamond to higher order non-cubic polytype[165], being the last ones appearance due to the rapid and short-lived transformation to the more dense crystal structure. The so-called high-pressure high-temperature (HPHT) growth technique[166], which was first marketed by General Electric and has been used for “industrial” production of diamond for several decades. This method consists in compressing carbon-based materials (diamond[167], fullerenes[168], [169], carbon nanotubes[170], graphite, etc), reaching tens of thousands of atmospheres and high temperatures in the presence of a metal catalyst, producing diamond in the form of single crystals ranging in size from nanometers to millimeters, which limits the range of applications.

Also laser methods have been used, including pulsed laser ablation (PLA) of carbon materials in water/alcohol[171], [172] and irradiation of ethanol with a femtosecond laser[173]. Laser methods offer the advantage of, in a single step, producing pure nanodiamond with uniform size, but these methods are highly expensive since they require advanced laser setups and don't allow high production rates. Although these methods are commercially available they require extreme conditions (high pressures and temperatures) and other chemical treatments that compromise the final product.

Other methods such as chlorination of carbides[114], electron irradiation of carbon ‘onions’[174] and ultrasound cavitation[175], ion irradiation of graphite[176] and autoclave synthesis from supercritical fluids[177] are used for NDs synthesis.

However, most nanodiamonds, onion-like structures and other carbon materials research has been dedicated to identify suitable synthesis and purification methods, most of the existing production methods still grieve from either limited scalability, lack of process and subsequently material quality control, and require complex, expensive processing equipment and multi-step processing systems.

Therefore, it is vital to develop a method to produce NDs in a form that allow their outstanding properties to be exploited. Nowadays, the most important difficulty to overcome in the nanomaterials industry is the control on the homogeneity of the nucleation process of pure nanomaterials (chemically and structurally). Their production is a quite challenging task since the final structure and structural stability of a particle is largely dictated by the surface atoms, i.e. termination groups.

I.5.3.2. Plasma-based methods

Plasma based methods revealed to be very useful for material processing since they provide a unique environment capable of dissociating complex molecules, offering an attractive route for synthesis due to the high controllability of the process, reflecting in a detailed control of the produced material by simply adjusting plasma parameters.

Chemical vapor deposition (CVD) has been used for diamond films synthesis[178]–[182], as well as hot filament CVD using Ar/H₂/CH₄ as precursor[183], pulsed linear antenna microwave plasma[184], pulsed laser deposition at room temperature[185], dual DC/RF plasma system for hydrogenated diamond like carbon deposit[186]. Researchers have been making some progresses in the nanomaterials production processes, expressly in microwave plasmas. Stacey group[181] showed that microwave plasma enhanced CVD is able to produce NDs at low pressure conditions. It consists on growing individual single crystalline nanodiamonds from nanodiamond seeds on silicon and sapphire substrates. This study allowed to understand the importance of the microwave power density applied to the system on the crystal morphology. NDs dimensions ranged the hundreds of nanometers. Later on, Kim et al[187] showed that a microwave-excited atmospheric pressure plasma jet is able to produce different carbon nanostructures, including diamond-like ones. Graphite and amorphous carbon were synthesized using gas mixtures of Ar/CH₄. The addition of hydrogen to the mixture lead to the formation of diamond-like structures. The deposits are composed by ball-like particles of 100-300 nm in diameter. These dimensions disable their usage in biological applications. Some very interesting results have been achieved, but all these methods require substrates and/or seeding processes to enhance the growing process. Consequently, being one of the main disadvantages the necessity to use chemical agents to transfer the material, leading to final product contamination.

More recently Kumar et al[188] used a microplasma to dissociate ethanol, obtaining cubic, n and lonsdaleite diamond phases at near ambient conditions. Particle size obtained were between 2-5 nm. It was proved by this research that with the hydrogen addition to the gas mixture it is possible to increase the purity of the synthesized product, allowing the production of pure nanodiamonds, besides graphene and amorphous carbon which are always present in the synthesized samples. The counter parts of this method rely on the non-scalability of the process and on the lack of control of particle size, surface chemistry, type of the synthesized structures

and respective doping process. A large amount of amorphous carbon as evidenced by Raman spectroscopy and XRD results is to be noted.

Despite the advances in techniques such as biased enhanced nucleation, the synthesis of individual and dispersed high quality (i.e. pure) free-standing nanodiamond crystals is still a challenge. For most of the existing plasma methods seeding or treatment of the substrate is required to initiate and/or enhance the nucleation process. Other techniques include polishing of the substrate with diamond powder, ultrasonic treatment of the substrate with micron diamond powder[189] or nucleation from energetic species[190]. The advantages of the PLA technique, such as reproducibility of the process and the purity of the obtained material, are nevertheless counter-balanced by the low production rates and by the high-costs. Besides all the advances, it is expected that mechanical as well as harsh chemical treatments would damage and contaminate the final product, i.e. nanodiamond.

In conclusion, the biggest challenge is to create synthetic route for NDs controllable synthesis without using harsh chemistry and extreme conditions. It is a challenge to tailor plasma and corresponding processes in order to have selective synthesis of one carbon allotrope.

Therefore, since the existing methods have critical limitations, in the present work a catalyst-free microwave plasma-based single step process at ambient conditions was developed to synthesize very promising diamond-like structures. This method brings novelty to this field since it will allow to produce free-standing NDs, therefore not requiring transition metals as substrates. By tailoring the plasma conditions, as power applied, precursor fluxes and consequently gas temperature, residence time, etc, it will be proved that carbon materials with different morphologies can be synthesized, such as cubic, n and hexagonal diamonds. Moreover, by adjusting the plasma parameters, it will be possible to achieve selective synthesis[191], [192]. Another big advantage of this method is the scalability of the process[93]. In addition, the formation of nanodiamonds at atmospheric pressure will confer also the remarkable stability of the synthesized nanostructures in modern technologies such as coating of polymeric substrates and drug delivery.

I.6. Material characterization techniques

I.6.1. SEM and TEM

Scanning electronic microscopy (SEM) [104], [193]–[195] is a technique that uses an electron beam of high energy in a way to generate several signals on the surface of the sample. The resulting signals of the interactions between the samples and the electrons give information about the sample, including morphology, chemical composition, crystalline structure and materials orientation. These devices have a magnification from 20 times till 80000 times and a special resolution between 1 nm to 100 nm and produce a 3D like image. The important signal here are the secondary electrons in a way to produce SEM images. In standard detection mode, operating in secondary electron image (SEI), this technique can produce very high-resolution sample images (less than 1 nm).

Transmission electron microscopy (TEM)[194], [196] is a microscopy technique in which a beam of electrons is transmitted through an ultra-thin specimen, interacting with it. From the interactions it is possible to obtain an image that is amplified and focused with a device for those purposes. This technique is good to observe atomic images and also to study the number of graphene layers and determine its thickness. To identify a monolayer just one dark line is observed, and if several lines are observed, it indicates presence of a multi-layered graphene.

I.6.2. SAED

The selected area electron diffraction (SAED)[193], is a crystallographic experimental technique that can be performed inside a transmission electron microscope (TEM). A thin crystalline sample is exposed to a parallel beam of high-energy electrons (energy that can go from 100-400kV). The obtained image is a series of spots which represent the selected area diffraction pattern, which is made under broad, parallel electron illumination and it is defined when the “selected” area is chosen. SAED can provide the information about the number of layers, more specifically if it is mono or multi-layered graphene. Monolayered graphene has a 2D crystal lattice, which indicates there is only zero-order Laue zone in its reciprocal space. And if the intensities observed on obtained image do not vary according with the change of the angle of incidence with the sample it indicates the presence of a mono layered graphene.

I.6.3. X-Ray

X-ray diffraction technique is widely applied for material characterization. The X-ray wavelengths have more or less the size of an atom, therefore, X-rays can be used in diffraction applications, they allow to know the structural arrangement of atoms and molecules. The x-rays used in these applications have energies in a range from 1keV to 120keV, with wavelengths between a few angstroms to 0.1 Å, and since they are very energetic, they can penetrate very deep into the samples.

I.6.3.1. XRD

X-ray diffraction (PXRD)[197]–[199] is a rapid analytical technique primarily used for phase identification of a crystalline material. In this technique a sample generally in powder form is analysed in order to study the compounds of the crystalline grains, but it is also possible to characterize particles in suspension particles or polycrystalline solids, such as thin films. Transmission and reflection geometry are the two different ways to collect powder diffraction data. In both methods the obtained information would be the same because of the powder orientation, which is random. In most experimental setups of XRD a diffractometer or a custom built 4-circle diffractometer are either used.

Figure I.9 - Reflection and Transmission geometry (XRD).

Using just one diffractometer the data is measured in reflection mode, which is mostly used for solid samples. On the other hand, if the custom built 4-circle diffractometer is used, the data is measured in transmission mode, which is most suitable for liquid phase samples.

The obtained data corresponds to the intensity detected by the diffractometer for each scattering angle (2θ) (see Figure I.9).

I.6.3.2. NEXAFS

Near-edge X-ray absorption fine structure (NEXAFS) spectroscopy and XPS are often used to determine the near surface region elemental composition[200]–[202]. Both techniques are similar, since they are based on the interaction of incident x-ray photons with matter but have distinct differences. In a XPS process the core electron is excited to the vacuum and collected, providing the core level binding energy information of the detected electrons, while in a NEXAFS one, core electrons are excited to the unoccupied orbitals above the Fermi level, obtaining consequently the information concerning the unoccupied states. Nevertheless, when combined, they provide valuable information about the surface.

Up to now, synchrotron-based spectroscopic techniques have contributed meaningfully to a better understanding of electronic and structural properties of materials at the macroscopic and microscopic scale level. They are commonly used on a variety of fields, including life sciences, biology, chemistry and materials. NEXAFS spectroscopy is a technique that can reveal not only the electronic structure of the material but also information concerning the orientation of adsorbed molecules. Surface properties play a significant role since they determine the interaction of an object with the surroundings and NEXAFS allows the identification of the bonds within the topmost layer of the surface (~ 2 nm). The NEXAFS technique was created in the 1980s, mainly to determine the structure of molecules bonded to surfaces, particularly intended to be applied to low-atomic number molecules, i.e. mostly organic molecules such as carbon, nitrogen, oxygen and fluorine.[203]

It normally detects transitions from the K-edge, the deepest core shell, of an atomic species into empty molecular orbitals of bonds to intra-molecular and extra-molecular neighbours, i.e. surface atoms, leaving a hole in the core shell.

During a measurement the sample is irradiated with monochromatic X-rays and their energy varies around an ionization edge. The dominant process in the soft X-ray energy range (~ 2000 eV) is photo-absorption. The absorption process results in a photoelectron and a core hole. The hole is subsequently filled by an electron either radiatively by the emission of a fluorescent photon, or non-radiatively by the emission of an Auger electron (see Figure I.10). Both channels are a direct measure of the existence of a core hole created by the X-ray absorption and are therefore a measure of the absorption cross section.

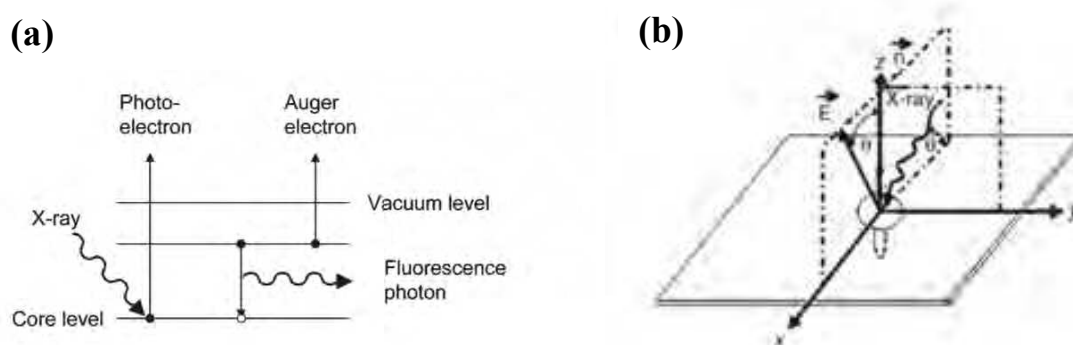


Figure I.10 – (a) Energy diagram of the photo-absorption process and the subsequent filling of the hole by emission of a photon or Auger electron. (b) Representation of the geometry of π^* vector orbitals (vertical to the xy plane) and σ^* planes (within the xy plane) with respect to the incident beam and the electric field vector, E[204].

Depending on the core electron excitation different edges are considered, namely K-, L-, and M-edges, which correspond to the quantum numbers $n=1, 2$ and 3 , respectively (see Figure I.11). For a better understanding, excitation of a $1s$ electron occurs at the K-edge, while excitation of a $2s$ or $2p$ electron occurs at an L-edge.

NEXAFS involves the excitation of electrons from a core level to partially filled and empty states. The decay of core hole states results in the emission of Auger electrons from valence molecular orbitals, resulting in a NEXAFS electron yield spectrum. Hence, the peak positions and spectral line-shape in a NEXAFS spectrum are directly related to the nature of these unoccupied electronic states. Decay of core holes may also occur via the emission of fluorescent photons, which originate from the top 200 nm of the film as opposed to Auger electrons, which arise from the top 10 nm. Thus, this technique is both surface and bulk sensitive and is capable of probing both graphene electronic structure as well as surface functional groups simultaneously.

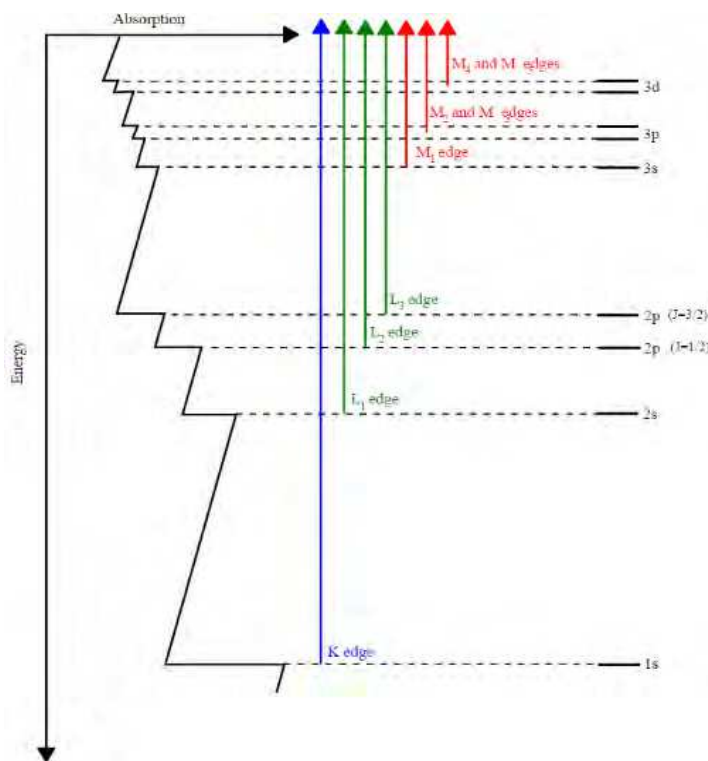


Figure I.11 – Schematic of showing the different levels of the core electron.

I.6.4. Raman

Raman[205] is a high resolution photonic technique used to obtain chemical information from organic and inorganic samples. This technique relies on Raman scattering (inelastic scattering) of a monochromatic light with a certain frequency that hits a sample and disperses. Most of the dispersed light has the same frequency (Rayleigh dispersion). Furthermore, due to the inelastic dispersion (Raman dispersion), the remnant dispersed light has a different frequency, and the information given by that is important to identify the molecular composition of the sample. The Raman dispersion is based on the Raman Effect, a phenomenon of inelastic scattering of light throughout matter. Raman spectroscopy is used to determine the thickness of graphene layers, as well as to study the strain effect, doping effect, misoriented bi-layer graphene and crystallographic orientation of graphene.

I.6.5. FTIR

Fourier transform infrared spectroscopy (FTIR)[205], [206] is a technique used to obtain an infrared spectrum of emission, absorption, photoconductivity or Raman scattering of a solid, liquid or gas specimen. In order to obtain an absorption spectrum while a sample is shined

by a beam containing a range of light frequencies at once, the amount of light absorbed by the sample is being measured. The beam described above is generated by a broadband light source, containing the full spectrum of wavelengths to be measured. The light shines into a Michelson interferometer (Figure I.12) that consists on a beam splitter, a fixed mirror, and a mirror that translates back and forth, very precisely. As the mirror moves, each wavelength of light in the beam is periodically reflected, transmitted, reflected, transmitted, by the interferometer, due to wave interference. Basically, the beam is divided in two when it reaches the beam splitter.

Figure I.12 - A Schematic of a generic Michelson interferometer.

Half of the beam is transmitted, and the other half is reflected. Subsequently FTIR spectrometer collects and digitizes the interferogram, performs the FT function, and displays the spectrum. The infrared portion of the electromagnetic spectrum is usually divided into three regions; the near-, mid- and far- infrared. The higher-energy near-IR covers approximately the region from 0.8 to 2.5 μm , and that radiation excites overtone or harmonic vibrations. The mid-infrared covers approximately the range 2.5–25 μm , which is mostly used to study the fundamental vibrations and associated rotational-vibrational structure. The far-infrared covers approximately the region from 25 to 1000 μm , which lies adjacent to the microwave region, in result low energy radiation, and is usually used for rotational spectroscopy.

FTIR spectroscopy can be considered a simple and robust method to analyse functionalised graphene. Although in some cases absorption bands from the fingerprint region are almost impossible to distinguish due to the overlapping of several signals, this technique has played an important role in revealing some specific functional groups.

On the other hand, FTIR spectroscopy is also very commonly used to analyse the plasma outlet gas stream. To monitor the molecules decomposition mechanisms caused by plasma processing[23], [93].

Chapter II. Experiments, results and discussion

II.1 - Microwave plasma-based method used for 2D and 3D carbon nanostructures synthesis

II.1.1 - Mass production of high-quality free-standing graphene and N-graphene sheets using an Argon-Ethanol microwave plasma

II.1.2 - Synthesis of complex carbon structures using different precursors

II.2 - N-doping of graphene using a Ar-N₂ microwave remote plasma treatment

II.3 - Graphene applications using plasma-based methods

II.3.1 - Samples preparation for plasma treatment/polymerization

II.3.2 - Polymer-graphene nanocomposites using a plasma polymerization method

II.3.3 - Graphene functionalization for biosensing applications

II.1. Microwave plasma-based method used for 2D and 3D carbon nanostructures synthesis

A microwave atmospheric plasma torch driven by surface waves is used to synthesize carbon nanostructures[3], [93]. A wave-guide surfatron-based setup is used to create a surface wave induced microwave plasma at atmospheric pressure conditions. The 2.45 GHz radiation at up to 2 kW is provided by a microwave generator (Sairem). The generated plasma has an extended active zone outside the wave launcher, as seen in Figure II.1, since it is sustained by the field of a travelling wave that simultaneously propagates and creates its own propagation structure. In this way, large microwave power densities can be delivered into the processing area and create high population densities of active species of interest. The discharge takes place inside a quartz tube which is inserted vertically and perpendicularly to the waveguide widest wall. The background gas, i.e. argon, is injected to which is added a hydrocarbon precursor, i.e. ethanol (C_2H_4OH)/methane (CH_4), mixed with other gases such as carbon dioxide and hydrogen, through an inner tube. The nanostructures are then collected by a collecting system.

This experimental setup can be divided in six functional modules. The first module refers to the microwave generation, the second to the power transference from the microwave generator to the plasma – waveguide elements, the third to the gases extraction and cooling systems, the fourth to the pressure control on the nanostructures deposition chamber, the fifth to the control of exhaust gas stream temperature and lastly the sixth to the control and monitoring of partial and total fluxes.

Module I – Microwave Generation

A generator SAIREM GMP 20K SM 56M230 FST 3 with IR mode is used. It is composed by a high-voltage power supply and a magnetron. The High-Voltage power supply can work in different modes (pulsed, continuous, etc). It's fed with a three-phase current for $208\text{ V} \pm 10\%$ and $400\text{ V} \pm 10\%$, being also possible to work in a 230 V one-phase.

Figure II.1 – Experimental setup used for synthesis of carbon nanostructures.

In addition, the output power can go from 300 W to 2 kW and the reflected power up to 400 W. The magnetron works at 2.45 GHz and has an output internal cross-section of 86x42 mm, typical dimension for WR340 waveguide type elements. The magnetron has a refrigeration system connected to a circulator/isolator, where the reflected power is dissipated. Furthermore, when the circulator detects a reflected power over 400 W, a safety procedure is activated, the magnetron turns off.



Table II-1 – SAIREM GMP 20K SM 56M230 FST 3 IR. (left) Power supply. (right) Microwave head.[207]

Module II – Waveguide elements

The module of the waveguide elements guides the power to the microwave launcher. All the elements are placed on top of a metallic bench. It is also important and vital that this elements segment is electrically connected to the metallic bench to prevent the existence of high voltages in order to assure the safety of the people as well as of the material. As it can be seen on Figure II.1, right after the magnetron, there is a WR340 waveguide system, which includes a (3-port) isolator, directional couplers, a stub tuner, a waveguide-surfatron as the field applicator and a movable short-circuit. The 3-port isolator has 3 ports, in which port one corresponds to the output of the magnetron, port two links this element to the rest of the waveguide structure and port three corresponds to a cooling system with water circulating. Ideally the power goes directly from port one to port two and the reflected power goes from port two to port three, in which power is dissipated. The 3-stub tuner on the waveguide minimizes the reflected power. The adjustable short-circuit linked to the waveguide-surfatron is used to assure a high power in the centre of the quartz tube, consequently having a minimum power value at port three, at the isolator. The waveguide-surfatron (see Figure II.2) where the microwaves are launched in order to generate and maintain the plasma, has a quartz tube that is placed vertical and perpendicularly to the waveguide. Inside the quartz tube where the discharge occurs there is another tube with internal and external radii of (1.5 ± 0.5) mm and (2.5 ± 0.5) mm, respectively, which is used to introduce the vaporized precursors. The waveguide-surfatron is a surface wave launcher that creates a wave propagating along the interface between the plasma and the dielectric tube surrounding it, which in this case is quartz. The waveguide-surfatron combines a rectangular waveguide with a cylindrical launcher, which is attached perpendicularly to the

waveguide and consist on a metal housing that completely shields the plasma tube, save for a small gap of air. Usually connected to the waveguide is a short-circuit that could be adjustable in order to optimize the field strength at the gap for different loads. The adjustable short-circuit is used to create a standing-wave pattern. The field configuration is TE₁₀, where the electric field is parallel to the discharge tube.

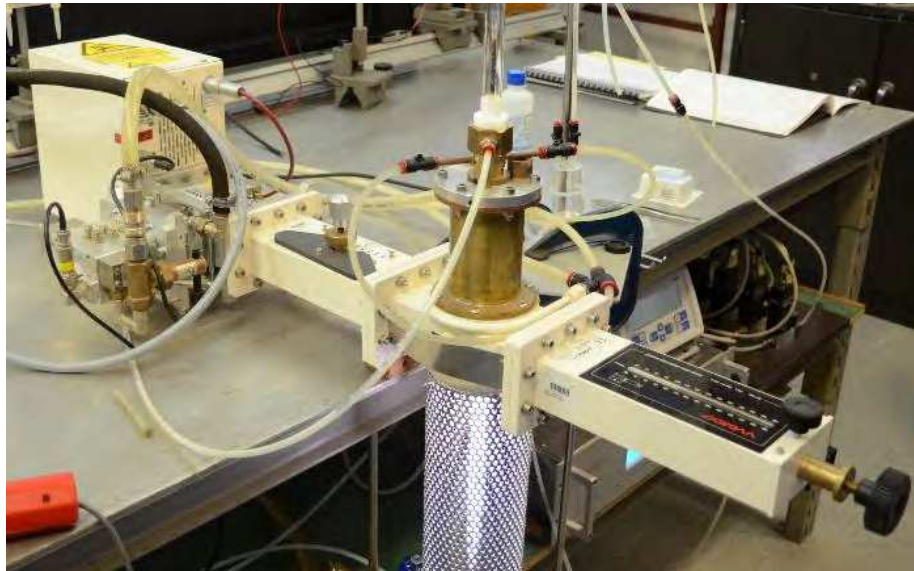


Figure II.2 – Waveguide elements.

Module III – Gas extraction and cooling system

The module of gas extraction and cooling system includes a cooling system of the discharge quartz tube with compressed air, in order to prevent the overheating of the tube, because of the high-power levels that are reached while the experiment is running. It also includes a cooling system with water to cool down the gap in the waveguide-surfatron and a cooling system to cool down the magnetron in the isolator, port three, to prevent the reflected power to reach the magnetron, dissipating the power in the cooling system with water circulating. Gases extraction comprises adjustable metallic pipes of (120 ± 5) mm of diameter and a turbine within that is capable to assure fluxes of 190m³/h. Connected to this structure are PVC tubes to guide the gases to the outside of the building.

Module IV – Control and monitoring of partial and total flux

Figure II.3 – Flow controller - Brooks 0254 series readout.[208]

The flow rates needed to create the appropriate conditions to synthesis of the nanostructures are controlled by Brooks 0254 Readout (see Figure II.3) coupled with two flow-meters. The background argon gas is injected into the discharge tube (external tube placed on the middle of the waveguide-surfatron) with flow rates between 250 sccm to 2000 sccm under laminar gas flow conditions. The partial fluxes (gas phase and/or vaporized precursors into the internal tube) are injected with flow rates from 5 to 120 sccm. The vaporized precursors, go as into the internal tube placed on the waveguide-surfatron. In order to become vaporized, previously, the liquid precursor is mixed with the background gas in a nebulizer (see Figure II.5). The vaporization is performed at room temperature by passing argon gas through a porous filter, composed of bonded grains of quartz glass immersed in the precursor liquid inside the tank at 40°C. The gases are carried by LLDPE tubes (Linear Low-Density Polyethylene) and the flows control is made by flow-meters and electrical-valves.

Module V - Control of outlet gas stream temperature

The temperature in the nucleation zone of the plasma reactor is essential for synthesized nanostructure, i.e. particles or sheets. For this reason, in order to provide external forced cooling/heating of the outlet gas stream a cryostat or IR lamps (see Figure II.1) have been used.

Module VI – Collecting system

The nanostructures were captured by a tornado type Hurricane Cyclone system® followed by a methanol trap (Figure II.14). Using these two stages containers we obtain larger particles in the first container and smaller ones in the methanol trap. The methanol trap avoids the nanostructures with reduced dimensions to escape the system with the exhaust gas, being this an eco-friendly measure.

Figure II.4 – Hurricane Cyclon System® used to collect the nanostructures produced.

II.1.1. Mass production of high-quality free-standing graphene and N-graphene sheets using an Argon-Ethanol microwave plasma

One of the greatest challenges in the commercialization of graphene and derivatives is the production of high-quality material in bulk quantities at low price and in a reproducible manner. The very limited control, or even lack of, over the synthesis process is one of the main problems of conventional approaches. For this propose, a microwave plasma is used in this part of the project, since plasma enables scalable route for continuous, large-scale fabrication of free-standing graphene and nitrogen doped graphene sheets. The method's crucial advantage relies on harnessing unique plasma mechanisms to control the material and energy fluxes of the main building units at the atomic scale. By tailoring the high energy density plasma environment and complementarily applying in-situ IR and soft UV radiation, a controllable selective synthesis of high-quality graphene sheets at ~ 2 mg/min yield with prescribed structural qualities was achieved. Raman spectroscopy, scanning electron microscopy (SEM), high resolution transmission electron microscopy (HRTEM), X-ray photoelectron spectroscopy (XPS) and Near Edge X-ray-absorption fine-structure (NEXAFS) spectroscopy were used to probe the morphological, chemical and microstructural features of the produced material. The method described here is scalable and show a potential for controllable, large-scale fabrication of other graphene derivatives and promotes microwave plasmas as a competitive, green, and cost-effective alternative to presently used chemical methods. Part of the work presented in this section was published in Nature Scientific Reports [209].

II.1.1.1. Experimental proceedings

The discharge takes place inside a quartz tube that contains a section with expanding radius, which was designed to satisfy specific thermodynamic conditions (gas velocity, thermal fluxes, residence time etc) in the "assembly zone" of the plasma reactor (see Figure II.5).

Figure II.5 – Large scale setup used for mass production of free-standing graphene sheets.

The gas passing through the discharge results from the mixture of direct argon flow and the combined flow of argon and carbon-based precursor, i.e. ethanol. To increase control over the synthesis process and improve the structural quality of the assembled flowing nanostructures being dragged by the background gas flow both infrared (in-situ annealing) and soft UV radiation ($\lambda=300-400$ nm at 4 W) were applied in the post-plasma zone, where nanostructures assemble and grow. This system allows removal of the epoxy oxygen groups and sp^3 carbons during the flight to a tornado-type Hurricane Cyclone collecting system[210] of the free-standing graphene sheets. A methanol trap connected to the exit of the Hurricane system is used to capture the smallest particles that can escape the system with the gas flow. (see Figure II.5) For the N-graphene synthesis nitrogen atoms can be incorporated within the carbon nuclei via careful plasma tailoring and their density can be effectively controlled by the percentage of N_2 flux in the precursor gas mixture[211].

II.1.1.2. Basic Workings

The plasma reactor can be considered as the assemblage of three different zones, as presented in Figure II.6.

Figure II.6 – Scheme of the process.

The first is the surface wave sustained discharge zone, including the zone inside the launcher and the extended “hot” plasma zone outside the launcher. Here, the wave power is absorbed primarily by plasma electrons, which transfer the power to heavy particles via elastic and inelastic collisions resulting in gas temperatures up to 4000 K (see section II.1.1.3 - Tailoring plasma environment)[212]. The gas temperature decreases slightly when moving away from the launcher up to about 15 cm before dropping considerably in the “mild” plasma zone (20 - 30 cm from the launcher). Carbon precursors are injected in the “hot” high energy density zone. Due to the collisions involving electrons and heavy particle along with intensive radical’s chemistry, decomposition processes of the injected carbonaceous molecules, i.e. C_2H_4OH , take place. The created radicals become precursors of chain reactions leading to creation of the main building blocks of carbon nanostructures, i.e. carbon atoms and C_2 radicals[212]. It is worth to notice, that the assembling process requires very fast delivering and stacking of building units and equally fast supply of energy sufficient to overcome all the actual potential barriers. In the “mild” plasma zone, which includes also the “near” plasma afterglow, gas temperature drops from about 2000 K to 500 K. Note that the gas temperature changes also in radial direction, following closely a parabolic profile, due to the radial thermal losses. The transport of gas-phase carbon

atoms/molecules into a colder zone through the so-called surface of vaporization (bold blue solid line in Figure II.6)[212] results in transformation into solid carbon nuclei. Here, the schematic presentation of the isothermal plasma surface with constant temperature is marked as “vaporization surface” (see supporting results in section II.1.1.3 - Tailoring plasma environment). The transport of plasma generated carbon atoms/molecules into colder zones (outside of the vaporization boundary) of the reactor results in formation of solid carbon nuclei that are gradually withdrawn in the outlet plasma stream where kinetic processes of assembly and growth of “flowing” carbon nanostructures take place.

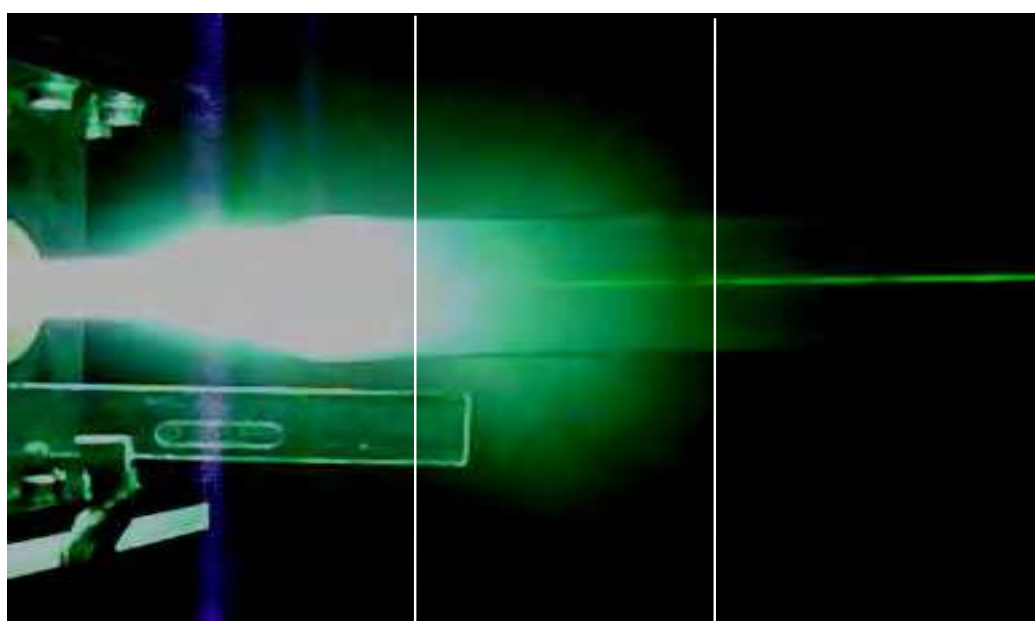


Figure II.7 – Image of the plasma and flowing nanostructures irradiated by laser beam.

The three zones can be clearly distinguished in the photograph of plasma reactor (Figure II.7). The incident laser (532 nm, 1 W power) beam is scattered from the “flowing” nanostructures, causing it to appear as a discontinuous green line on the photo. The scattered light from growing nanostructures appears in “the” mild plasma demonstrating that the graphene sheets are assembled and grown rapidly after crossing the vaporization surface”. The nanosheets, being created in the plasma zone where ultrafast electrons rapidly settle on their surfaces, are negatively charged.

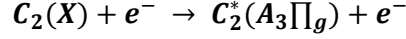
Using a cylindrical reactor with expanding radius allows the injection of large power density in the sections with smaller radius and achieve larger fluxes of building units (C_2 , C) with

sufficiently high energy that will then flow towards “mild” plasma zone, i.e. assembly zone of the reactor. Once in the larger volume, the departure from the supersaturation conditions of the environment, prone to foster nanosheets assembling, is preserved [4], [23]. That is, the existence of a smaller amount of nuclei surpassing the critical size for nucleation and growth and conditions in which no supersaturation of species is possible promote the growth of existing nuclei rather than creation of new seeds. The reduction of Gibbs free energy of the system is behind the processes of nucleation and growth. This reduction of the Gibbs free energy of a saturated environment (e.g. plasma + solid phase) is proportional to the gas temperature. Lower gas temperatures, as well as larger number densities of building units, foster supersaturation conditions in the environment and thus promote the synthesis of plenty nuclei and amorphous structures are more likely to be created. Contrarily, lower number density of nuclei and higher temperatures lead to a deviation from supersaturation conditions, more prone to generate graphitic sheets. As expected, in the larger volume, the density of carbon nuclei decreases, and, as a result, the conditions favour the creation of planar nanostructures.

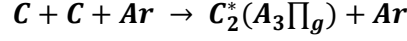
II.1.1.3. Tailoring plasma environment

To identify the species of interest and to determine important plasma parameters such as the gas temperature and the electron density in the discharge "hot" zone, plasma emission spectroscopy has been performed. Optical emission spectroscopy allows to identify the active carbon species in the plasma that are the “building units” providing the synthesis and growth of the carbon nanostructures in the outlet plasma/gas stream. The detected argon/ethanol plasma emission spectra in the visible range (350-720 nm) are shown in Figure II.8. The emission of OH ($A^2\Sigma^+, v=0 \rightarrow X^2\Pi_i, v'=0$) (300-320 nm) bands, as well as of atomic C (247.9 nm) and hydrogen Balmer-alpha line ($H\alpha$) (656.3 nm) are also present in argon/ethanol plasma. As mentioned, the experiments were carried out in the open atmosphere so that some nitrogen containing species also appear. The emission from CN species corresponding to violet system CN ($B^2\Sigma^+ \rightarrow X^2\Sigma^+$) transitions in the range 335-350 nm and 590-640 nm as well as several Ar lines in the range 600-800 nm were detected. The emission of molecular $C_2(A^3\Pi_g \rightarrow X^3\Pi_u)$ Swan system, in the range 450 – 570 nm, with heads band at 473.7, 516.5 and 558.6 nm, is clearly seen. The typical C_2 emission is generated by the radiative decay of $C_2^*(A_3\Pi_g)$ level. Due to the low energy threshold

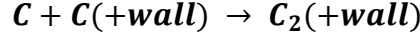
($E_{\text{ext}} = 2.4$ eV), ground state C_2 molecules can easily be excited to this level either by electron impact [213]



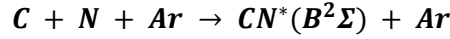
by three body recombination processes involving carbon (C) and argon (Ar) atoms



or by recombination of two carbon atoms at the quartz tube wall



On the other hand, CN species result from a three-body recombination reaction



The gas temperature in the “hot” plasma zone is a key parameter concerning ethanol decomposition. The collision rates in the plasma at atmospheric pressure are high enough to ensure local thermodynamic equilibrium. Therefore, the rotational temperature can be taken as a good approximation to the gas kinetic temperature. The emission band from CN species corresponding to violet CN ($B^2\Sigma^+ \rightarrow X^2\Sigma^+$) and OH ($A^2\Sigma^+, v=0 \rightarrow X^2\Pi_i, v'=0$) (300-320 nm) transitions were used to estimate the gas temperature in the “hot” plasma zone. An estimation of the gas temperature was obtained from measurements of the rotational distribution of CN(B-X) band in the 380-388 nm range and OH(A-X) in the 300-320 nm. The rotational temperatures were determined by fitting the experimental data to the simulated ones given by a spectra simulation program LIFBASE[214].

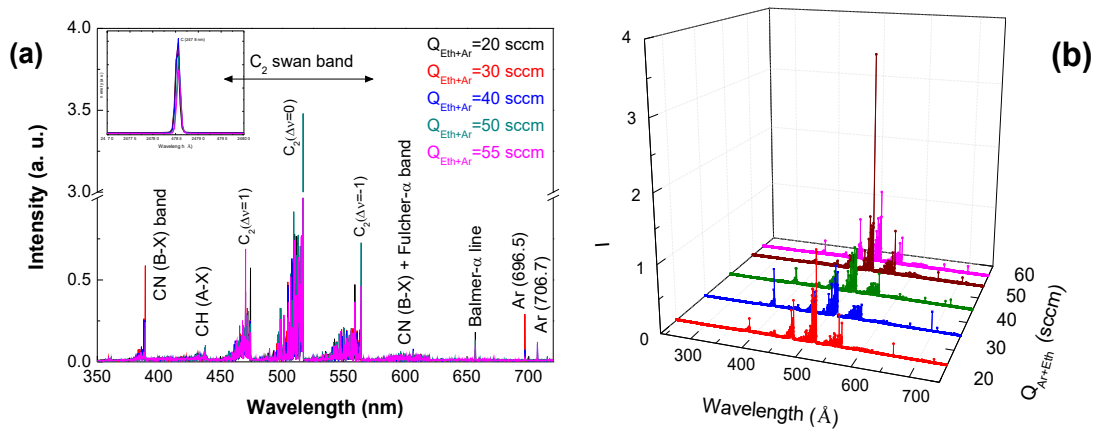


Figure II.8 – (a) Emission spectra of Ar-ethanol plasma ($p=1$ atm, $P=2$ kW, $Q_{Ar} = 1200$ sccm, $z=4$ cm). (inset) Atomic carbon emission at 247.9 nm. (b) 3D perspective of graph present in (a) for better understanding.

The estimations demonstrate that the rotational temperature measured at fixed background Ar flux (1200 sccm) and precursor fluxes in the range (20-60 sccm) remains nearly constant in the central "hot" zone (at distances 6-10 cm from the launcher position) with variation from about 4000 K to 2800 K (as it can be seen in Figure II.9), which validates the theoretical models mentioned in the previous section when describing the different zones of the reactor (see section II.1.1.2 - Basic Workings).

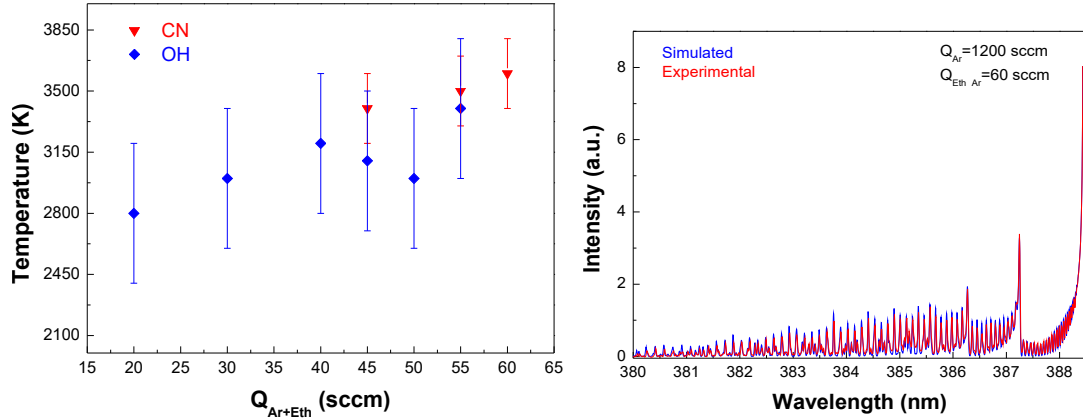


Figure II.9 – (left) Rotational temperature of CN violet (B-X) and OH (A-X) molecular bands considering different precursor (ethanol+argon) fluxes. (right) CN violet (B-X) band experimental data fit by simulated one for 3400 K given by LIFBASE program[214]. Discharge conditions: $p=1$ atm, $P=2$ kW, $Q_{Ar}=1200$ sccm, $Q_{Eth}=21$ sccm.

It should be mentioned that this temperature is associated with the axis of the "hot" plasma column, since the radiation collected originates mainly from this region. Having a much lower value close to the wall, the gas temperature exhibits a sharp radial gradient. As shown in the previous studies, the plasma reactor wall temperature, as a boundary value of the gas temperature, is one of the key parameters influencing the process of synthesis of carbon nanostructures.[3], [212] The 2D map of the wall temperature as detected by an infrared-sensitive thermal imager (FLIR camera) is shown in Figure II.10. As seen, the wall temperature remains stable at around 670 °C until 4.5 cm from the discharge, i.e. 2 cm from the injector, and reveals a sharp decrease in the section with expanded radius, reaching around 180 °C right before the IR lamp system and dropping nearly to the room temperature at about 35 cm from the launcher.

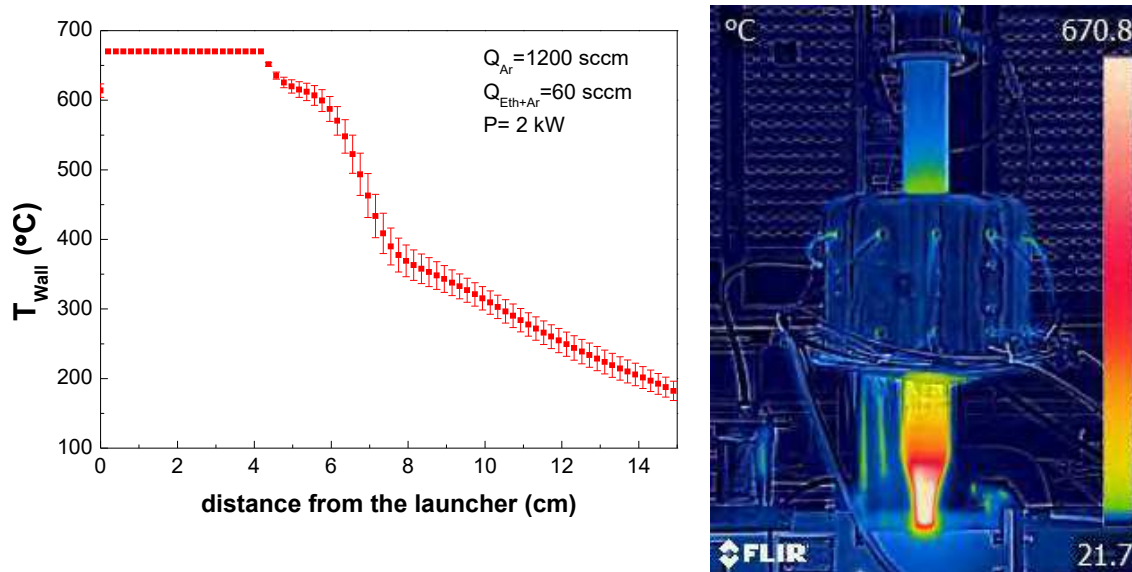


Figure II.10 – (left) Axial wall temperature profile along the tube. (right) respective thermal image of the discharge at $p=1$ atm, $P=2$ kW, $Q_{Ar}=1200$ sccm, $Q_{Eth}=21$ sccm.

II.1.1.4. Material characterization

II.1.1.4.1. Techniques

SEM

SEM characterization of the samples has been performed by a JEOL, JSM-7001F field emission gun scanning electron microscope operating in secondary electron imaging mode (SEI) using 15kV accelerating voltage. The samples were deposited on a double-sided carbon tape mounted on an aluminium stub.

Raman spectroscopy

In order to perform the Raman spectroscopy characterization, the synthesized nanostructures were freely suspended on a glass substrate and the Raman spectra from different regions on the substrate were obtained using a LabRAM HR Visible (Horiba Jobin-Yvon) Raman spectrometer at 633 nm, 514 and 458 nm with 5 cm^{-1} spectral resolution and a laser spot size of 2 μm . Measurements were performed with a laser power $P_l = 0.054$ mW to avoid overheating.

Graphene and N-graphene bonding situation was studied using a Fourier-Transform Infrared Termo Nicolet 5700 spectrometer in the wave number range $1000 - 4000$ cm^{-1} .

HRTEM

The graphene flakes were placed directly as a solid powder onto a copper grid for transmission electron microscopy (TEM). The sheets were then characterized by a high-resolution TEM JEOL JEM-2010F, operating at 200 kV accelerating voltage.

XPS

XPS spectra of N-graphene were obtained with a KRATOS XSAM800 X-ray spectrometer with double anode, operating in Fixed Analyzer Transmission mode, with analyser pass energy of 20 eV and non-monochromatic X-radiation with a power of 120 W (12 kV 10 mA). Samples were analysed at room temperature, at UHV pressure around 10^{-7} Pa and a take-off angle set to 90° . Graphene sheets were peeled from the filters using the XPS sample holder with double-side tape. The spectra were collected with 0.1 eV steps, using a Sun SPARC Station 4 with Vision software (Kratos). X-ray source satellites were subtracted. Shirley backgrounds and Gaussian/Lorentzian line shapes were fitted using XPS Peak 4.1 (freeware). No flood gun was used for charge compensation. Binding energies (BE) were corrected taking as a reference the binding energy of sp^2 carbons.

XPS characterization of pure graphene sheets was carried out on a VSW XPS system with the Class 100 energy analyser being a part of an experimental setup (Multitecnica) assembled for surface investigation. The samples were pressed onto 1 mm thin lead plates, in order to provide both mechanical support and electrical contact. The survey spectra were taken in a fixed analyser transmission mode with the pass energy of 44 eV, i.e., FAT 44, while the detailed spectra of characteristic lines were taken in FAT 22 mode. The analysis has been performed using the non-monochromatic Mg $K\alpha$ line (photon energy of 1253.6 eV). The carbon line was fitted to Doniach-Šunjić profile convoluted with pseudo-Voigt GL(70) shape2-4. The applied peak fitting model was established from the previous measurements of freshly cleaved highly oriented pyrolytic graphite. The oxygen line was fitted to pseudo-Voigt GL(30) line shapes. For the energy axis calibration, Ag (110) and polycrystalline Au samples (previously cleaned by ion sputtering) were used. The energy was calibrated to the peak position of Ag 3d $_{5/2}$ (binding energy of 368.22 eV) and Au 4f $_{7/2}$ (binding energy of 83.96 eV) lines. The samples were analysed ex-situ without cleaning, in order to avoid bond breaking.

NEXAFS

NEXAFS spectroscopy was performed on the samples using the HE-SGM beam line at BESSY II storage ring (PREVAC end station provided by Professor Ch. Wöll). NEXAFS measurements were performed considering different incident angles (20-90°) relative to the substrate surface. The data was collected in respect to the C K-edge to characterize the carbon chemistry of the produced free-standing graphene, in the partial electron yield (PEY) mode (few nm depth), using a home built double channel plate detector. The energy resolution was ≈ 0.40 eV. The raw NEXAFS spectra were corrected for the beam line transmission by division through a spectrum of a clean, freshly sputtered Au sample. Alignment of the energy scale was accomplished by using an I_0 feature referenced to a C $1s \rightarrow \pi^*$ resonance at 284.9 eV from a fresh surface of a graphite foil standard sample [215].

II.1.1.4.2. Large scale synthesis of pristine graphene

The range of operational conditions, i.e. background and precursor flow, microwave power, post-discharge conditions (in-situ annealing by IR radiation, UV treatment, etc), fostering selective synthesis (only graphene sheets) is very limited. Outside of this range different carbon allotropes, i.e. amorphous carbon, 3D and 2D structures, at the same time can be synthesized.

The precursor fluxes have been varied in the range of 5 and 100 sccm, as well as the range of the background Ar gas flux from 500 to 2000 sccm under laminar gas flow conditions. The wall temperature of the reactor in the outlet gas zone (in the region 15 to 30 cm from the launcher, where IR radiation is applied) was also varied between 150 and 260°C.

The evolution in the synthesized nanostructures as the background flux changes while precursor flux remains unchanged (5 sccm), i.e. decreasing residence time, are shown in Figure II.11.

Figure II.11 - Evolution of morphology with background gas. SEM images of samples produced at 2 KW and $Q_{Eth} = 0.6$ sccm at atmospheric pressure.

The SEM images show that different carbon nanostructures can be produced using this method as the previous prototype developed in PEL had already proved[3], [23]. The samples produced in the range 500 to 1500 have nanostructures resembling graphene sheets. Nevertheless, the main objective is to achieve selective synthesis of pristine graphene, being the sample produced with 1000 sccm of Ar the most promising one. The other samples seem to have other carbon nanostructures mainly by increasing the background flux, i.e. decreasing the residence time. Since one of the main goals is to increase the yield of graphene, the partial flux should be increased, in order to increase the density of carbon species decreases. As the precursor flux increased until 55 sccm the shape remained by eye untouched, resembling graphene foils (Figure II.12), and 2 mg/min of graphene was produced.

From previous studies it is well known that the wall temperature manipulation at the post discharge is crucial to control the quality of the produced material[3], [23]. Therefore, to control the thermodynamic conditions at post discharge, IR irradiation was applied at the reactor's outlet gas zone, i.e. the region 15 to 30 cm away from the launcher, and the wall temperature (T_{Wall}) was measured as an indicative of the amount of IR irradiation that was simultaneously applied.

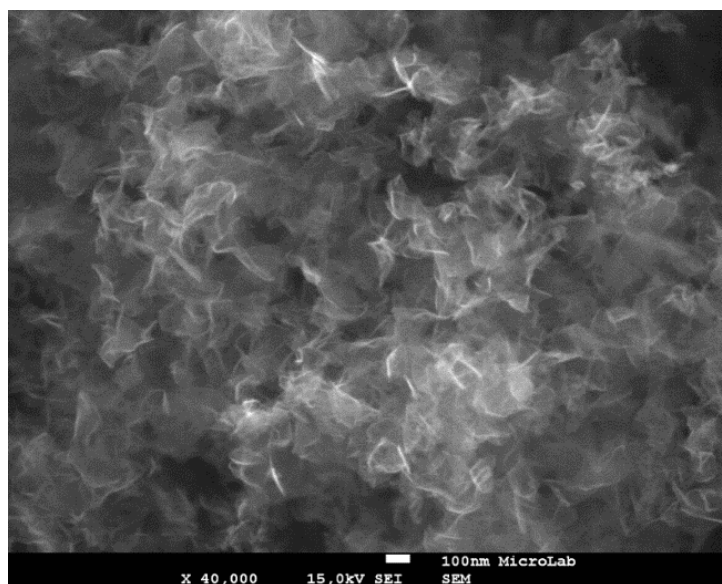


Figure II.12 – SEM image of foil-like structure resembling graphene. Sample synthesized at 2 kW, 1 atm, $Q_{\text{Ar}}=1200$ sccm and $Q_{\text{Eth}}=15$ sccm.

Raman spectroscopy is the most efficient way to provide a quick and easy structural and quality characterization of the samples. Typical Raman spectra of the synthesized carbon sheets

produced considering different plasma conditions, while maintaining an applied power of 2 kW, a precursor (ethanol) flux of 15 sccm and a background Ar flux of 1200 sccm are shown in Figure II.13.

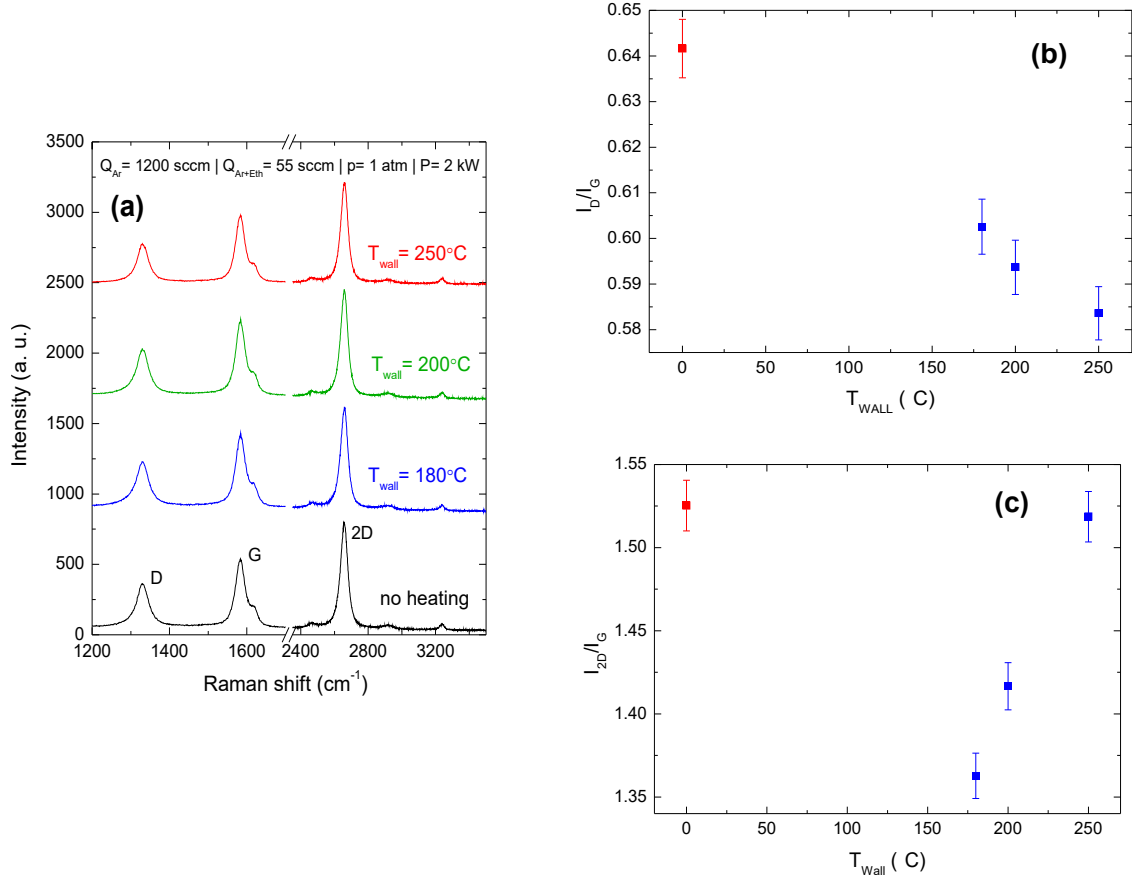


Figure II.13 – (a) Average Raman spectra obtained from three different spots of 4 different samples. Spectra were normalized to the intensity of the G peak and offset vertically for better viewing. (b) Wall temperature dependence on the intensity ratios of D and 2D peak to G peak. The red point is the reference point where no IR is irradiated at the post discharge, i.e. no control of the wall temperature. Samples produced at $Q_{Ar}=1200 \text{ sccm}$, $Q_{Eth}=15 \text{ sccm}$, $P= 2 \text{ kW}$ at atmospheric pressure

In order to perform the Raman spectroscopy characterization, the synthesized nanostructures were freely suspended on a glass substrate and the Raman spectra from different randomly chosen spots were obtained. The Raman spectra reveals very interesting results, as the wall temperature at post discharge increases, the intensities ratio of D to G peak (I_D/I_G) decreases from 0.64 to 0.58 due most probably to a decrease in the structural defects present in the graphene sheets, caused by the oxygen reduction during the annealing process in the IR irradiated zone. As the reduction process was optimized, the original 2D/G Raman intensity ratio of few-layer graphene

was recovered. Furthermore, Raman spectroscopy was performed considering 3 different laser wavelengths. The pairs of spectra, obtained with the same excitation, are practically identical, an evidence for the homogeneousness of the sample thus confirming that synthesis of only graphene sheets has been achieved. However, the relative intensity of all other lines and even their position are different, and they strongly depend on the laser wavelength used (see Figure II.14). The line, denoted with D, changes its position from 1333 cm^{-1} (in $\lambda = 633\text{ nm}$ spectra) up to 1367 cm^{-1} (in $\lambda = 458\text{ nm}$ spectra). Its relative peak intensity (according to the G line (I_D/I_G)) decreases from 0.70 to 0.20, respectively.

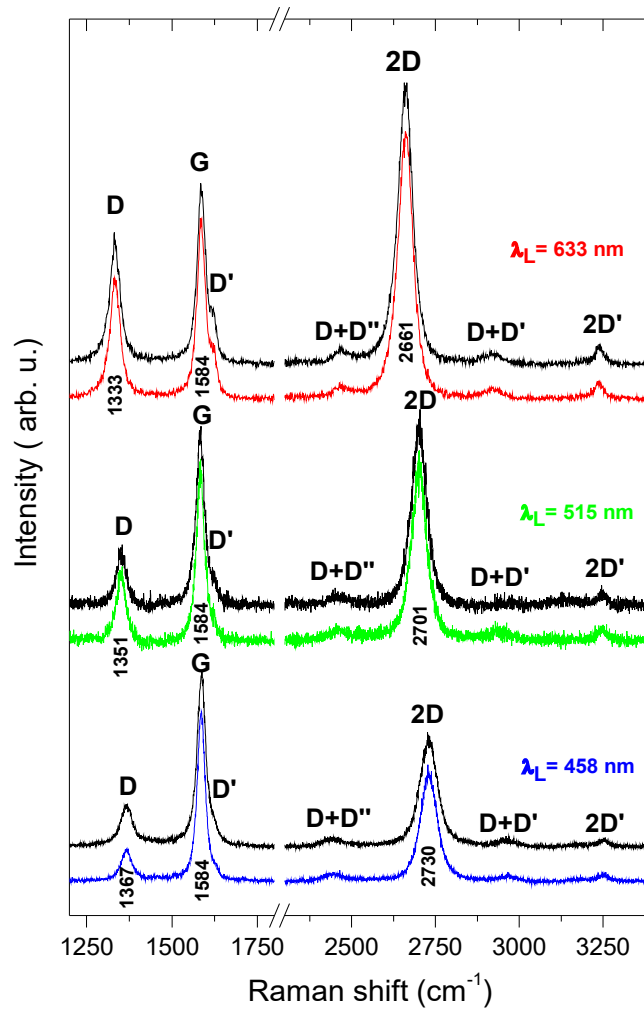


Figure II.14 – Raman spectra obtained with three excitation laser lines (633 nm, 515 nm, 458 nm) from two different spots of a single sample. Spectra is normalized in respect to the intensity of the 1584 cm^{-1} peak (denoted with G) and offset vertically for viewing purposes. Samples produced at $Q_{Ar}=1200\text{ sccm}$, $Q_{Eth}=30\text{ sccm}$, $P=2\text{ kW}$ and atmospheric pressure

The other strong line, denoted with 2D, changes its position from 2661 cm^{-1} (in $\lambda = 633\text{ nm}$ spectra) up to 2730 cm^{-1} (in $\lambda = 458\text{ nm}$ spectra). Its relative peak intensity (according to the G line (I_{2D}/I_G)) decreases from 1.60 to 0.65, respectively.

Although the primitive cell of graphene is very simple, and it contains only two carbon atoms, the Raman spectra of graphene cannot be trivially interpreted. From a symmetry point of view, only one E_{2g} mode from the Γ -point of the Brillouin zone is Raman-active[216]. This vibration corresponds to the G-line situated at 1584 cm^{-1} in all spectra. The appearance of the other lines is due to one-phonon forbidden scattering and/or two-phonon resonant scattering[217]. Their position depends on the excitation photon energy, whereas their intensity depends on the excitation photon energy and/or defects in the layer and the finite size of graphene flakes. The frequency dependence of the D and 2D lines was reported[217], [218] and our spectra fully confirms it. The most prominent feature in the Raman spectrum of graphene is the 2D peak, whose position, shape and intensity are frequently used to distinguish between single-layer, bi-layer and multi-layer graphene. Taking into account the ratio between the 2D and G peak intensities and the full width at half maximum of the 2D-band ($\sim 49\text{ cm}^{-1}$) the obtained results show that the samples contain graphene sheets with single or few mono-layers of carbon atoms[219].

Furthermore, XPS and NEXAFS analysis have been performed to determine the elemental composition of the samples and to identify the chemical bonds. The representative XPS spectrum in Fig. 7(a) shows a relatively small amount of oxygen in respect to the prominent carbon presence. The C 1s region and the corresponding energy loss features are shown in Fig. 7(b). The line was fitted to the superposition of four peaks: the first three peaks can be attributed to sp^2 (284.4 eV), sp^3 (285.2 eV) and C-O-C or C-OH (286.3 eV) bonds[220], while the wide fourth peak represents π - π^* shake up satellite (290.6 eV). Analysis of O 1s line fully support these findings, with the peak being well reproduced as the sum of aliphatic C-O-C bond (532.4 eV)[220] and PbO (529.3 eV)[221] contributions after taking into consideration different C 1s positions assumed for adventitious carbon (Fig. 7(c)). The later contribution originates from the oxidized lead surface, used to hold the graphene powder.

The combination of UV irradiation and modest heating of the reactor's wall by IR irradiation at the post discharge region 15-30 cm from the launcher (i.e. $T_{\text{wall}}=150\text{ }^\circ\text{C}$) significantly increases

sp^2/sp^3 peaks area ratio to about 15, while in the absence of both, annealing and UV irradiation, the same ratio is 10. This is probably due to the breaking of sp^3 bonds by UV photons with an energy of about 3 eV (300–400 nm). The change in the amount of oxygen is, however, negligible (from 2.3 % to 2.2 %). At higher precursor fluxes ($Q_{Eth}=35$ sccm) and annealing temperature (260 °C), keeping the other operational parameters constant ($P=2$ KW; $Q_{Ar}=1200$ sccm, UV irradiation applied), the relative amount of oxygen is two times smaller (~ 1.1 %), while the sp^2/sp^3 peaks area ratio (15) is preserved. Under these conditions, defects are activated and annealed out by reopening the bonds and letting them reorganize to the perfect “crystalline” structure. This can be achieved only for a limited range of temperatures. Thus, the control/tuning of the thermodynamic conditions in the third (gas phase) zone of the reactor.

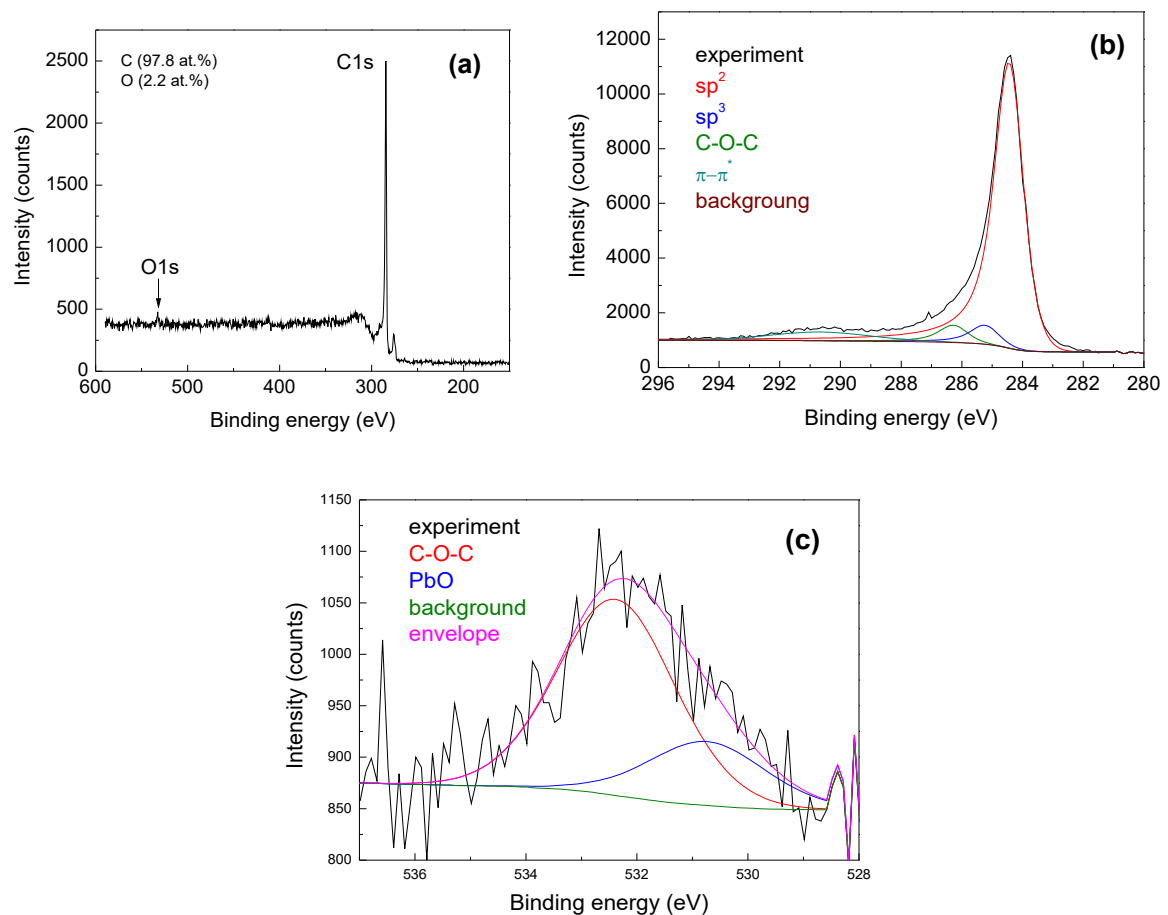


Figure II.15 - (a) XPS survey spectra of the sample obtained at $P= 2$ KW; $Q_{Ar}=1200$ sccm; $Q_{Eth}=26$ sccm; $T_{wall}=150$ °C, UV radiation applied; (b) detailed C 1s region with corresponding fitting; (c) detailed O 1s region with corresponding fitting.

The nature of chemical intra molecular bonding has been further analysed also by means of NEXAFS spectroscopy. Graphene powder was mechanically smeared onto different substrates. The substrates used for this specific measurement were intrinsic Si wafers. Spectra, as presented in Figure II.16, were obtained on the C K-edge, in the partial electron yield mode (PEY), which shows the very surface of the substrate[202].

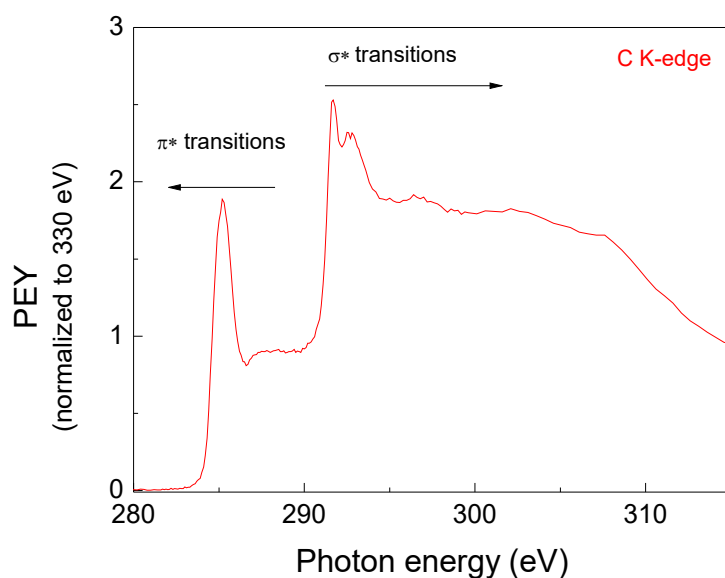


Figure II.16 - NEXAFS spectrum at C K edge of the graphene sheets synthesized at $P = 2 \text{ kW}$, $Q_{Ar} = 1200 \text{ sccm}$ and $Q_{Eth} = 30 \text{ sccm}$ and applied IR radiation ($T_{wall} = 240^\circ\text{C}$). Normalized to the absorption jump, with post-edge intensity at 330.0 eV is set at 1 [222].

A characteristic sharp C 1s $\rightarrow \pi^*$ resonance is observable at $\sim 285.1 \text{ eV}$ [223], [224]. σ^* resonances are observed at around 292 eV, with a sharp excitonic peak at $\sim 291.7 \text{ eV}$, where π^* and σ^* refer to anti-bonding molecular orbitals, i.e. bands, of π and σ symmetry, respectively[223], [224]. Higher energy features are due to transitions towards higher-lying states of π or σ symmetry[225]. The lack of other peaks in-between is an indication of absence or low levels of oxygen and hydrogen. These results are in accordance with the previous XPS analysis, that shows about 2 at.% of oxygen present on synthesized free-standing graphene sheets.

Processing graphene sheets is a delicate task since the charged sheets can reply in an ambiguous way during their treatment. Two photos of graphene sheets suspended on a glass substrate are shown in Figure II.17(a,b). The black graphene powder freely suspended on the glass substrate is shown in Figure II.17(a), while the same powder after being spread over the glass using a

metallic scalpel is shown in Figure II.17(b). As a result of this mechanical treatment, the graphene exhibits a yellow/golden colour.

The corresponding Raman spectra are shown in Figure II.17 (c). The spreading of graphene powder results in a sharp increase of the D-line at 1333 cm^{-1} and slight decrease of the G and 2D peaks. Moreover, a small frequency shift of the D-line of about 2 cm^{-1} towards smaller wavenumbers along with widening of the line is observed. The enhancement of the D-line, both absolute and relative to the G and 2D lines, may be simply related to the cutting-up of graphene sheets.

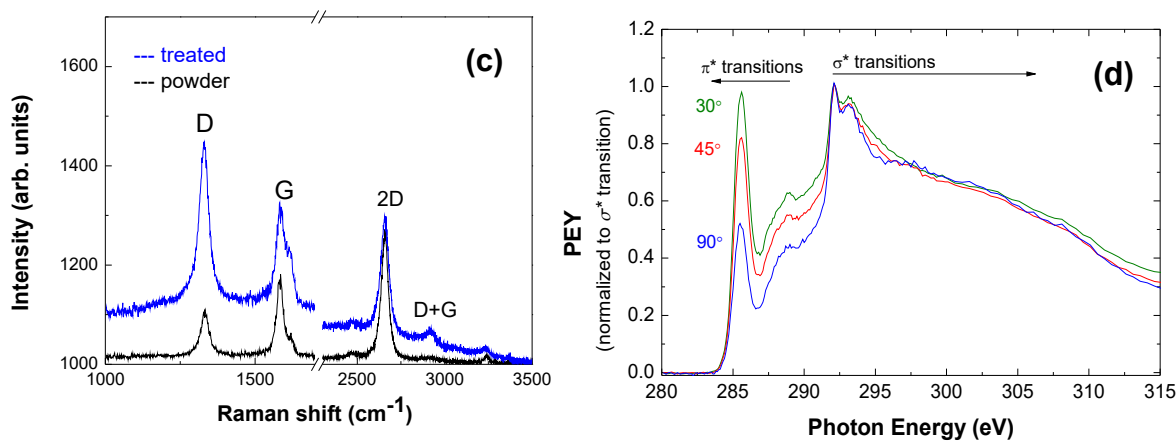


Figure II.17 - (a) Graphene sheets freely suspended on a glass substrate; (b) the same sheets spread over the glass with a metallic scalpel; (c) Raman spectra of the samples; (d) NEXAFS spectra of the graphene sheets spread over silicon substrate. Normalized to σ^* resonance peak at $\sim 291.7\text{ eV}$, indicated to observe angle dependence.

However, the process may also force the parallel orientation of the sheets in respect to the supporting dielectric surface and lead to the formation of a network of electrically-oriented

connected graphene sheets. In this case, the reduced G and 2D peak intensity could be linked to an increase in the conductivity of the whole layer and a corresponding decrease of the scattering volume. To test this hypothesis, traces of graphene powder were mechanically smeared over silicon substrate (simple Si wafer as used for microelectronics) and analysed by means of NEXAFS spectroscopy. Measurements were performed at different beam incident angles (θ_i) relative to the substrate surface as shown in Figure II.17.

At the low-energy side a sharp resonance at ~ 285.1 eV, corresponding to a C 1s - π^* transition[203], [223], [224], is observed, and second dominant feature, the double-structured resonance, is observed at around 292 eV, corresponding to C 1s - σ^* . This double resonance comes from excitonic (~ 291.7 eV) and band-like contributions (~ 293.1 eV)[222], [223]. Considering the “fingerprint” region between 286 and 290 eV it is possible to identify some residual peaks. In some studies, the origin of such peaks (specially broad shoulder) is connected with interlayer states in low symmetry regions of the Brillouin zone, as suggested by Fischer et al.[223] (based on band calculations), from defects in the top most graphene layers[226] or O-containing functional groups, resulting from oxidation (as it is most probably in this case).

NEXAFS is a powerful tool to observe molecular orientations due to the high linearly polarized nature of the synchrotron radiation, specifically for 1s \rightarrow 2p excitations, where the product of the orbital symmetry axis and the electric dipole leads to simple intensity correlations between incidence angle and molecular orientation of the radiation[203], [223], [227]. There is a clear angular dependence of the C1s \rightarrow π^* resonance peak at 285.2 eV, with its intensity increasing towards the plateau regions and towards the intensity of excitons, as the incident angle relative to the supporting surface decreases. The differences are strongly correlated with orientation of the bonds relative to the surface and therefore support the existence of self-organization of the graphene sheets with respect to the surface of the substrate. In graphene sheets, the π bond deriving from p_z orbitals is oriented perpendicular to graphene plane (out-of-plane) and the σ bond is oriented along the intermolecular bonding axes (in-plane). Thus, as the angle between incident beam and surface increases out-of-plane excitation, i.e., π^* resonance becomes weaker, and the ratio between σ^* and π^* resonances at 291.7 eV and 285.1 eV increases, as it is expected for highly oriented structures[224] with a preferential orientation of the graphene sheets parallel

to the substrate. It is to be noted that this alignment does not disappear over time or after functionalization by means of for example ammonia or nitrogen plasma.

To measure the electrical conductivity of the graphene sheets, 0.1 g of the graphene powder was pressed into a disc of 8 mm diameter and 1.2 mm thickness. The electrical conductivity was measured applying Van der Pauw method at room temperature[228]. The measurement geometry utilizes a four-contact scheme where pinching point contacts are used, situated on the periphery of the tablet. This design provides measurement of the longitudinal conductivity as far as the current lines are parallel to the tablet surface. The current during the measurement was in the range 1–2 mA. Additionally, current-voltage characteristics and reconfirmation of the Ohmic contact character were conducted for current values ranging from 0.5 to 3.5 mA. Several measurements were carried out and the average value is reported. The electrical conductivity of the graphene sheet measured was (3500 ± 350) S/m, which is much higher than the reported values of graphene sheets powder obtained by chemical methods[229] and comparable with a reported value[230]. This could be explained with highly conductive sheets having multiple interfaces between them.

II.1.1.4.3. In-situ synthesis of N-graphene

In order to test the direct route for N-graphene synthesis as well as to demonstrate potential of the method, nitrogen gas flow (5–10 sccm) has been added to the ethanol flow. A small percentage of the N_2 in respect to the background argon flow results in a high dissociation degree of N_2 molecules, therefore, generating a significant amount of reactive nitrogen atoms, approximately 10^{22} m^{-3} (value estimated using the model present in [231]), that can be incorporated into the growing carbon lattice structure. Nevertheless, the dependence of N atoms density on gas mixture composition is to be noticed[211]. The rate of pure N-graphene sheets collected at a background argon flow of 1200 sccm, power of 2 kW, precursor (ethanol) flow of 15 sccm at 40 °C and N_2 flow of 5 sccm was about 0.5 mg/min. In the next Figure II.18(a), a SEM image of disordered N-graphene sheets is shown, revealing only graphene-like sheets. Hence, it may prove that this plasma method is a non-destructive path to obtain N-doped graphene, since its morphology did not change when compared with the one of pure graphene sheets (Figure II.12). Given the fact that N atoms incorporate the carbon lattice in different carbon-nitride configurations, it is

conceivable that uneven distribution of charges in the different sheets promote the creation of attractive forces that increase their interactions.

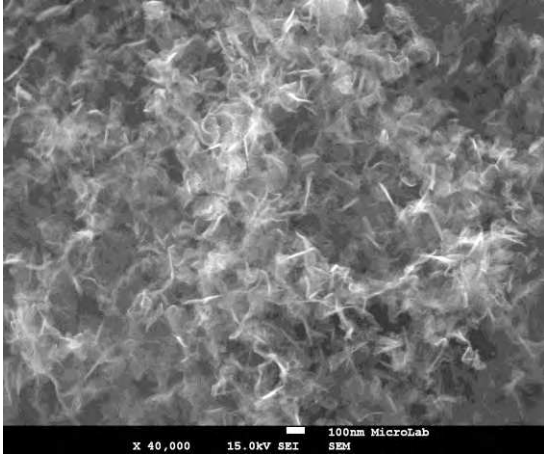


Figure II.18 – (a) SEM image of N-graphene sheets and (b) Raman spectra obtained at different partial N_2 flows. Plasma conditions: $Q_{Ar} = 1200$ sccm; $Q_{Eth} = 15$ sccm, $Q_{N_2} = 5$ sccm.

Furthermore, Figure II.18(a) shows the obtained Raman spectra for “pure” graphene sheets and its evolution with the increasing of N_2 flow. Laser emitting at 633 nm has been used. As discussed, the three typical graphene peaks are attributed to the G band at ~ 1583 cm^{-1} , 2D band at ~ 2658 cm^{-1} , and D band at about ~ 1332 cm^{-1} . The D band, i.e., “disorder” band, is related to a series of defects: bond-angle and bond-length disorder as well as hybridization that are caused by hetero atoms, i.e., nitrogen doping. The presented spectra are averaged over different locations. The most notable spectral change is the increase in the D band to G-band intensity ratio when N_2 is introduced in the plasma. As seen from the figure, the D-peak intensity rises with the introduction of N_2 gas. The nitrogen atoms constitute defects within the graphene lattice and consequently contribute to the D band intensity, yielding the observed increase of the D band to G-band intensity ratio.

Similarly, N-graphene sample chemical structures can be seen from XPS regions of C 1s and N 1s in Figure II.19(a,b). The main peak fitted in C 1s region is centred at 284.3 ± 0.1 eV which is assigned to sp^2 carbon atoms bound to carbon or hydrogen atoms.[23], [107], [212] Peaks centred at higher BE are assigned to sp^3 carbon atoms bound to other carbons or hydrogen atoms (285.0 eV), carbon bound to nitrogen or singly bound to oxygen (peaks at 285.7 and 286.6 eV), carbon in epoxide and/or carbonyl groups (287.6 eV) and carbon in carboxylate groups (289.0 eV)[220]. The spectral features detected at BE >290 eV are energy losses due to π - π^* excitations

typical of carbonaceous systems with delocalized π electrons such as graphene. The peak centred at 289 eV may be overlapping some of these features. Peaks found around 286 eV, which are, in a first approach, identified as C-N and C-O, are most probably superposing some aliphatic carbon atoms (C) bound to other carbons (C-C<) from more electronegative vicinities, for instance C-COO- or C-(C = O) (which can be found, roughly, between 285.3 and 286.2 eV) [220]. XPS confirms undoubtedly the doping of graphene by nitrogen atoms. The N 1s region was fitted with two peaks, one centred at a binding energy equal to 399.4 ± 0.2 eV assigned mainly to pyridinic nitrogen[107], [220], and a minor peak centred at 401.2 ± 0.2 eV, corresponding to graphitic nitrogen[107], [232]. Pyrrolic nitrogen, which is likely to exist in these structures, must be close to 399.9 eV[107], [233], i.e. between the two fitted components. The shoulder found around 398.6 eV (not fitted) can be attributed also to pyridinic nitrogen in a slightly different chemical environment than the N 1s main peak (for instance in a more electron delocalized vicinity[234]). The quantitative analysis shows that the relative atomic concentration of nitrogen incorporated in the graphene scaffold is 0.2 at.% for the conditions considered. The relative atomic concentration of incorporated oxygen is 8 at.%.

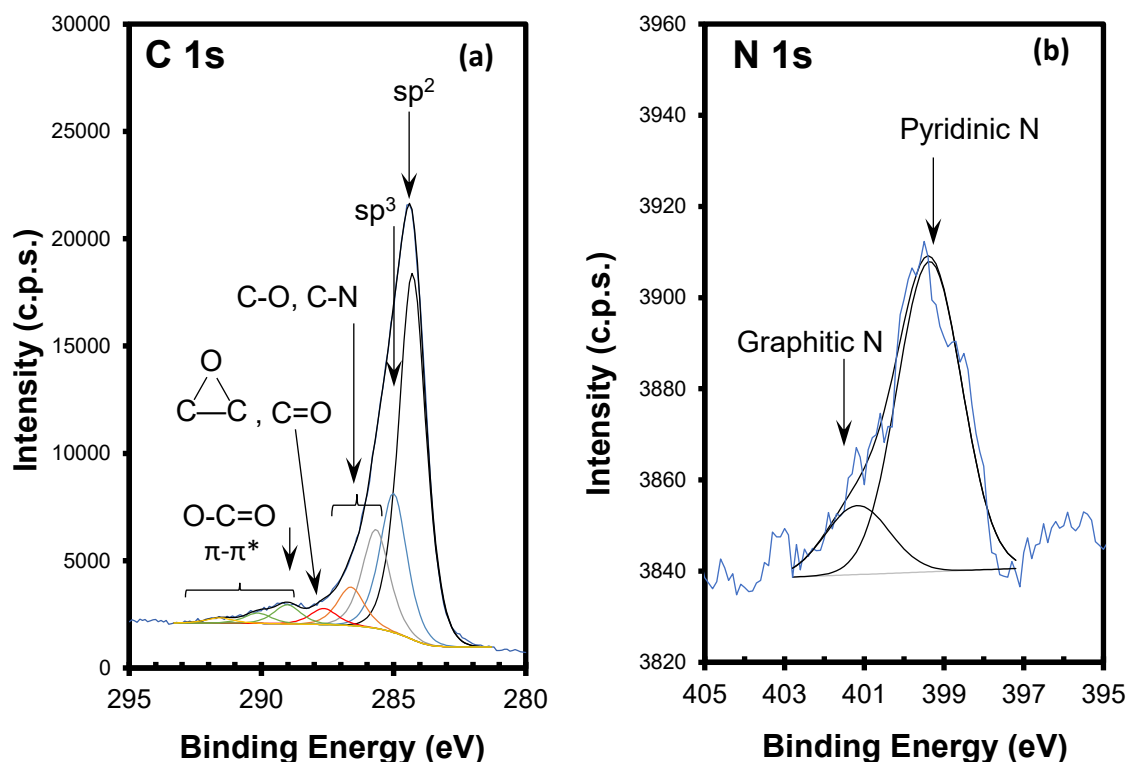


Figure II.19 – (a) Detailed C1s and (b) N 1s regions with corresponding fitting. ($P = 2$ kW, $Q_{Ar} = 1200$ sccm, $Q_{Eth} = 15$ sccm, $Q_{N_2} = 5$ sccm).

FTIR analysis was additionally employed to investigate the chemical bonding differences when graphene sheets are N doped (see Figure II.20)[235]. The FTIR spectrum of graphene sample is characterized by a broad peak at around 1100 cm^{-1} – 1220 cm^{-1} , which can be attributed to C–O and C–O–C stretching bands, respectively, being in agreement with XPS results (see Figure II.19(b))[236], [237]. In the IR spectrum of N-doped graphene (see Figure II.20) some of the above peaks are not present, while several new bands appear. Few weak and broad peaks at 1220 , 1340 (shoulder of a higher peak at 1390 cm^{-1}), and 1550 cm^{-1} in the spectrum of N-graphene, can be attributed to C–O–C/C–OH stretching, C–N stretching and N–H bend vibrations, respectively[236], [237]. Additionally, the most intense peak at 1390 cm^{-1} (C–O–H stretching vibrations) is detected along with a wider band at around 3000 cm^{-1} (C–H)[238]–[241].

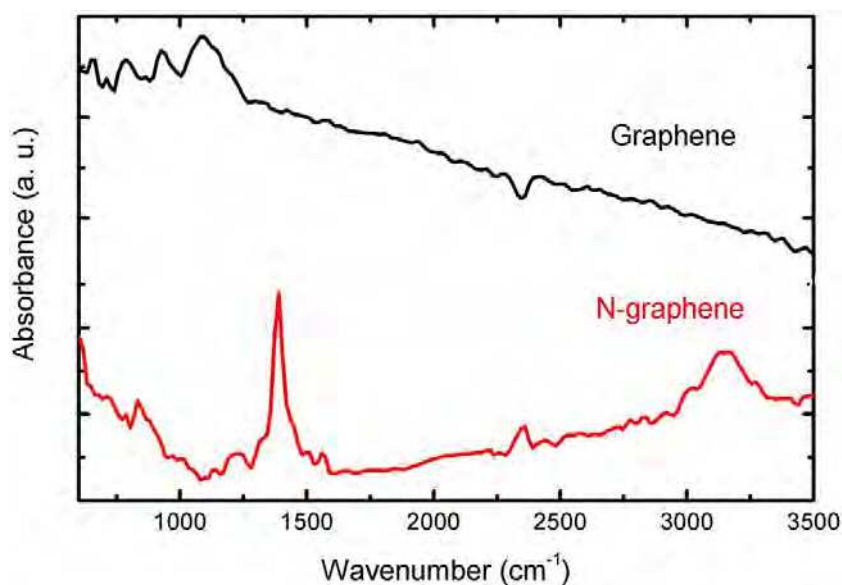


Figure II.20 - FTIR spectra of graphene and N-graphene ($P = 2\text{ kW}$, $Q_{Ar} = 1200\text{ sccm}$, $Q_{Eth} = 15\text{ sccm}$, $Q_{N_2} = 5\text{ sccm}$).

II.1.1.5. Summary

In summary, microwave-driven plasmas were successfully applied for the first time in the selective synthesis of high-quality graphene and N-graphene sheets via a single step process at atmospheric pressure. A high level of control over oxygen functionalities and sp^2/sp^3 carbons ratio (~ 15) has been achieved. For a randomly chosen samples, the percentage of counts of monolayers in all graphene sheets is about 40%. The method is rapid, highly cost-efficient and environmentally friendly, since it does not require the use of catalysts and noxious chemicals. It is also

customizable and versatile, allowing the synthesis of different types of 2D nanostructures (e.g. N-graphene,) in the same reactor. Furthermore, the high energy density of the generated plasma environment allows the use of gaseous and liquid precursors. Moreover, self-organisation of the graphene sheets in respect to the supporting surface after mechanical treatment was observed. To this end, our key enabling technology provides a rapid, single-step, cost-efficient and environmentally friendly method for selective synthesis of tailored graphene/N-graphene sheets at high yield and at atmospheric ambient. It is non-destructive, free of toxic chemicals, metal catalysts and substrates, and allows the use of carbon precursors in solid, liquid or gas state. The main advantage of our approach is the achievement of a very high and extremely controllable energy density in the plasma reactor, which allows effective control over the energy and material fluxes towards growing nanostructures at the atomic level via proper reactor design and tailoring of the plasma environment in a synergistic way. The ability to control the amount and localization of energy and matter delivered from the plasma bulk to the developing nanostructures is the key to achieve the desired morphological, structural and functional properties of targeted materials.

Further scale-up along with better understanding of nucleation/growth processes in a multiphase environment will certainly lead to a substantial increase of the yield and a reduction of the production costs. Besides, mastering will be focused on reducing the multilayer (5-10 single layers) sheets percentage below 1%, controllable increasing of N-doping and optimization of collecting system for extraction of nanoparticles with dimensions less than 20 nm, i.e. graphene quantum dots. The use of large-scale configurations of wave-driven discharges paves the way for further scale-up and a higher level of customization. The exclusive plasma mechanisms that rule the distributions of energy and matter at atomic scale endow the method significant potential for the synthesis of other 2D materials (e.g. boron-doped graphene, hBN, etc). The method has also a potential for producing unique graphene-metal nanocomposites with well-designed nanoarchitecture.

Some studies have already started concerning investigation of other carbon-nitrogen-containing precursors, such as pyridine and methylamine, for direct synthesis of N-graphene, revealing very promising results, namely higher doping levels when using methylamine as precursor, approximately 5.4 at.%.

II.1.2. Synthesis of complex carbon structures using different precursors

To the best of our knowledge, only a couple of examples in the literature, using plasmas at atmospheric pressure conditions, focus on the production of either isolated free-standing graphene sheets and/or nanodiamonds [4], [5], [23], [88], [191], [242]

The work presented in this section extends the scope of previous efforts in this field by using different carbon precursors (methane, carbon dioxide mixed with hydrogen) to produce free-standing carbon nanostructures via microwave plasmas driven by surface waves at atmospheric pressure conditions, using what is essentially the same set up (Figure II.1). The externally controlled operational parameters and, consequently, the plasma properties have been adapted to achieve selective synthesis of free-standing carbon nanostructures and to induce different level of crystallization in the final product. The synthesized nanostructures were analysed by applying SEM and Raman spectroscopy. In order to identify the species involved in the nucleation processes, OES measurements in 250-750 nm spectral range were performed. A self-consistent kinetic model has been developed to describe the methane decomposition and the theoretical data have been validated by the experimental ones. Part of the results presented in this section were published in [93], [191].

II.1.2.1. Experimental proceedings

II.1.2.2. Basic Workings

Given the fact that the nucleation and growth processes are determined by the interplay of kinetic and thermodynamic factors, the engineering of structural qualities of targeted nanostructures was achieved via synergistic tailoring of the “hot” plasma environment and thermodynamic conditions in the “mild” zone of the plasma reactor (see Figure II.21).

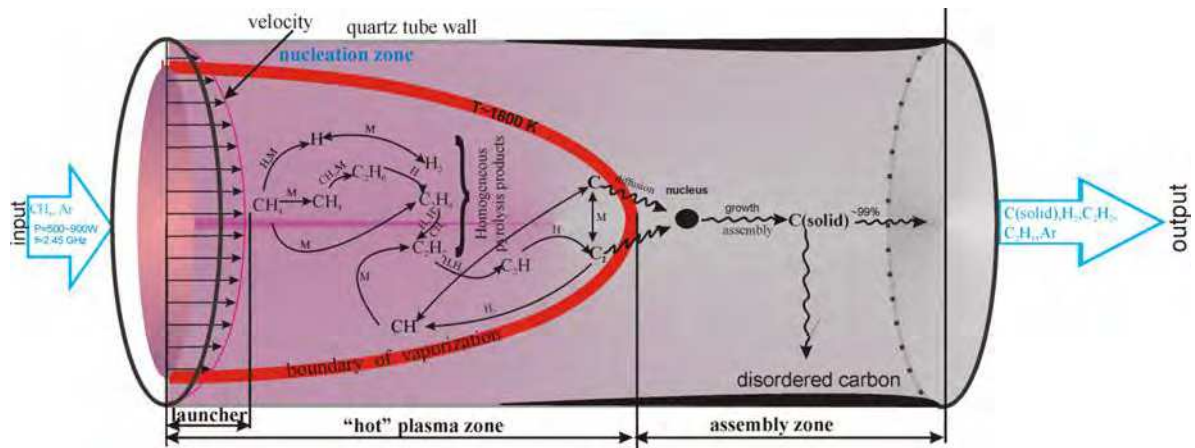


Figure II.21 - Schematic of methane dissociation inside the discharge. [191]

The "active" microwave plasma region of the reactor considered is composed by two zones. The first one is the surface wave sustained discharge zone, including the zone inside the launcher and the extended "hot" plasma zone outside the launcher. Here, the surface wave power is absorbed by plasma electrons, which transfer the power to heavy particles via elastic and inelastic collisions, resulting in high gas temperatures. The gas temperature maintains nearly constant in the discharge zone when moving away from the launcher (up to about 10 cm) and then drops sharply in the "near" (10 - 13 cm) afterglow plasma zone. The next zone in axial direction that includes the plasma afterglow (~ 20 cm) is the "assembly zone" (see Figure II.21) where kinetic processes of growth and assembly of carbon nanostructures take place.

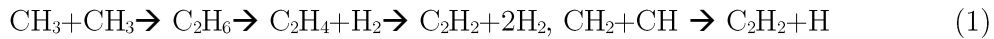
The model used to describe the methane decomposition is based on a self-consistent treatment of plasma thermodynamics and chemical kinetics and is similar to the one developed by N. Bundaleska et al.[243]. The model input parameters are externally controlled, i.e., gas flows, total power delivered to the launcher, pressure and background gas mixture composition, i.e., the Ar/CH₄ gas mixture injected into the discharge. A kinetic scheme similar to that presented in [243] is used. The scheme includes 57 components and about 390 chemical reactions. The model was applied for the heterogeneous case, i.e. considering that both gas and solid phase carbon nuclei are formed in the plasma. The thermodynamic information of the considered processes was obtained from thermodynamic databases [244]–[247]. The rate balance equations for the decomposition products were solved simultaneously with the gas thermal balance equation, i.e.,

$$\frac{p_0 V_0}{k_B T_0} c_p \frac{dT_a}{dz} = -\frac{4\chi(T)}{R^2} (T_a - T_w) + \frac{\delta P}{S dz} \quad (\text{eq. II-1})$$

where p_0 corresponds to the gas pressure, k_B is the Boltzmann's constant, V_0 is the gas velocity, T_0 is the initial gas temperature, c_p is the heat capacity at constant pressure, T_a is the temperature at the discharge's axis, χ is the Ar thermal conductivity, R is the tube radius, T_w is the wall temperature, δ is the fraction of the absorbed wave power which is transferred to thermal energy of the gas, S is the plasma cross-section and P is the absorbed microwave power. The microwave power dissipation was assumed linear along the plasma column length and δ was estimated to be 0.9, a typical value for discharges at atmospheric pressure.

The calculated relative concentrations of the main products, which result from the decomposition process of methane in the Ar plasma, are shown in Figure II.22 (b) as a function of the distance from the launcher. The theoretical results for the axial variation of the gas temperature are presented in Figure II.22 (a). A theoretical model previously developed has been further updated and refined to map the thermal fluxes in the plasma reactor[191], [243]. The reference point, $z=0$ cm, corresponds to launcher position.

Methane dissociation begins in "hot" plasma zone. The major initial reaction is C-H bond breaking with simultaneous formation of CH_3 , CH_2 , CH , H , C_2 and C at "hot" plasma zone (Figure II.22(c)). These radicals are involved in the formation of ethane and ethylene. The recombination of radicals can lead to the formation of acetylene through the following reactions:



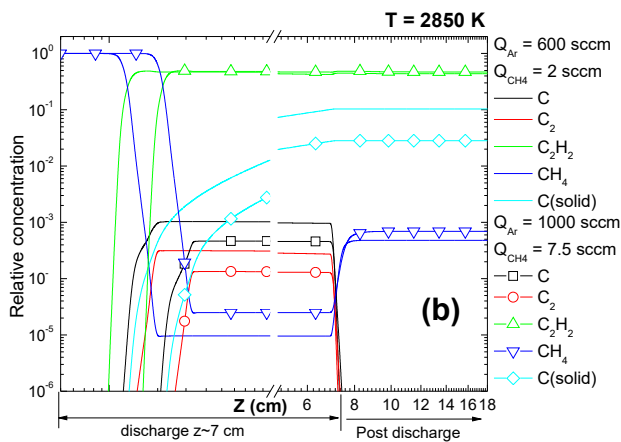
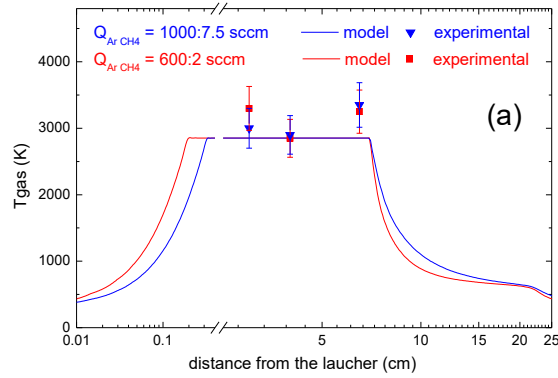


Figure II.22 - (a) Gas temperature profile, where samples were produced at $P=1$ kW, $p=1$ atm, and at two different Ar-CH₄ mixtures: 1000-7.5 sccm and 600-2 sccm). (b, c) Axial distribution for the main CH₄ decomposition products in the discharge and afterglow plasma jet. ($P = 1$ kW, $p = 1$ atm, $T_{gas}=2850$ K). [191]

Outside of the launcher the gas temperature is almost constant, approximately 2900 K, along the discharge zone but sharply decreases in the afterglow region and approaches room temperature in the outlet gas stream. Since the CH₄ decomposition process is thermally dependent, the resulting stable species concentrations reveal evident axial variations. The main zone, where nucleation occurs, is located near the tube walls. In the Figure II.22 (b, c) this is the zone outside of the vaporization boundary surface. The main outlet products of methane decomposition are H₂, solid carbon, C₂H₂ and C₂H₄ and CH₄. A fraction of the solid carbon nuclei accumulates on the wall, but the majority of it is gradually removed with the outlet gas stream in the assembly zone as seen in Figure II.22 (b, c). A decrease of both C and C₂ species were

observed with the increase of the background gas flow and hydrogen content in the gas mixture Figure II.22 (b).

II.1.2.3. Tailoring plasma environment

A plasma emission spectrum in the 300-800 nm range detected at an axial distance of 3 cm is shown in Figure II.23 (a). As it can be seen in the figure the spectrum is dominated by argon atomic lines. The vibrational sequences belonging to C₂ Swan band are as well presented in the 400-600 nm spectral range as expected from the previous analysis.

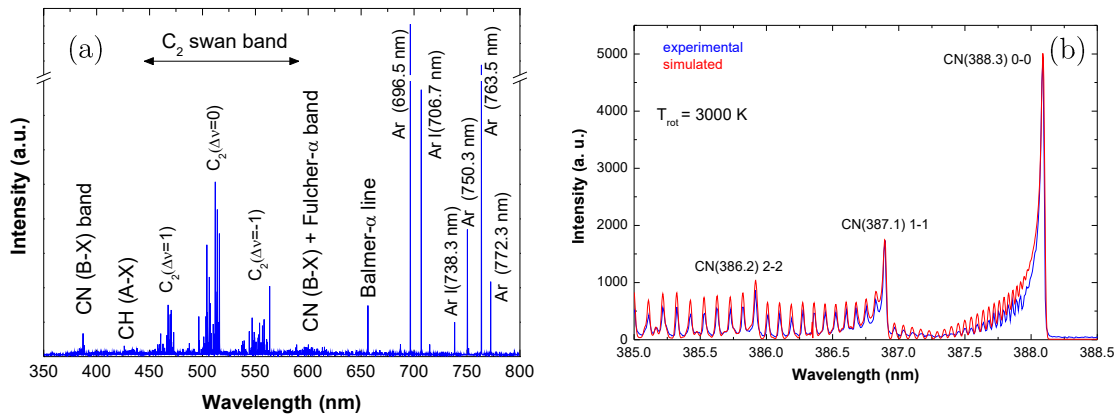


Figure II.23 – (a) Plasma emission spectrum in the 300-800 nm range and (b) CN(B²Σ⁺ → X²Σ⁺) emission band at P= 1 kW, p=1 atm, Q_{Ar}=600 sccm Q_{CH₄}=2 sccm mixture, at 3 cm from the launcher.

The typical C₂ emission is generated by the radiative decay of the C₂^{*}(A³Π_g) state. As it was seen in the previous section (II.1.1 - Microwave plasma-based method used for 2D and 3D carbon nanostructures synthesis), the bands appear due to excitation of ground state C₂ molecules to higher levels either by electron impact, or by three body recombination processes involving C and Ar atoms, or by recombination of two carbon atoms at the quartz tube wall. Reactions of C₂ molecules with hydrogen and oxygen radicals result in C₂ dissociation and formation of atomic carbon.

In this case, the emission band from CN species, corresponding to violet CN(B²Σ⁺ → X²Σ⁺) transitions, was also used to estimate the rotational temperature Figure II.23 (b). Assuming local thermodynamic equilibrium between rotational and translational degrees of freedom an estimation of the gas temperature was obtained from measurements of the rotational CN(B²Σ⁺ → X²Σ⁺) (3800-3883 Å) spectra. The rotational temperature measured at 3 cm from

the launcher was approximately 2900 K and remains almost the same from 3 to 6.5 cm away from the launcher, nearly at the middle of the “hot” plasma zone.

The good agreement between the theoretical and experimental values of the gas temperature shown in the Figure II.22(a) is to be noted. Since the radiation collected originated mainly from the central axial part of the “hot” plasma column, the results correspond to that same region of the plasma.

Due to the presence of hydrogen in the precursor it is possible to analyse the emission of Balmer beta line (H_{β}) and information concerning electron plasma density can be obtained. The H_{β} line was measured at several positions along the discharge axis. For each position along the discharge axis the experimental profile was fitted with a Voigt function, which is a convolution of Gaussian and Lorentz profiles. The instrumental broadening caused by the spectrometer was estimated to be 0.065 Å. The electron density (estimated on the basis of the Lorentzian component width) varies within the limits $7-9 \times 10^{13} \text{ cm}^{-3}$ in the "hot" plasma zone.

As mentioned previously the plasma reactor wall temperature is one of the key parameters influencing the process of synthesis of high-quality graphene sheets. To this end, infrared sensitive measurements of the wall temperature were also performed on this reactor. The 2D thermal image of the plasma as detected by thermal FLIR camera is shown in Figure II.24(a). The corresponding variation of the wall temperature along the tube axis are shown in Figure II.24(b). As seen, the wall temperature increases reaching a maximum at the middle of the "hot" zone, around 5 cm from the launcher, and then decreases with the distance, reaching room temperature at nearly 25 cm (Figure II.24(b,c)).

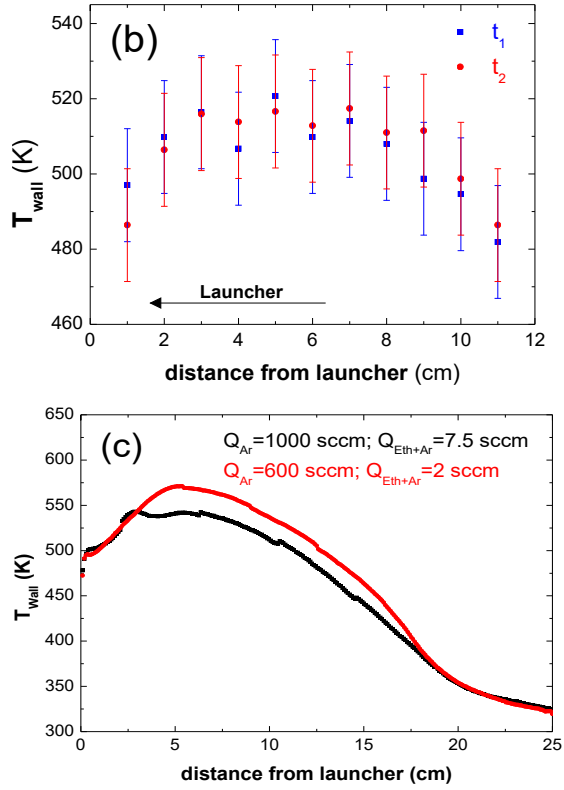


Figure II.24 - (a) Thermal image of the discharge at $P=1$ kW, $p=1$ atm, $Q_{\text{Ar}}=600$ sccm, $Q_{\text{CH}_4}=2$ sccm. and respective (b) axial wall temperature profile along the discharge tube captured at two different times. (c) Axial wall temperature profile along the discharge tube captured at 2 different gas mixtures.

An increase in gas flow from 600 to 1000 sccm leads to an evenier heat distribution along the discharge for the same amount of applied microwave power (1 kW) and results in an decrease of the wall (and gas) temperature in the “hot” plasma zone from 570 K to about 530 K, at $z = 5$ cm (see Figure II.24(c)). These axial variations of the gas/wall temperature correspond to the synthesis of different types of carbon nanostructures as shown below.

Stark broadening of the Balmer-beta line was used to estimate the electron density of the plasma. To this end, the Balmer-beta line profile for different plasma conditions were fitted with a Voigt profile (see an example in the inset graphic in Figure II.25).

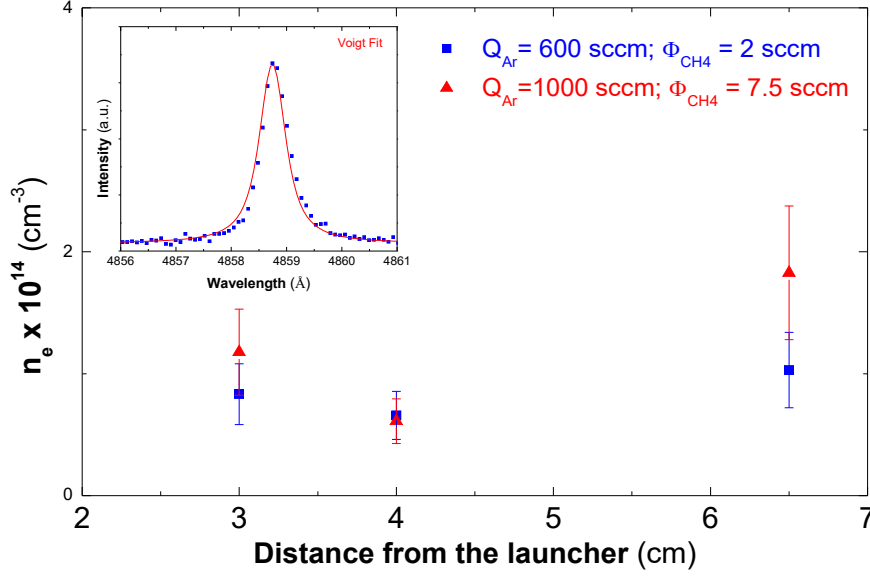


Figure II.25 – Axial variation of the electron density. (inset) Emission profile of Balmer-beta line ($Q_{Ar} = 1000 \text{ sccm}$, $Q_{CH_4} = 7.5 \text{ sccm}$, $P = 1 \text{ kW}$, $z = 3 \text{ cm}$) Material characterization

The Voigt profile is a convolution of two profiles, Gaussian and Lorentzian, being the first one a conjugation of Doppler and instrumental broadening, whether the second broadening corresponds to pressure and Stark broadening mainly. Therefore, in order to determine the full width at half-maximum of the Gaussian and Lorentzian components a deconvolution of the H_{β} line was performed. Under conditions considered the major contribution to Lorentzian line broadening is the Stark broadening caused by Coulomb interactions between charged particles. The plasma electron density is then calculated, using the expression of the electron density obtained from a fit to the data listed by Gigosos and Cardenoso[248], [249]:

$$FWHM = 4.8 \text{ nm} \left(\frac{N_e}{10^{23} \text{ m}^{-3}} \right)^{0.68116} \quad (\text{eq. II-2})$$

Axial variations of the electron density are shown in Figure Figure II.25, the average electron density of the plasma is around 10^{14} cm^{-3} .

II.1.2.4. Material Characterization

II.1.2.4.1. Techniques

Raman spectroscopy and SEM techniques used have the same characteristics as described in the previous section (II.1.1 Mass production of high-quality free-standing graphene and N-graphene sheets using an Argon-Ethanol microwave plasma).

For the HRTEM analysis the synthesized carbon nanostructures were placed directly onto a holey grid of Titan ChemiStem (FEI) HRTEM operating at 300 kV accelerating voltage.

The X-ray diffraction was studied with a Panalytical X'Pert Pro MPD diffractometer, equipped with a curved graphite monochromator. Cu-K α radiation ($\lambda=1.5406 \text{ \AA}$) was used. The current and the accelerating voltages in the X-ray tube were 35 mA and 40 kV, respectively. The spectra were measured in a range of 2θ from 10° to 90° . For the diffraction patterns identification ICDD data base was used, version PDF-2. The Bragg's equation was applied to the observed reflection planes to evaluate the distance between graphene layers, denoted as d (Table II-2).

II.1.2.4.2. Results and analysis

A typical SEM image of the graphene sheets synthesized and captured by the filter membrane system [3], [4] is shown in Figure II.26(a). The intrinsic curled/wavy morphology of graphene, consisting of a thin wrinkled paper-like structure, is readily identifiable. This result is further confirmed by Raman spectroscopy measurements Figure II.26(b).

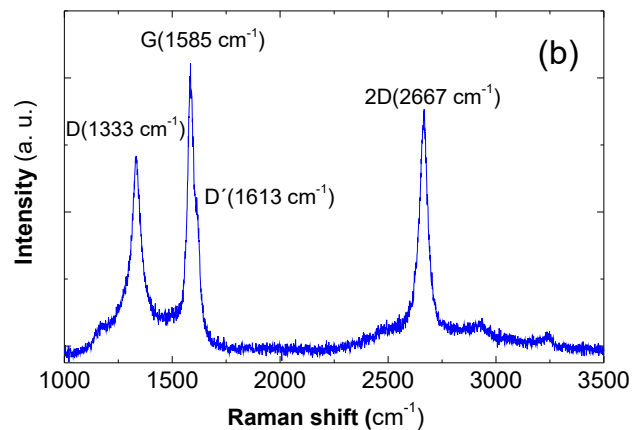


Figure II.26 – (a) SEM image and (b) respective Raman spectrum of synthesized material at $P= 1 \text{ kW}$, $p= 1 \text{ atm}$, $Q_{Ar}=600 \text{ sccm}$ and $Q_{CH_4}=2 \text{ sccm}$.

The spectrum presented correspond to an average of the collected spectra at different regions of the sample and reveals a G-band peak related with the tangential zone centre mode at 1585 cm^{-1} and a sharp two-dimensional (2D) peak at about 2667 cm^{-1} due to the second order process, providing that the obtained carbon nanosheets are indeed graphene sheets. D-peak appears at approximately 1333 cm^{-1} and the small shoulder of the G peak at around 1613 cm^{-1} , which can be related with structural disorders, presence of sp^3 carbon bonds in the created sheets and/or edge effects as mentioned previously. The 2D peak as one of the most prominent features in the Raman spectrum of graphene, whose position, shape and intensity are frequently used to distinguish between single-layer and multi-layer graphene is also observed but not as sharp as it was shown in the previous section (section II.1.1 - Mass production of high-quality free-standing graphene and N-graphene sheets using an Argon-Ethanol microwave plasma). Considering the ratio between the G and 2D-peak intensities ($I_G/I_{2D}\sim 1.3$), the ratio of the D-peak to the G-peak integral intensities is ~ 1.5 and the FWHM of the 2D-band ($\sim 46\text{ cm}^{-1}$), the obtained results indicate a synthesis of few-layer graphene sheets. At the conditions considered free-standing graphene sheets are the only carbon allotrope present in the obtained sample is to be noted.

The plasma/gas thermodynamics plays a key role in the processes of formation and growth of the nanostructures. The temperature profile in the assembly zone can strongly influence the final product structure. For example, a too long residence time in this zone may result in growth of the sp^2 planes, but graphene sheets can also agglomerate due to Van der Waals interactions and form graphite. Depending on the thermodynamic conditions different carbon allotropes can be formed. The consequences of an almost two-fold increase in gas flow can be seen in Figure II.27.

Figure II.27 – (a,b) Carbon nanostructures produced at $P=1$ kW; $p= 1$ atm, $Q_{Ar}=1000$ sccm and $Q_{CH_4}=2$ sccm.

Moreover, increasing the background flux leads to change of the thermal map in the “active chemical” and the “assembly” plasma zones (Figure II.24), therefore different carbon nanoparticles as well as diamond-like structures were produced along with graphene sheets. Free-standing graphene sheets (Figure II.27(a)), particle-like structures (Figure II.27(b)) were simultaneously synthesized at nearly double decrease of the residence time when compared with the free-standing sheets obtained at the same power but different gas mixture composition and fluxes correspondingly (see Figure II.26(a))

Afterwards, we increased the precursor flux to 7.5 sccm and external cooling in the “assembly” zone up to 0° C was applied to force the creation of supersaturation conditions as described in [4], to adjust the temperature spatial profile in the “assembly” zone. Considering the cryostat system positioned at post discharge region, the cooling fluid circulates, with a constant flow rate, between the cryostat and a tubular heat exchanger as shown in Figure II.1. The heat exchanger consists of an external pyrex tube, with internal and external radii of (31.8 ± 0.1) mm and (42.0 ± 0.1) mm, respectively, concentrically aligned with the outer discharge quartz tube, placed at the afterglow region. The wall of the quartz tube is the heat transfer surface. The liquid used in the cryostat varied from 0°C to 100°C.

Comparing SEM images of Figure II.27 and Figure II.28(a,b), it is possible to verify that particle-like structures are the predominantly synthesized structures, which is representative for the whole sample. However, still a very small amount of structures resembling graphene sheets were also

synthesized, but not as transparent as the ones present in Figure II.26, showing the possibility of multi-layered sheets.

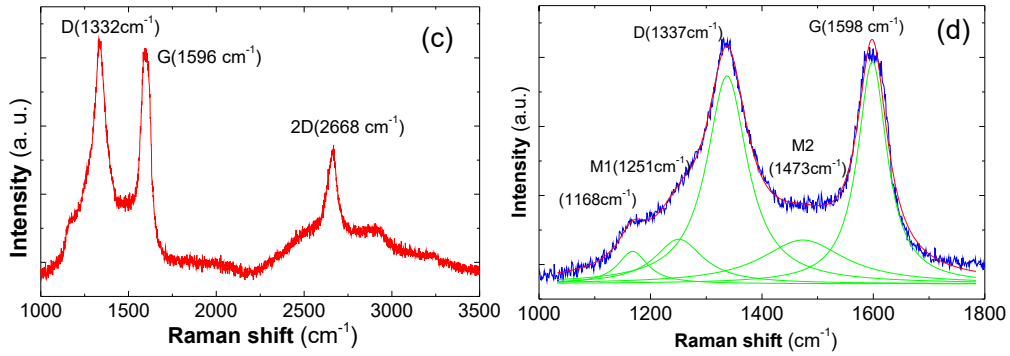


Figure II.28 – (a,b) Carbon nanostructures produced at $P=1$ kW; $p=1$ atm, $Q_{Ar}=1000$ sccm and $Q_{CH_4}=7.5$ sccm and $T_{Wall}=0^\circ C$. (c) Respective Raman spectrum. (d) Inset of Raman spectrum in the range 1000-1800 cm^{-1} and corresponding deconvolution.

The corresponding Raman spectrum can be seen in Figure II.28(c) and respective fitting in Figure II.28(d). Several significant changes in the spectrum occur when compared to the Raman spectrum of the graphene sheets present in Figure II.26, which were produced with almost half of background gas and one fourth of the precursor. The Raman spectrum also proved the observation in SEM images, a significant decrease of graphene related 2D peak (at ~ 2668 cm^{-1}) along with an increase of the D-peak (at ~ 1332 cm^{-1}) in respect to the intensity of the G peak. The position of the G peak is also shifted to 1596 cm^{-1} compared to 1585 cm^{-1} in graphene samples. Part of the Raman spectrum between 1000 and 1800 cm^{-1} is displayed in Figure II.28(d). The complex shape of the Raman intensity can be fitted with 5 Lorentzian profiles. The deconvolution resulted in 5 contributions at frequencies 1168, 1251, 1337, 1473 and 1598 cm^{-1} . It is seen that except the dominating D and G bands, observed in all sp^2 containing carbon materials, the weak

so-called M1 (1168) and M2 (1473) bands are observed [250]. These two bands always are observed in the spectra of nanocrystalline diamond. Although it is uncertain if they are really intrinsic for the nanocrystalline diamonds or rather they originate from a satellite co-phase (trans-polyacetylene), their observation in our spectra is a good indication of the presence of such structures in the sample. For higher partial methane fluxes and lower temperatures in the assembly zone (7.5 sccm) carbon nanoparticles with a size ranging from 70 to 800 nm are produced. The particle size distribution is shown in Figure II.29. As expected, the density of carbon species increases as the partial flux increases, and, as a result, the conditions in the assembly zone favoured creation of spherical particle-like nanostructures.

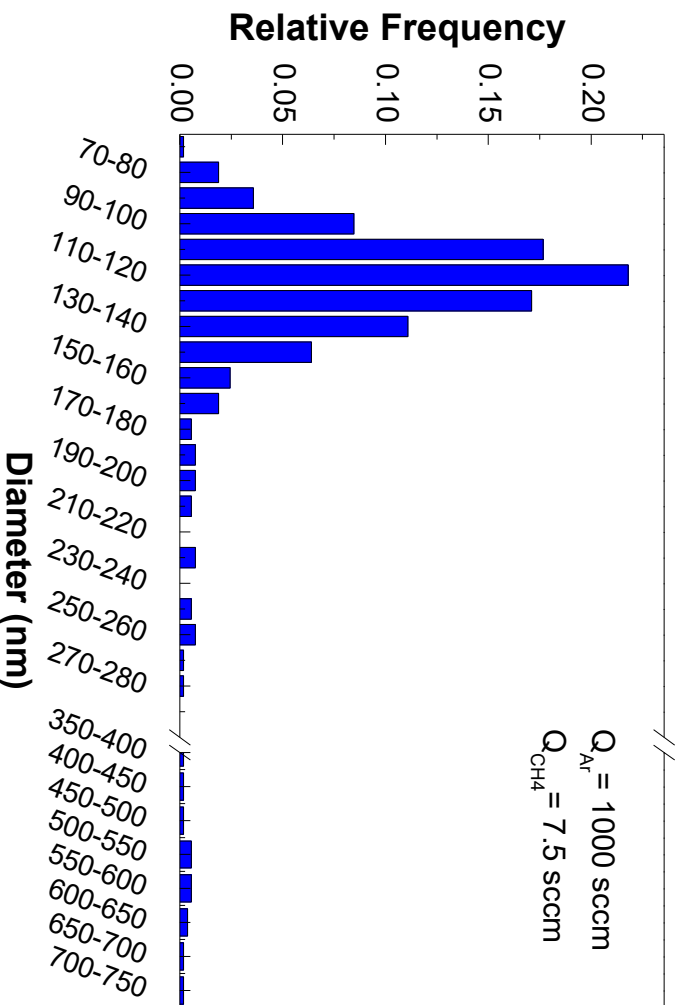


Figure II.29 – Particle size distribution Carbon nanostructures produced at $P=1$ kW; $p=1$ atm, $Q_{Ar}=1000$ sccm and $Q_{CH_4}=7.5$ sccm and $T_{wall}=0^\circ C$.

Additionally, there is interplay between the density of nucleation centres and the mean free path (λ_{c-c}) for carbon-carbon atomic collisions. Once being introduced in a volume already containing nucleation centres, carbon atoms can a) collide with other C atoms (or small carbon clusters) and eventually form new nucleation centre or, b) interact with previously formed nucleation centre and contribute to their further growth. The probability of the two cases will depend on the density of nucleation centres and the mean free path λ_{c-c} . If the λ_{c-c} is very small, it will be more probable for an atom to collide with another atom forming new nucleation centre, than to

reach already existing nucleation centres. The density of nucleation centres increases until the average proximity between two neighbouring nucleation centres becomes smaller than λ_{C-C} . Consequently, decrease of λ_{C-C} will increase the density of nucleation centres.

Therefore, higher density of nucleation centres is expected under the conditions with larger amount of the precursor, forcing supersaturation conditions.

In order to decrease the dimensions of the nanoparticles as well as to remove sp^2 carbons from the synthesised structures hydrogen was added to the precursor flow. SEM images of two different conditions can be seen in Figure II.30 and Figure II.31.

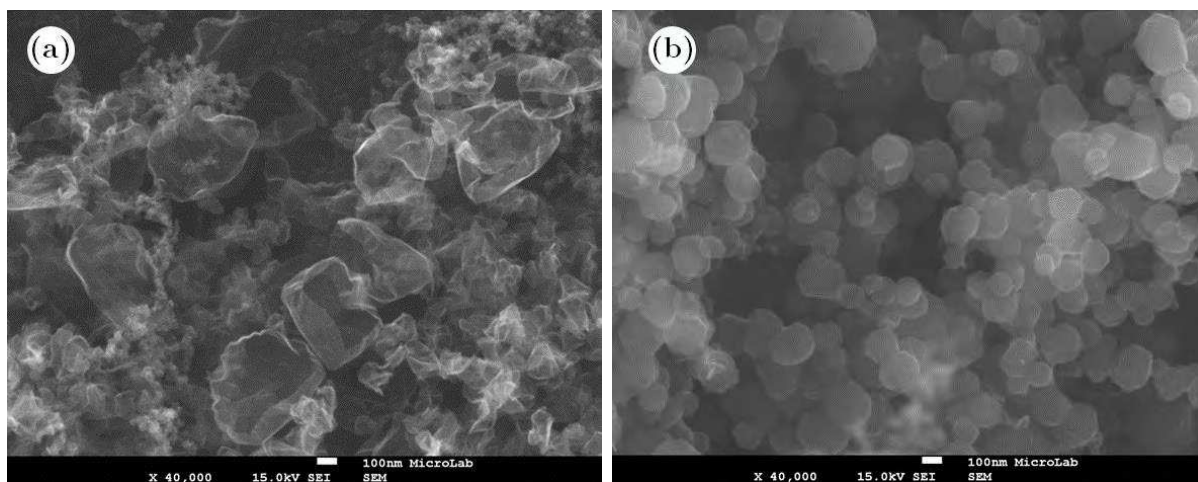


Figure II.30 - (a, b) SEM images obtained from different parts of the sample produced at $P = 1$ kW, $Q_{Ar}=2500$ sccm, $Q_{CH_4}=5$ sccm.

In Figure II.30 we can see that particle-like structures were also synthesized as expected but still some graphene sheets are present in the sample, although argon flux was doubled, leading to a decrease in residence time. Nevertheless, the huge changes are observed in Figure II.31(a) where the SEM image shows mainly nanoparticles formation, possibly diamond-like ones. This can be confirmed by Raman spectrum. The Raman spectrum is representative of the whole sample. The diameter of the particles in this samples ranges from 35-55 nm (see Figure II.31(b)).

Figure II.31- (a) SEM image of carbon nanoparticles. (b) Respective histogram of the particles diameter. (c) Measured Raman spectrum of the as-synthesized nanoparticles at $P=1$ kW, $Q_{Ar}=1000$ sccm, $Q_{CH_4}=5$ sccm $Q_{H_2}=2.5$ sccm; (d) deconvolution and fitting of the two broad features observed in the range 500-2000 cm^{-1} .

The Raman spectrum shown in Figure II.31(c, d), exhibits two major features, as it was also seen in Figure II.28(b, c): one broad peak between 1100 and 1400 cm^{-1} and a sharper one at around 1600 cm^{-1} . Yet, a very small peak at around 2700 cm^{-1} , with much lower intensity when compared with graphene spectrum Figure II.26, supporting the idea of reduction of sp^2 carbons by adding hydrogen to the plasma gas mixture. Some studies reveal this same very small broadened peak, assigning this to carbon onions[251]. As before, the complex shape of the Raman spectrum in the region 500-2000 cm^{-1} was fitted with four Lorentzian profiles centred at 1210, 1340, 1497, and 1600 cm^{-1} . Besides the dominating D and G bands, the weaker so-called M1 and M2 bands, which are always detected in the spectra of nanocrystalline diamond[188], [250], were also identified.

In addition to all this very impressive results obtained with methane as carbon-based precursor, it revealed to be of high importance to channel the research also for carbon dioxide conversion,

since nowadays it is still an issue to be solved. Therefore, the next step was to add CO₂ to the Ar-CH₄ microwave plasma. Figure II.32 (a) shows a SEM image of the carbon nanostructures produced at P= 1 kW, Q_{Ar}=2000 sccm, Q_{CH₄}=40 sccm and Q_{CO₂}=20 sccm. It is very similar to the one observed in Figure II.31(a), giving an idea that we are also in presence of nanodiamonds. To confirm this HRTEM as well as XRD analysis were performed on the sample (see Figure II.32 (b, c, d) and Figure II.33).

Figure II.32 - (a) SEM image, (b) HRTEM image and (c, d) respective FFT images of the two regions identified in the HRTEM image. Both diagnostics were performed on the carbon nanoparticles produced at P= 1 kW, Q_{Ar}=2000 sccm, Q_{CH₄}=40 sccm and Q_{CO₂}=20 sccm, at atmospheric pressure.

The high-resolution TEM image allowed to determine the interplanar distance by means of FFT (Figure II.32 (c, d)) of individual particles whose random orientation let lattice fringes to be observed. FFT is a configuration of reciprocal lattice points obtained from HRTEM image and is similar to that of electron diffraction (SAED) from the crystal planes. The measured lattice spacings match up well with interplanar distances from different diamond phases, including hexagonal diamond (lonsdaleite) (0 0 2) and cubic diamond (1 1 1). Figure II.33 shows a XRD spectrum of the sample presented in Figure II.32 and Table II-2 summarizes the measured d spacing, all of which within error compare favourably with reported values for lonsdaleite, cubic

diamond and n-diamond. In this spectrum it is possible to observe a pronounced peak at (0 0 2) (25.9°) that corresponds to graphite, showing that most likely it will be necessary to add H₂ to the mixture to eradicate sp² carbons from the sample. Note that this is the first result concerning CO₂ as carbon precursor.

Figure II.33 – XRD Spectrum of the nanoparticles produced at P= 1 kW, Q_{Ar}=2000 sccm, Q_{CH₄}=40 sccm and Q_{CO₂}=20 sccm, at atmospheric pressure.

Therefore, theoretical model must be applied to this system to tailor the plasma environment in order to find the range of conditions that can lead to a selective synthesis of nanodiamonds. Nevertheless, it was also possible to identify other peaks from diamond-like structures as lonsdaleite (1 0 0) (0 0 2) (1 0 1) (1 0 2) (1 1 0) (1 0 3) and cubic diamond (1 1 1) (2 0 0) (2 2 0). The plane (2 0 0) from cubic diamond suggests the presence of n-diamond. The lattice spacing obtained with the FFT of the HRTEM images validate the crystalline structure and are in excellent agreement with XRD results.

Peak	d (Å)	2 θ (°)	graphite		Hex. diamonds (lonsdaleite)		Cubic diamond	
			d (Å)	h k l	d (Å)	h k l	d (Å)	h k l
1	3.440	25.9	3.3756	0 0 2				
2	2.176	41.5			2.19	1 0 0		
3	2.108	42.9	2.1386	1 0 0				
4	2.062	43.9	2.039	1 0 1	2.06	0 0 2	2.06	1 1 1
5	1.981	45.8			1.92	1 0 1		
6	1.743	52.5					1.78	2 0 0*
7	1.670	55	1.6811	0 0 4				
8	1.530	60.5			1.5	1 0 2		
9	1.228	77.8			1.26	1 1 0	1.26	2 2 0
10	1.215	78.8	1.234	1 1 0				
11	1.181	81.5			1.17	1 0 3		
12	1.169	82.5	1.1603	1 1 2				
13	1.136	85.5	1.1208	0 0 6				

Table II-2 – Crystal structure analysis of XRD data present in Figure II.33. * Forbidden cubic diamond reflection. For XRD patterns identification ICDD data base was used, namely PDF-2 #190268, #060675 and #411487, which corresponds to lonsdaleite, cubic diamond and graphite patterns, respectively.

II.1.2.5. Summary

Free-standing carbon nanostructures are produced by injecting different carbon precursors, i.e. CH₄ and CO₂, into a argon microwave generated plasma environment. Selective synthesis of different carbon allotropes, i.e., few atomic layers graphene sheets and diamond-like nanostructures, is achieved by tailoring the plasma environment and thermodynamic conditions in the assembly zone of the reactor in a synergistic way. Sensitivity analysis of the influence of the main decomposition products' dependence on fluxes, namely background gas, carbon-based precursors and additional hydrogen percentage in the background gas mixture was performed [93], [212]. It was possible to verify that the increase of the background gas flow and hydrogen decreases sp² carbons presence leading to 3D structures formations, namely diamond-like structures, including hexagonal diamond (lonsdaleite), cubic diamond and n-diamond.

Additional work is required to relate the plasma specific properties and specific structural qualities of assembled nanostructures that, in turn, determine their electronic, mechanical, photonic properties, etc. The results about carbon precursor's flows should be further used as input data for mechanistic models to simulate the nucleation and growth processes of carbon nanostructures.

II.2. N-doping of graphene using a Ar-N₂ microwave remote plasma treatment

Self-standing N-graphene sheets were produced in a low-pressure microwave N₂-Ar plasma. Graphene sheets were exposed to the plasma for various durations and doped with nitrogen atoms, which incorporated the hexagonal carbon lattice contributing to the formation of different carbon-nitrides. Atomic nitrogen emissions at the substrate position in plasma were detected applying optical emission spectroscopy. Raman spectroscopy, X-ray photoelectron spectroscopy, transmission and scanning electron microscopy were applied for material characterization. The influence of the exposure time as well as the amount of nitrogen in the plasma on the characteristics of the treated samples has been investigated, being mainly localized at the graphene surface. Formation of new types of carbon-nitride structures was observed. Part of the results present in this section were published in [107].

II.2.1. Experimental setup

A slot antenna excited, surface wave sustained N₂-Ar plasma source [252], [253] was used for graphene samples doping/functionalization with nitrogen. The schematic diagram of the setup is shown in Figure II.34. A glass tube ($ID = 30$ cm and length $L = 45$ cm) constitutes the discharge vessel, which is headed by a water-cooled aluminium block ($ID = 24$ cm and length $L = 10.7$ cm) and closed at the top by a 10 mm-thick quartz window. The plasma vessel is evacuated by an Edwards diffusion pump (model 100 Diffstak 100) backed by an Edwards two-stage rotary pump (model BS2212), which provide a base pressure of about 10^{-6} mbar when no gases are injected into the chamber. Argon and nitrogen gases with high purity (99.999 %) are injected at the bottom of the chamber ($Q_{\text{Total}}=50$ sccm). The slot-antennas are cut in the broad wall of the feeding rectangular waveguide shown in Figure II.34. Microwave power of 600 W at $\omega/2\pi = 2.45$ GHz is fed to the chamber. The generator is isolated from the chamber by a high-power circulator with a high-power matched load connected to its third port. An impedance transformer matches the chamber impedance to the feeding waveguide. The other end of the waveguide is short-circuited. The plasma is created by the energy carried by surface waves propagating radially and azimuthally along the interface between the plasma and a quartz dielectric plate. The microwave power enters the vessel through a quartz window. The waves form a resonant eigenmode

satisfying the pertinent boundary conditions and the plasma takes discrete density values in average, which ensure that the resonant eigenmodes exactly appear at the excitation frequency (2.45 GHz). For stable operation of the system, selective excitation of a proper mode is necessary. A pure TM_{140} , i.e., an evanescent wave along z , surface mode excitation is considered. The power of the surface wave close to the interface sustains an overdense plasma. As the distance from the interface increases, the wave electric field decreases exponentially and vanishes at some critical distance ($z_{cr} \sim 1$ cm) [252], [253].

Figure II.34 - Experimental setup for graphene doping/functionalization with nitrogen.

According to the main mechanisms governing the plasma production and sustaining, the plasma source can be separated in two different parts. The first one is close to the interface (at about 1 cm from the quartz plate for the present conditions), where the surface waves are propagating, and their energy sustains the discharge; this is the active discharge zone of the plasma source. Due to diffusion, the plasma expands into a second region, where a “microwave electric field free” diffusion plasma is formed, for $z > z_{cr}$. Particle diffusion and heavy particle collisional processes are dominating in the remote plasma zone. As a rule, the axial length of the remote plasma zone is much larger than that of the active discharge zone.

For graphene nitrogen doping/functionalization, samples were processed in the remote plasma zone at a distance (z) of 4.5 and 7.7 cm from the quartz plate, considering different exposure times (5-15 min) as well as different nitrogen concentrations in the gas mixture (Ar-N₂) used for the plasma production, between 5-40%. Before the plasma treatment the synthesized free-standing graphene sheets were dispersed in methanol by ultrasonication bath and then applied onto cleaned glass substrates. After drying, the graphene sheets were firmly attached onto the glass. The samples were then placed on a quartz holder positioned in a remote zone of the plasma at the distances mentioned above.

II.2.2. Plasma characterization

Optical emission spectroscopy was performed using an “optical periscope” system which was placed inside the plasma (see Figure II.34). This system consists on a stainless-steel piston with an optical fibre inside. The top of the piston is terminated by an optical quality window and a right-angle prism. The plasma radiation radially impinged on the prism is deflected towards the axis, collimated by a lens and then collected at the end of the optical path by a quartz optical fibre, which leads it into the input slit of the Jobin-Yvon Spex 1250M spectrometer (2400 g/mm grating) equipped with both a CCD camera and a R928 Hamamatsu photomultiplier. The analog signal generated by the photomultiplier module is converted to a digital signal by the acquisition electronics DataScan2 and processed by SpectraMax software. This component is connected to a computer via a serial port, allowing the acquisition of data and remote control of the photomultiplier high-voltage.

The cryogenic, back illuminated UV sensitive CCD camera has a 2048 x 512 matrix, featuring a 13.5 μm pixel-size, which provides high spectral resolution. It is cooled to approximately 170 K with liquid nitrogen and operated via the CCD 3000 module that uses a 16 bit A/D converter to translate the signal from the CCD into digital signal. The current generated by the detector is sent also to data acquisition module DataScan2 and processed by SpectraMax software.

The plasma emission spectra in the 230-750 nm range was detected at two different axial distances (see Figure II.35). As seen from the figure the spectrum is dominated by Ar atomic lines. The nitrogen molecular bands and nitrogen atomic lines are shown in the insets made. Intense nitrogen atomic lines at 821.6 nm and 822.3 nm belonging to the transition N (3p \rightarrow 3s)

have been detected. As seen in Figure II.35 (a) the nitrogen atomic lines intensity decreases nearly twice as the distance toward the antennas increases from 4 cm to the double, almost linear progression. This behaviour is expected since direct electron impact excitation and ionization processes involving N atoms (see Figure II.35) decrease with the distance from the launcher.

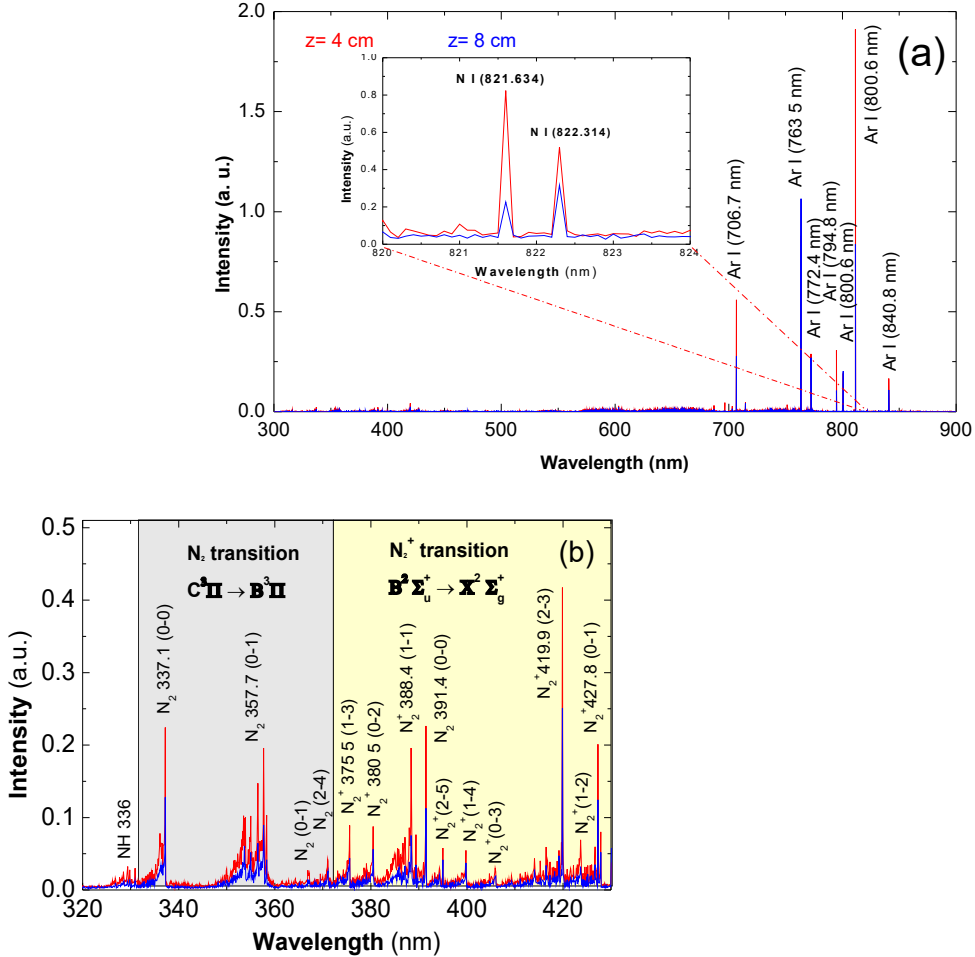


Figure II.35 – (a) Optical emission spectra emitted by N_2 -Ar plasma (10%-90%) at axial distances of 4 and 8 cm with an inset of Nitrogen atomic lines detected at axial distances of 4 and 8 cm ($P=600$ W, $p = 1$ mbar; $Q_{Total}=50$ sccm). Full spectra detected with a photomultiplier and the inset data detected with a CCD. (b) 1st negative system transition N_2^+ for the two distances. (c) A simplified energy-level diagram for nitrogen, giving rise to 1st negative system $B^2\Sigma_u^+ \rightarrow X^2\Sigma_g^+$.

The rotational temperatures corresponding to the first negative system $N_2^+(B^2\Sigma_u, v=0 \rightarrow X^2\Sigma_g, v=0)$ of nitrogen provide a good measure of the gas temperature (see Figure II.35 (b, c)). To this end, the rovibronic bands in the 389-391 nm range have been used. As seen from Figure II.36, the emission spectrum of the first negative system of nitrogen is

well established and the rotational lines are well resolved. These transitions can be used to measure the rotational temperature, provided that an accurate spectroscopic model is available. The LIFBASE code[214] has been used for this purpose. Both the measured and calculated spectra are shown in Figure II.36. The gas temperature varies in the limits 1200 - 1000 K when axial distance increases from 4 cm to 8 cm. Increasing the concentration of N₂ in the gas mixture from 5-40%, the gas temperatures from 900 to 1450 K (see Figure II.37).

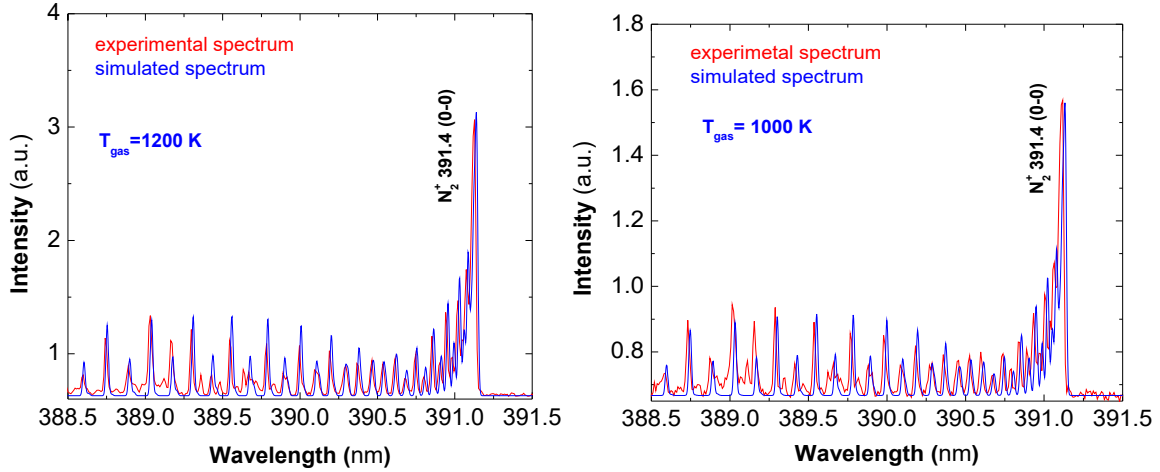


Figure II.36 - Experimental and simulated emission spectra of the 1st negative system of nitrogen. Experimental data obtained at (a) 4 cm and (b) 8 cm of axial distance. (N₂-Ar (10%-90%), P=600 W, p = 1 mbar; Q_{Total} = 50 sccm.)

Although the location in the remote plasma zone has been chosen to avoid to some extent the adverse ion bombardment effect, the measured gas temperatures indicated the presence of energetic neutrals, i.e. Ar atoms and N₂ molecules, at the locations where plasma processing of graphene sheets is performed. Therefore, the interaction of accelerated ions with graphene may also contribute to the defects formation and doping of graphene. Additionally, interaction of ions from plasma with graphene should be also considered. A simple estimation shows that the DC potential of the substrate with respect to the plasma potential, i.e.,

$$\Phi \approx \frac{kT_e}{2e} \ln \left[\frac{kT_e}{2\pi kT_i} \frac{M_{Ar}}{m_e} \right] \quad \text{eq. II-3}$$

may reach nearly 3 V assuming an electron temperature $kT_e \sim 0.5$ eV[252], [253] and an Ar ions temperature kT_i equal to the gas temperature.

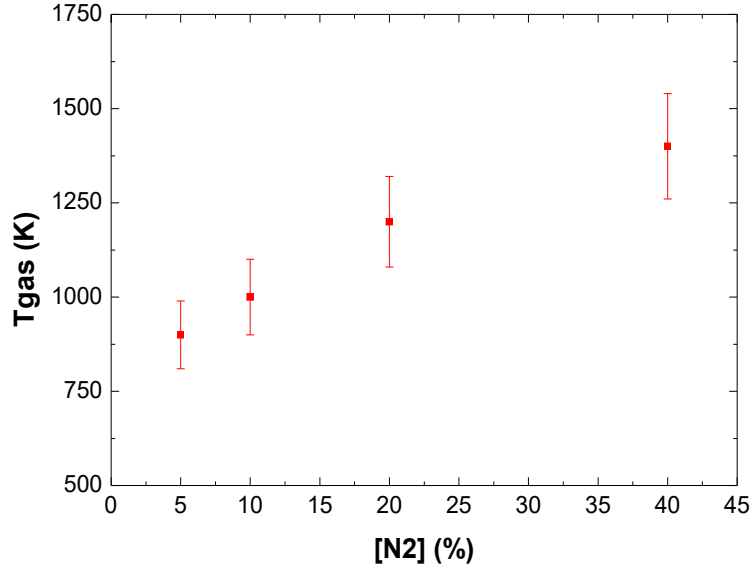


Figure II.37 – Gas temperature dependence of N_2 concentration ($[N_2]$) in the gas mixture of the N_2 -Ar plasma. Gas temperature obtained by the simulation spectra of the 1st negative system of nitrogen with LIFBASE[214]. Experimental data obtained with applied power of 600 W, $p = 1$ mbar; $Q_{Total} = 50$ sccm, considering different nitrogen concentrations, $[N_2] = 5$ -40%.

A 3D theoretical model describing the performance of the slot antennas excited microwave plasma source, considering the main plasma balances and accounting for the main bulk and surface elementary processes as well as wave electrodynamics is presented in [253]. This model defines in a self-consistently way the spatial structure of the plasma source, i.e. spatial distribution of population densities of ground-state molecules, atoms, excited species and charged particles containing the main energy exchange pathways as well as plasma-wall interactions [211], [254], [255]. The highly reactive $N(^4S)$ ground state atoms are considered the main nitrogen precursors in the plasma conditions considered. For a better demonstration of the $N(^4S)$ atoms spatial distribution in the reactor, an isosurface of $N(^4S)$ atom density of $8.0 \times 10^{13} \text{ cm}^{-3}$ was designed using this model (see Figure II.38). The figure that shows the $N(^4S)$ atoms distribution near the graphene sample holder. As seen the density is considerably high and homogeneous close to the sample holder than the one in the surroundings. To be noted that for lower N_2 percentages in the mixture, the density of ground state $N(^4S)$ atoms at around 8 cm of distance from the launcher is about 10^{12} cm^{-3} while the density of excited $N(^2P)$ $N(^2D)$ atoms is one order of magnitude lower[211], [254], [255]. However, increasing the nitrogen percentage up to 30 % the ground state atoms $N(^4S)$ density increased twice.

Figure II.38 - Isosurface of the nitrogen atom density $N^4(S)$ with a density of $8.0 \times 10^{13} \text{ cm}^{-3}$. The dielectric quartz disk is shown in the base of the figure as well as the sample holder cut in half. Plasma conditions: $P=600 \text{ W}$, $p = 1 \text{ mbar}$, N_2 -Ar plasma (10%-90%).

Under conditions considered, i.e. applied power of 600 W, pressure of 1 mbar, the ions that most likely will reach the substrate are Ar^+ , N^+ , N_2^+ , N_4^+ . Being Ar^+ ions ($1.9 \times 10^{10} \text{ cm}^{-3}$) the predominant positive ions at 5% nitrogen percentage in the mixture, one order of magnitude higher density than the nitrogen ions at $z = 7.7 \text{ cm}$. Increasing the nitrogen amount up to 30 % results in significant increase of nitrogen ions density, in this case approximately 1.5×10^9 , 2×10^9 and $4 \times 10^9 \text{ cm}^{-3}$ for N^+ , N_2^+ and N_4^+ ions, respectively. The Ar^+ ions density slightly decreased to approximately $6 \times 10^9 \text{ cm}^{-3}$. Keeping in mind that the ion energy distribution is spread over an energy interval the energy of the ions from the high energy part of the distribution can be significantly higher than an average energy of 3 eV. Therefore, accelerated Ar ions with an energy above 3 eV can impinge the samples, creating defects or doping them.

II.2.3. Material characterization

II.2.3.1. Techniques

The material characterization of the produced nanostructures performed includes Raman spectroscopy, SEM and XPS with the same characteristics described in section II.1.1 - Mass production of high-quality free-standing graphene and N-graphene sheets using an Argon-Ethanol microwave plasma.

The N-graphene sheets were further characterized by a high-resolution TEM JEOL JEM-2010F, operating at 200 kV accelerating voltage, equipped with an ultra-high-resolution objective lens pole-piece having a point-to-point resolution of 0.19 nm and a resolution limit at 0.11 nm ($C_s =$

0.48 mm, $\Delta f = 8$ nm), being sufficient to resolve the full lattice images of graphene. On the other hand, the graphene nanosheets have been also characterized by HRTEM with a Titan ChemiStem (FEI) operating at 200 kV accelerating voltage.

The samples produced at different concentrations of N_2 in the gas mixture were carried out on SPECS customized UHV surface analysis system containing sputter ion gun, PHOIBOS 100 spectrometer for energy analysis, dual anode Al/Ag monochromatic source and electron flood gun for the charge compensation. XPS spectra were taken using monochromatic Al $K\alpha$ line (photon energy of 1486.74 eV) in the fixed analyser transmission mode with the pass energy of 20 eV. The energy step and the dwell time are 0.1 eV and 2 s, respectively. The glass plates with the processed graphene powder were analysed as-received, without any further treatment. Non-treated, i.e., pristine graphene, sample was also analysed as a reference. The surface composition was determined using the atomic sensitivity factors provided by the XPS setup manufacturer. Survey spectrum in low resolution and high-resolution spectra of C 1s, O 1s and N 1s lines were collected from each sample. In addition, freshly cleaved highly oriented pyrolytic graphite was also measured as a reference for graphitic sp^2 carbon. Finally, valence band of all samples was also measured.

II.2.3.2. Results and analysis

II.2.3.2.1. Exposure time influence

The samples were processed in the remote plasma zone at a distance $z = 4.5$ cm from the launcher, considering different exposure times (from 5 to 15 min), with a fixed N_2 -Ar gas mixture (5%-95%).

Raman spectroscopy is the most efficient way to provide a quick and easy structural and quality characterization of the samples. Figure II.39 shows the Raman spectra of "pure" graphene sheets and the evolution of the Raman spectrum with plasma exposure time. N-graphene sheets were obtained at different exposure times in N_2 -Ar remote plasma. As seen in the spectra, there are three dominant peaks. The three peaks are attributed to the G band at ~ 1585 cm^{-1} , 2D band at ~ 2663 cm^{-1} , and D band at about ~ 1333 cm^{-1} . The G-band is related to the in-plane bond-stretching motion of pairs of sp^2 -C atoms. The D band, i.e., "disorder" band, is related to a series of defects: bond-angle disorder, bond-length disorder and hybridization that are caused by

heteroatom (nitrogen/oxygen) doping and structure defects by plasma treatment. Taking into account the ratio between the 2D and G peak integral intensities (>1.5) and the full width at half maximum of the 2D-band ($\sim 45 \text{ cm}^{-1}$) of the Raman spectrum of graphene sheets before plasma treatment (at the bottom of Figure II.39) the result is an indication of few-layer graphene sheets. Note that the graphene sheets were freely suspended on a glass substrate and the Raman spectra from different regions on the substrate were obtained.

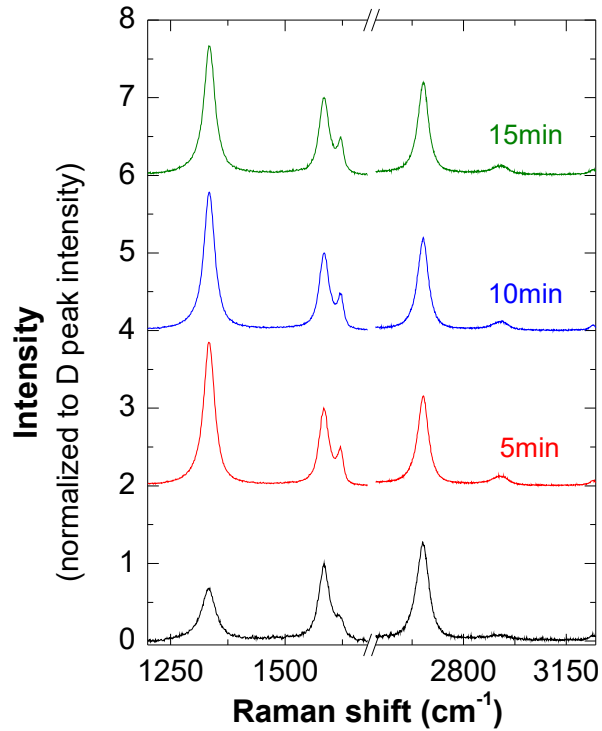


Figure II.39 - Raman spectra of graphene (at the bottom) and N_2 -Ar plasma treated graphene sheets ($P = 600 \text{ W}$, N_2 -Ar (10%-90%), $p = 1\text{mbar}$, $Q_{Total} = 50 \text{ sccm}$). The spectra from the bottom to the top correspond to 0, 5, and 10 min exposure time.

For non-treated graphene sheets, the D peak is the smaller and the ratio of the D-peak to the G-peak intensities is about 0.5. Remember that the edges of graphene sheets also contribute to the D-peak intensity. Moreover, after the plasma treatment, a well pronounced small shoulder at 1620 cm^{-1} on G peak appears. As seen from Figure II.39, the D/G intensity peak ratio increases nearly twice with the exposure time to the plasma treatment. The sp^2/sp^3 peaks area ratio increase can be correlated with the D/G peak intensity ratio increase in the case of nanocrystalline graphite[250]. Meanwhile, the 2D peak, the second order of D peak, decreases in intensity with the plasma treatment. As discussed in[14], the reduction in 2D intensity after

saturation of the D peak intensity is relevant to the excess charges from a dopant because the ratio 2D/G peaks intensity is sensitive to the charge density.

In Figure II.40(a) it can be seen the TEM image of a large area of high purity multilayer N-graphene sheets, with a size of 100 - 200 nm. A HRTEM image of the N-graphene sheets is presented in Figure II.40(b).

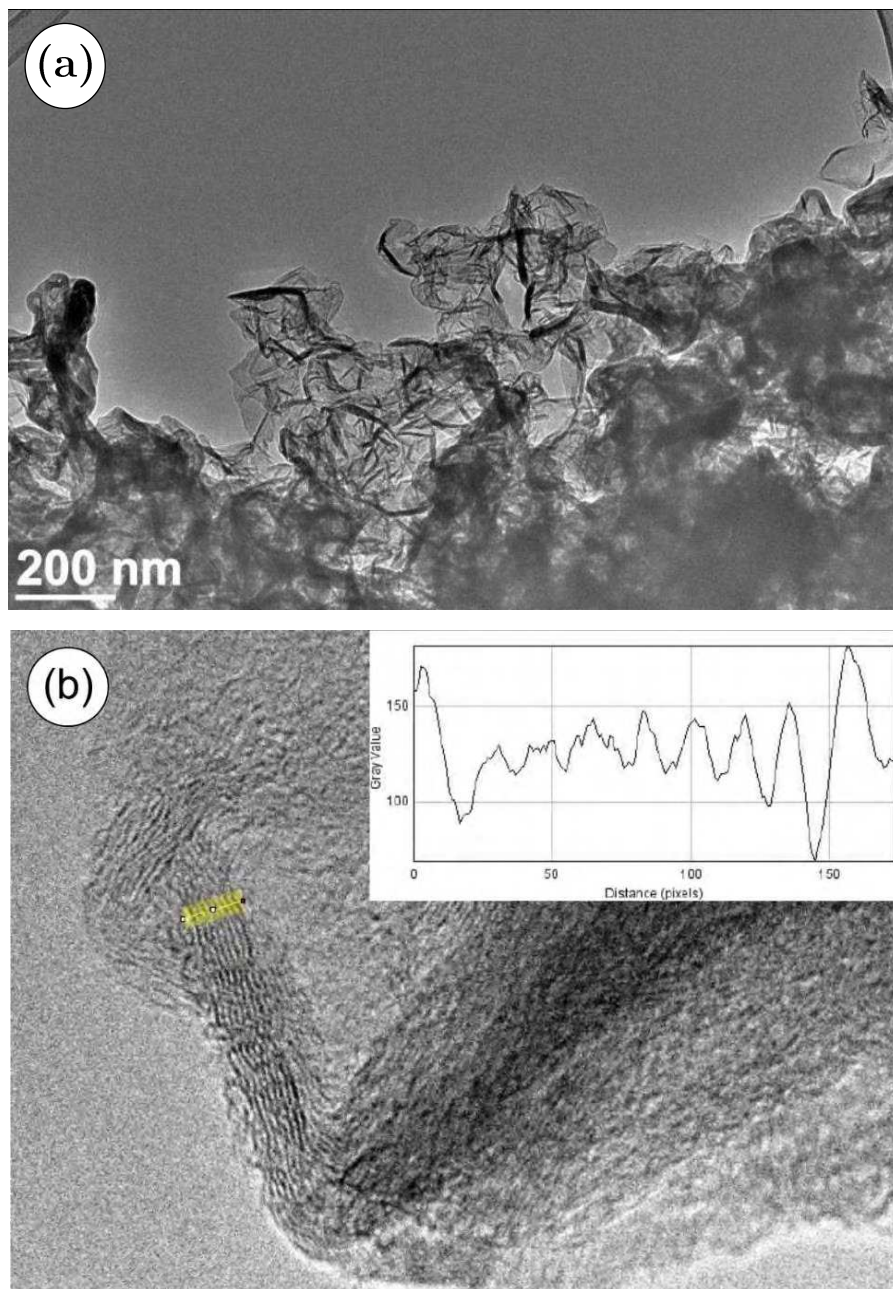


Figure II.40 - (a) TEM image of N-graphene and respective (b) HRTEM image with the edge of multilayered sheets consisting of eight layers. (inset) Graphic of the highlighted area in the HRTEM image that results from a FFT analysis. This graphic gives the distance between layers and the respective number of layers as well.

In principle, the layers of flat graphene cannot be seen by HRTEM. However, the edges of graphene sheets are folded and appear at HRTEM image as black fringes. From these folded edges the number of mono-layers can be determined. By looking at the graph of Figure II.40 it's possible to conclude that we are in presence of a multi-layered N-graphene with eight monolayers per sheet. The result indicates that the N-graphene sheets bear a well crystalline structure. We suppose that the number of mono-layers is mainly influenced by the dispersion of graphene sheets in methanol rather than by plasma doping. It should be stressed that dissolving graphene in methanol causes agglomeration of mono-layers and consequently an increase of the number of mono-layers in graphene sheets can be expected.

Furthermore, ex-situ XPS analysis has been performed to determine the elemental composition of the samples and to identify the chemical bonds. The survey XPS spectrum shown in Figure II.41(a) confirms the existence of N atoms attached to the graphene scaffold. Peaks appearing at about 284.5 eV, 400 eV, and 533 eV can be assigned to C1s, N1s and O1s lines, respectively. A detailed analysis of additionally appearing small peaks enables us to assign them to the glass substrate, i.e., Si 2p, Si 2s, and the Auger sodium line (Na_{KLL}). The estimation of the relative intensity of the O1s line, attributed to the glass substrate, is in accordance with the intensity of Si lines using the relative sensitivity factors from [256]. After removing the signal that is coming from the glass substrate, the elemental composition of N-doped graphene sheets was determined.

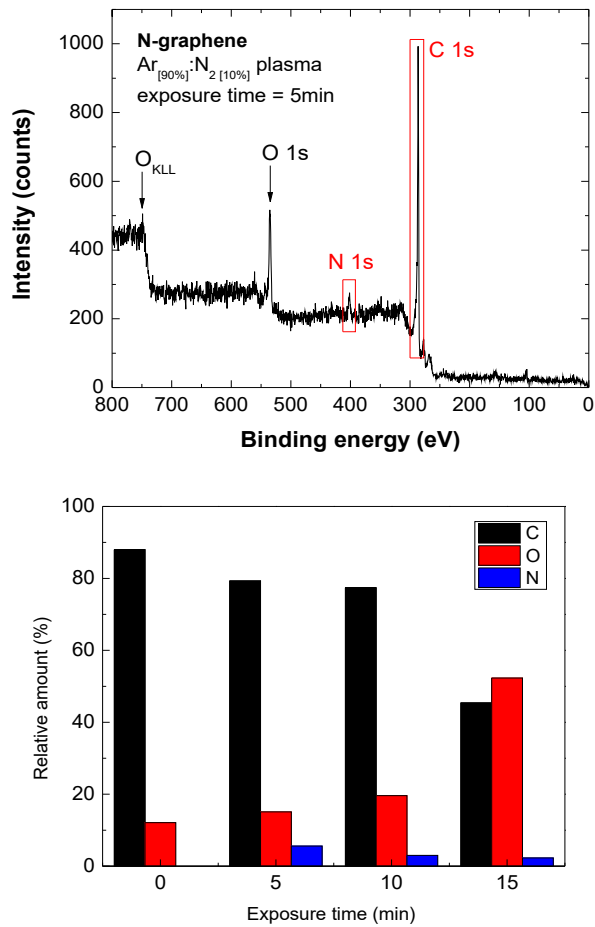


Figure II.41 – (a) XPS survey spectrum of N-doped graphene. (b) Evolution of the elemental composition of N-graphene with plasma treatment time ($P = 600$ W, N_2 -Ar (10%-90%), $p = 1$ mbar, $Q_{Total} = 50$ sccm).

The initial sample contains about 88 % of carbon and 12 % of oxygen. When the sample is treated by a pure Ar plasma for 5 min, the relative amount of oxygen increases to about 20 %. This is mainly due to sample's preparation method before the plasma treatment. Adding nitrogen to the carrier gas results in N-doping of graphene. The evolution of the elemental composition of N-doped graphene with plasma exposure time is shown in Figure II.41(b). As can be observed, the relative amounts of carbon and nitrogen drop with the exposure time, meanwhile oxygen rapidly increases. The largest amount of nitrogen (5.6%) is incorporated in the graphene scaffold at an exposure time of 5 min. It should be emphasized that the maximum nitrogen incorporated in graphene by applying simultaneous synthesis and doping of graphene in arc discharge is about 1% only [9].

The Argon plasma treatment creates structural defects on graphene, with an increased amount of unsaturated carbon atoms at graphene edge sites, which are very active to react with oxygen and form oxygen containing groups when exposed to air. In the case of the N₂-Ar plasma treatment, some nitrogen is also incorporated in the graphene scaffold, which further modifies the treated samples. Additionally, collisions with energetic heavy particles and different reactive species results in physical and chemical sputtering of the sample and consequently the loss of carbon material. Consequently, prolonged treatment destroys the sample and even reduces the amount of incorporated nitrogen. In the following, we analyse N 1s and C 1s photoelectron lines in order to reveal the nature of graphene modification by the plasma treatment.

Generally, several nitrogen functional groups in nitrogen doped graphene are expected. These include pyridinic-N (BE = 398.1-398.3 eV), pyrrolic-N (BE = 399.8-401.2 eV), and quaternary nitrogen N-Q (BE = 401.1-402.7 eV)[256]. Pyridinic-N (labelled as N-6) refers to nitrogen atoms at the edge of graphene planes, each of these N atoms is bonded to two carbon atoms and donates one p-electron to the aromatic π system; pyrrolic-N (labelled as N-5) refers to nitrogen atoms that are bonded to two carbon atoms and contribute to the π system with two p-electrons, i.e. each N atom is bound with two other C atoms forming a “pentagon”; in quaternary nitrogen structure (labelled N-Q) N⁺ ion is bound to four alkyl (aliphatic hydrocarbon) or aryl (aromatic hydrocarbon) groups (see Figure II.42(b)). Finally, some oxidized nitrogen can be also formed [102].

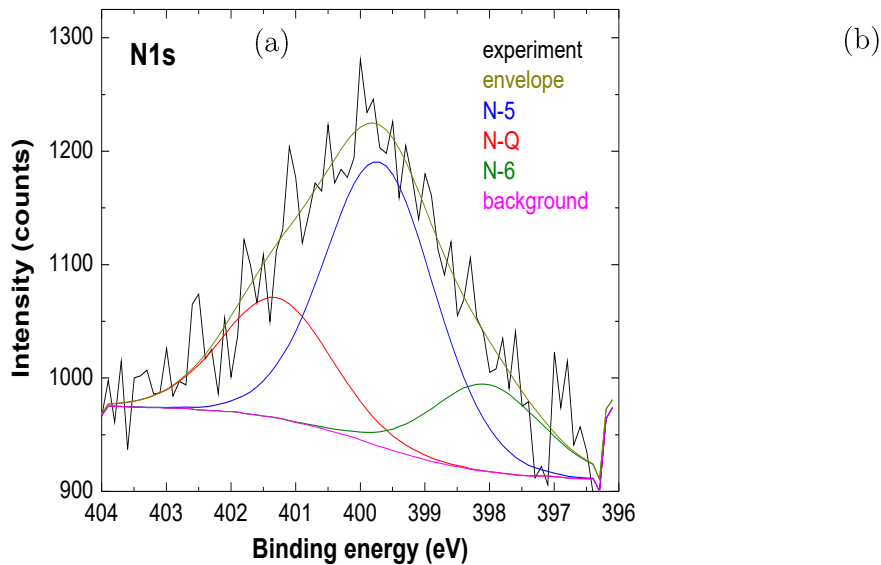


Figure II.42 - (a) XPS N1s spectrum of N-doped graphene sheets (5 min of treatment time). (b) Schematically presented nitrogen functional groups: pyridine N-6, pyrrolic N-5, quaternary nitrogen N-Q.

A detailed spectrum of the N 1s line taken from the sample treated for a 5min exposure time, together with the fitted result is shown in Figure II.42(a). For the peak model each contribution was described by a pseudo-Voigt Gaussian (70 %)-Lorentzian (30 %) line, and the background was determined using the Shirley algorithm. The constraint that each contribution has the same full width at half maximum (FWHM) was applied. The second (399.7 eV) and the third (401.3 eV) contributions can be addressed to N-5 and N-Q structures, respectively. Following the results in [102], peak 1 can be clearly interpreted as N-6. It should be also stressed that no oxidized nitrogen was observed.

The dependence of the relative amount of different nitrogen functional groups in N-graphene on plasma exposure time is shown in Figure II.43. As seen, the amount of pyridinic-N keeps nearly constant when exposure time increases from 5 to 15 min. Meanwhile, pyrrolic-N decreases and N-Q increases with the exposure time. It should be stressed that the role of the real "electrocatalytically active sites" is still controversial since their contribution to the catalytic activity is not well defined. In some studies, the enhanced electrocatalytic activity is attributed to pyridinic-N and/or pyrrolic-N. As can be seen from the results, these two types are present in the N-graphene analysed. To this end, an optimal exposure time of 5 min for N-graphene synthesis can be considered.

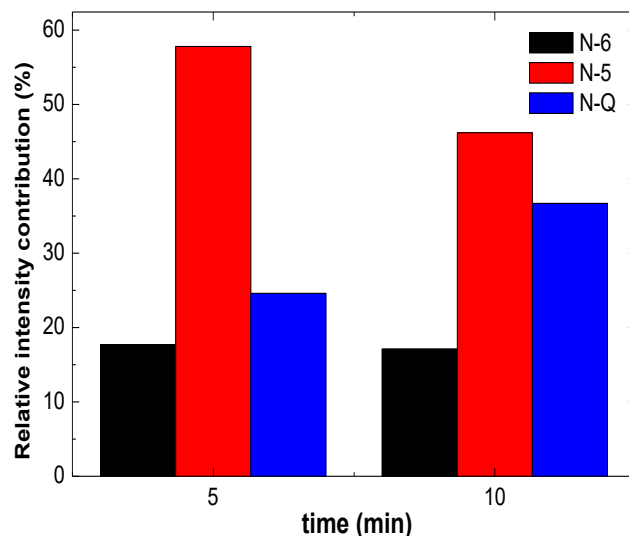


Figure II.43 - Time evolution of nitrogen functional groups attached to graphene scaffold ($P = 600$ W, N_2 -Ar (10%-90%), $p = 1$ mbar, $Q_{Total} = 50$ sccm).

The peak model for the C 1s line was chosen starting from the well-known fact that highly conductive samples, including different metals and graphite, have asymmetric photoelectron lines. The theoretical consideration yielded in Doniach-Šunjić (DS) profile [257], which then has to be convoluted to some symmetric profiles in order to describe different instrumental broadening effects. Similar to the approach of Kidambi et al. [258], for the peak model a DS profile with the asymmetry parameter of 0.01, convoluted by a pseudo-Voigt Gaussian 30% Lorentzian 70% profile was applied. Besides the optimum fit, the main criterion in choosing the peak model was to get chemical bond identification which will be consistent with the XPS composition analysis.

The detailed spectrum of the C1s photoelectron line taken from the graphene samples exposed to N_2 -Ar plasma for 5 minutes is shown in Figure II.44. The line can be well fitted into 5-6 components interpreted as follows: the contributions at about 284.5 eV and 285.3 eV are usually interpreted as sp^2 and sp^3 hybridized carbon, respectively; the peak at 286.3 eV can be related to epoxide (C-O-C) or C*-O-(C=O) groups; in the range 278-288 eV we expect contributions related to the carbonyl group (C=O) but also to C-N bond [220]; the peak at 288.7 can be interpreted as C-O-(C*=O) group; the peak at about 289.5 eV is related to carboxyl (COO) group. Finally, there is a satellite peak due to the $\pi \rightarrow \pi^*$ excitation, shifted for about 6.7 eV with respect to the sp^2 contribution. The results of the fitting of several samples are summarized in Table II-3.

Several conclusions can be made from these results. Firstly, the Ar plasma treatment increases the amount of oxygen bonds, which is fully consistent with the XPS composition analysis. In addition, it also decreases the sp^3 intensity, while sp^2 contribution does not change. Apparently, oxygen bonds were formed at the expense of sp^3 hybridized carbon, which consequently increases the sp^2/sp^3 peaks area ratio from about 3 to 4.3. Adding N_2 to the carrier gas contributes to both an additional decrease of the sp^3 component and also an increase of the sp^2 contribution. After 5 min of N_2 -Ar plasma treatment, the sp^2/sp^3 peaks area ratio reaches the value of 5.2. The contribution that was addressed to carbonyl group and/or C-N bond [220] clearly did not increase when nitrogen was incorporated into the graphene scaffold. Therefore, the increase of the sp^2 amount could be caused by the formation of N-6 and N-Q structures.

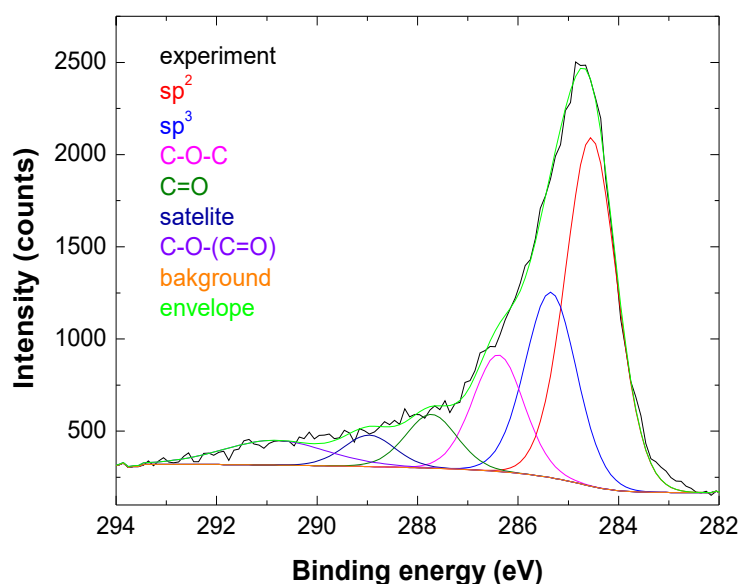


Figure II.44 - XPS C 1s profile modelled using Doniach-Šunjić profiles (asymmetry parameter $\alpha = 0.01$) convoluted by pseudo-Voigt $GL(70)$.

As it was already mentioned, the energy of heavy particles from plasma impinging graphene does not exceed several eV. These particles are able to recoil only loosely bound atoms in a direct knock-on collision while more stable structures, such as the graphene scaffold, cannot be affected. Consequently, short term plasma treatment of the sample increases the relative amounts of sp^2 hybridized carbon via etching of the less stable sp^3 -like structures and saturating the dangling bonds by nitrogen and oxygen atoms. It should be also emphasized that the observed increase of the sp^2/sp^3 area ratio is supported by the finding that D/G intensity ratio increases with the sp^2 content in the nano-crystalline graphite, as already discussed. However, a prolonged N_2 -Ar

plasma treatment of the graphene samples contributes to the decrease of the sp^2/sp^3 area ratio, a decrease of the carbon and nitrogen amounts, and an increase of the oxygen amount. Significant damaging of the graphene structure during the long-term exposure has to be caused by another mechanism, having slower etching rate. Chemical sputtering is probably responsible for the latter effect: it could create atoms with dangling bonds in the stable graphene structure, which can be then efficiently etched by collisions with heavy atomic and ionic particles. It should be also stressed that the relative amount of the N-Q contribution in N 1s line increases with the plasma exposure (Figure II.43). This fact supports the assumption that N-5 and N-6 contributions are related to sp^2 hybridized carbon while N-Q contribution corresponds to the sp^3 structure.

<i>Exposure time</i>	sp^2	sp^3	$C-O-C$, $C^*-O-(C=O)$	$C=O$, $C-N$	$C-O-(C^*=O)$	COO
<i>No treatment</i>	284.6 eV 60.1 %	285.3 eV 19.6 %	286.3 eV 11.7 %	288.1 eV 4.6 %	-	289.5 eV 2.4%
<i>5 min treatment with Ar plasma</i>	284.5 eV 60.1 %	285.3 eV 13.9 %	286.3 eV 11.0 %	287.4 eV 8.7 %	288.9 eV 4.8 %	-
<i>5 min treatment with N₂-Ar plasma</i>	284.5 eV 64.5 %	285.3 eV 12.4 %	286.3 eV 10.0 %	287.5 eV 6.8 %	288.7 eV 3.1 %	-

Table II-3 - Fitting results of the C 1s line by an asymmetric line; the satellite is not presented.

II.2.3.2.2. Concentration of N₂ in the gas mixture influence

The samples were treated in the remote plasma zone at 7.7 cm from the launcher for 3 minutes. Three different N₂-Ar mixture compositions were employed: 5%-95%, 30%-70% and 40%-60%, which were labelled with NG5, NG30 and NG40, respectively. SEM and TEM images of N-graphene show its morphology, which resembles the one of pristine graphene [3], [4], [93], [212], [259], evidencing that the graphene structure remains intact after N₂-Ar plasma treatment (see Figure II.45 (a, b)). Note that the TEM observations of N-graphene samples reveal graphene flakes up to 1 μm in size, composed by multiple layers (see Figure II.45 (c)), with typically 10-20 graphene monolayers per sheet, separated by 3.7 \AA , as directly measured from HRTEM images (see Figure II.45 (c)) and estimated by SAED pattern analysis (see Figure II.45 (d)). In analogy

of graphite structure, this layer separation would correspond to $\frac{1}{2}$ of graphite c-axis (002), with the separation of 3.35 Å. Therefore, we can confirm that individual layers are only weakly bonded and capable of hosting oxygen, nitrogen or argon molecules in the interlayer voids. From the SAED pattern in Figure II.45 (d) we can also verify preference in orientation of graphene layers, confirming that layers are not only randomly stacked together, but rather still connected by weak bonds.

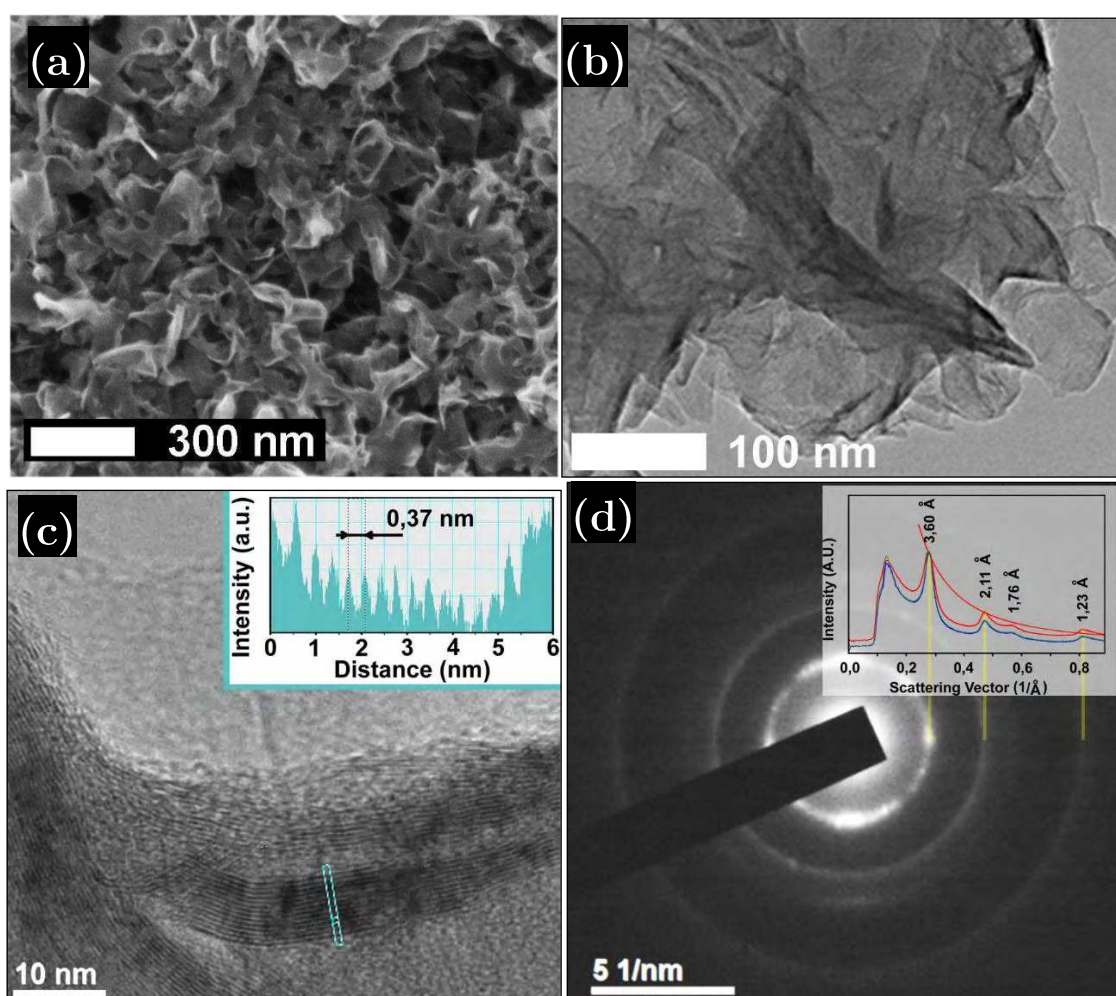


Figure II.45 – (a) SEM image, (b, c) TEM micrograph and corresponding (d) SAED of N-graphene synthesized with 30 % of N_2 (NG30). b) Curling of the edges of the graphene. c) Individual multi-layered N-graphene (10-20 layers) separated by 3.7 Å. d) SAED pattern of individual N-graphene sheet, showing preferred orientation of the individual sheets.

The Raman spectra of pristine graphene and N-graphene, obtained by averaging the measurements from few different spots of each sample, are shown in Figure II.46. All spectra present the three main features, assigned to D band at about $\sim 1332\text{ cm}^{-1}$, G band at $\sim 1583\text{ cm}^{-1}$ and the 2D band at $\sim 2661\text{ cm}^{-1}$. The D and D' (small shoulder of G peak) bands appearance can be due to bond-angle disorder, bond-length disorder and hybridization, caused by heteroatom doping and structure defects by plasma treatment.

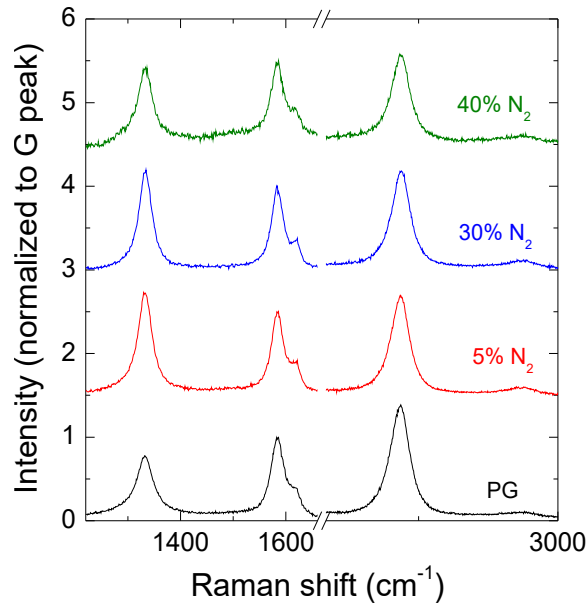


Figure II.46 – Raman spectra of graphene (black line) and N_2 -Ar plasma treated graphene sheets ($P = 600\text{ W}$, $p = 1\text{ mbar}$, $Q_{\text{Total}} = 50\text{ sccm}$) with different N_2 -Ar mixtures (5%-95%, 30%-70% and 40%-60%).

The 2D-band is an overtone of the disorder-induced D-band, being the most significant in the Raman spectrum of graphene. The position, full width at half maximum (FWHM) and intensity of 2D peak are used to determine the number of layers in graphene sheet [102], [260], [261]. In this case, the FWHM of 2D peak of PG is $\sim 50\text{ cm}^{-1}$, suggesting several monolayers graphene. Appearance of D-peak in the spectrum of PG can be due to the dangling bonds at the edges of the graphene sheets. In the Raman spectra of N-graphene samples an increase of the D-band is observed together with appearance of well-pronounced small shoulder of G peak at around 1620 cm^{-1} . A quantitative measure to estimate the degree of disorder in graphene is the D to G peaks intensity ratio ($I_{\text{D}}/I_{\text{G}}$) [102], [262]. By analysis of the Raman spectra present in Figure II.46, it was possible to observe that the values for $I_{\text{D}}/I_{\text{G}}$ increased from 0.85 (PG) to 1.15, 1.1 and 0.94 for NG5, NG30 and NG40, respectively. This implies that the nitrogen incorporation on the

graphene scaffold contributes to the increase in I_D/I_G values when compared with the one for pristine graphene, which means adding defects to the original graphene structure. The intensity ratio of 2D to G peaks, which is sensitive to the charge density, changes from 1.4 to nearly 1[14]. These tendencies indicate that changes are induced in the graphene with the plasma treatment, although the overall graphene character of the samples remains.

XPS survey spectra of doped graphene samples revealed presence of carbon, oxygen and nitrogen at the surface. The composition analysis of PG and N-graphene can be seen in Figure II.47 and PG sample is characterized with very small relative amount of oxygen ($\sim 1.6\%$), evidencing high purity of the graphene and being consistent with the Raman spectroscopy measurements shown previously (Figure II.46). Apart from the appearance of nitrogen in the samples due to the doping process, significant growth of the oxygen content can be also observed. For smallest amounts of nitrogen in the discharge gas, i.e. sample NG5, there is significantly less nitrogen than oxygen, which is consistent with the results obtained in the previous section (II.2.3.2.1 - Exposure time influence), where 10 % of nitrogen in the carrier gas mixture (Ar-N₂) was considered.

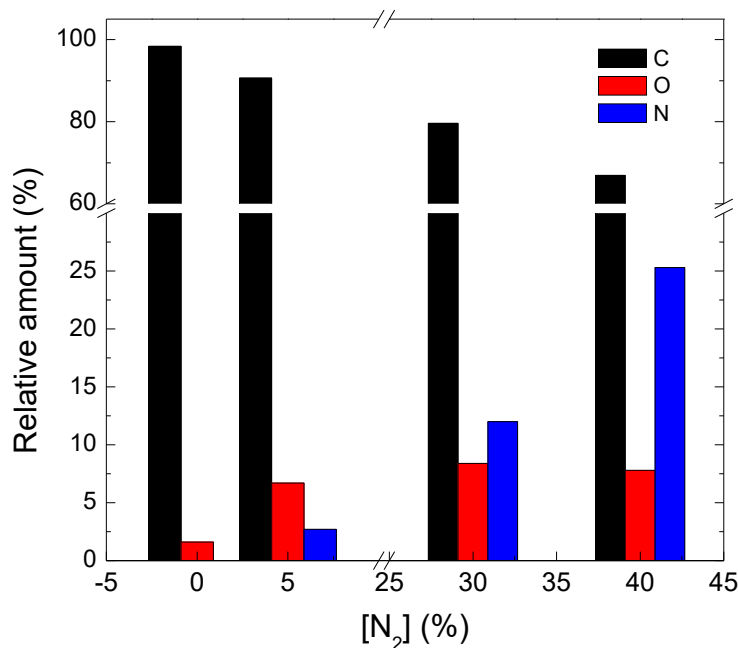


Figure II.47 - Evolution of the elemental composition of N-graphene with the concentration of N₂ ($[N_2]$) in the gas mixture. ($P = 600$ W, $p = 1$ mbar, $Q = 50$ sccm, exposure time = 3 min).

The nitrogen content grows rapidly for significantly larger quantities of N₂ in the discharge gas, while that the amount of oxygen seems to be saturated. Keeping this in mind, two regimes can be observed depending on the N₂ amounts in the discharge gas: for smaller concentrations of N₂,

nitrogen doping is accompanied with significantly higher content of oxygen; for higher N_2 fractions starting at 30 %, nitrogen atoms are the dominant doping agents. Consequently, creation of significantly different bonds is expected in these two cases. In the case of the sample NG5, nitrogen doping of graphene is expected, as already shown in the previous section (II.2.3.2.1 - Exposure time influence). High content of nitrogen in samples NG30 and NG40 opens a possibility for discrepancy from the graphene doping, and formation of new types of carbon-nitride structures. To note that the effect of accelerated ions impinging the graphene surface should also be taken into consideration at these conditions.

The N 1s lines were measured for the different samples and the one present in Figure II.48 corresponds to the sample NG30 and it is a good representative of the nitrogen photoelectron line from all three nitrogen containing samples (NG5, NG30 and NG40). The line can be deconvoluted in three contributions with the pseudo-Voigt Gaussian (70%)-Lorentzian (30%) profiles of the constant FWHM, after removing the background of the Shirley type, as it was done previously. The fitting results of the three samples are presented in Table 2.

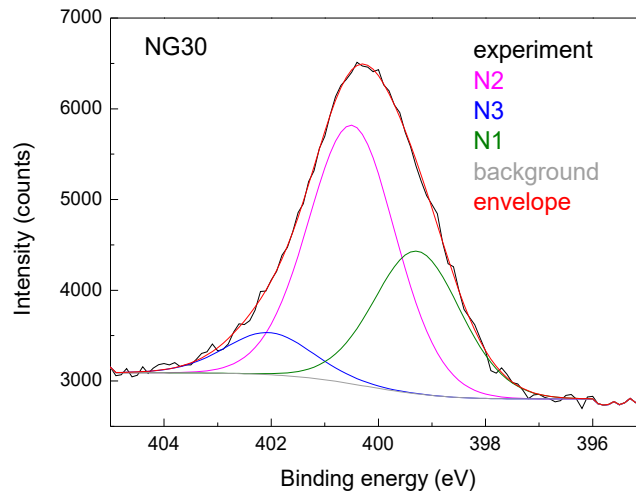


Figure II.48 – N 1s spectral line of sample NG30.

According to the Density Function Theory calculations of different carbon-nitride environments, contribution N1 at approximately 399 eV can be attributed to 2-coordinated nitrogen bound to sp^3 hybridized carbon[263], [264], also assigned to NH in hexagonal ring[234], [264]. The contribution N2 in the range 400-401 eV can be attributed to different kinds of 3-coordinated nitrogen bound to sp^2 carbon[264], [265], including so-called graphitic nitrogen[234] and pyrrolic nitrogen[107]. The contribution N3 at around 402 eV is most probably related to quaternary sp^3 hybridized nitrogen bound to sp^3 carbon[107]. Increase of the nitrogen content in the samples can

be clearly correlated with the decrease of bonds with sp^2 carbon and increase of the bonds with sp^3 carbon. C 1s line from the PG sample was fitted with Doniach-Sunjic profile with Shirley type background, where graphitic sp^2 and C-C sp^3 carbon are dominant contributions as expected from previous XPS analysis in this work. Estimated sp^2/sp^3 peaks area ratio is 11.5, confirming high quality of the pristine graphene.

Sample	N1 (eV/%)	N2 (eV/%)	N3 (eV/%)
NG5	399.1/19.9	400.2/70.0	402.3/10.1
NG30	399.3/32.2	400.5/58.3	402.0/9.5
NG40	399.4/17.8	400.7/46.3	402.0/35.9

Table II-4 – Table with N 1s fitting results for the 3 samples considered.

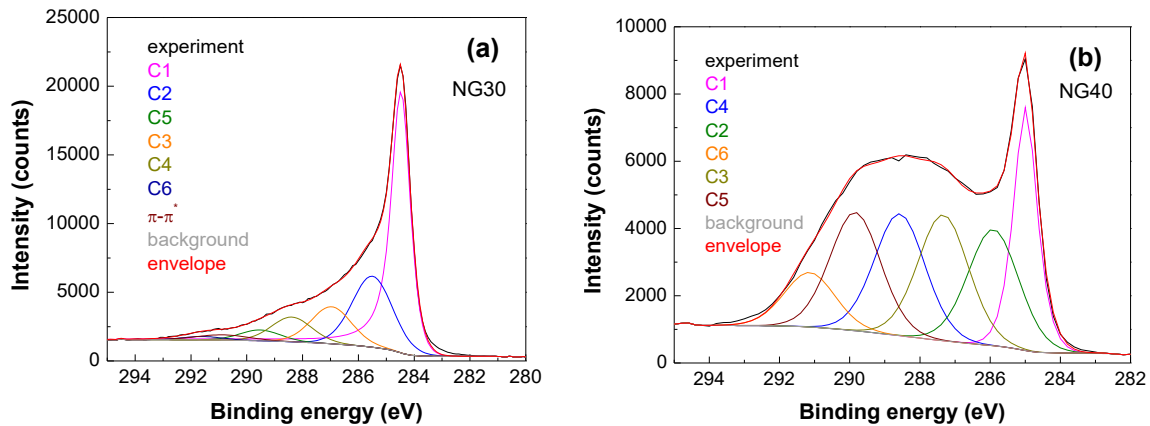


Figure II.49 - XPS C 1s line taken from NG30 and NG40 samples and the fitting results.

In the case of the samples with higher amounts of nitrogen content, i.e. NG30 and NG40, more than 50 % of the total line intensity belongs to the high energy tail attributed to bonds in which carbon is highly electropositive, and therefore non-conductive. For NG30 the C1 contribution corresponds to graphitic sp^2 carbon[107], as expected from the Raman spectroscopy TEM and SEM analysis. Therefore, only part of the spectrum originates from graphene (contribution C1), which was fitted with the peak having the profile used in low nitrogen content samples. The sp^2 contribution is accompanied by a wide symmetric peak corresponding to the characteristic shake-up $\pi \rightarrow \pi^*$ satellite. The rest of the contributions (C2-C6) were fitted to the symmetric pseudo-Voigt Gaussian (70%)-Lorentzian (30%) profiles, which is the standard choice for carbon

compounds. The constraint related to the constant FWHM was applied only to C2-C6 contributions, being much wider than the graphene peak.

The peak position of the NG40 sample is at 285 eV, implying absence of graphene measured volume. Therefore, the first contribution C1 is attributed to saturated hydrocarbons[266] as well as to sp³ carbon[107]. All other contributions are practically at the same positions as in the case of NG30 sample.

<i>Sample</i>	<i>NG5</i>		<i>NG30</i>		<i>NG40</i>	
<i>Peaks</i>	eV/%	possible contributions	eV/%	possible contributions	eV/%	possible contributions
C1	284.5/ 60.5	graphitic sp ² C[107]	284.5/ 60.5	graphitic sp ² C[107]	285.0/ 18.4	sp ³ C[107], C-H bonds[266]
C2	285.2/ 15.6	sp ³ C[107], C-H bonds[266]	285.5/ 23.9	sp ³ C [107], C-H bonds[266] and sp ² C bound to N[264]	285.9/ 17.7	sp ² C bound to N[264]
C3	285.8/ 9.9	CN bonds in graphitic environment[234], [264]	286.9/ 13.2	CN bonds [264], sp ³ bonded C to two N[263] (N)O-C=O[266]	287.3/ 19.1	CN bonds [264], (N)O-C=O[266], O-C=O[266]
C4	286.5/ 7.4	C-OH, sp ³ CN bonds[263]	288.3/ 9.2	Carbonyl group (C=O) in imide system, (N)O-C=O[266] sp ³ CN bonds[264]	288.6/ 18.5	sp ³ CN bonds [264] >C=O [266]
C5	287.2/ 4.2	CN bonds [264], (N)O-C=O[266], O-C=O[266]	289.6/ 4.6	sp ³ CN bonds [264]	289.8/ 18.0	sp ³ CN bounds [264]
C6	288.2/ 2.4	Carbonyl group (C=O) in imide system and sp ³ CN bonds[264]	291.4/ 2.8	sp ³ CN bonds[264]	291.1/ 8.3	sp ³ CN bonds[264]

Table II-5 – C 1s fitting results for NG5, NG30 and NG40 and respective contributions identification.

The absence of graphene might be contradictory to the conclusions taken from the Raman spectra only at first sight. Plasma processing is expected to affect only several outermost layers, namely those observed by XPS. It is likely that the graphene observed in NG30 sample originates from the somewhat deeper layers non-affected by the plasma processing. The contributions above 286

eV are most likely assigned to CN bonds[234], [263], [264], [266] (Table II-5). In addition, the binding energy increases with the number of nitrogen neighbours.

II.2.4. Summary

We have demonstrated the production of N-graphene using a microwave N₂-Ar plasma treatment of graphene sheets. Free standing graphene sheets were subjected to the remote region of the plasma for different exposure times and nitrogen concentrations in the N₂-Ar gas mixture at fixed applied power (Power =600 W), pressure (p=1 mbar) and total gas flow (Q_{TOTAL}= 50 sccm). Optical emission spectroscopy has been applied to monitor the nitrogen atoms, gas temperature and electron density at the graphene sheets' position. Raman and X-ray photoelectron spectroscopy (XPS) techniques have been applied to characterize the produced N-graphene, along with transmission electron microscopy (TEM) to study the morphology and structure of the samples.

The results demonstrate that the level of doping and type of functional groups attached to graphene scaffold can be controlled by changing the exposure time to the plasma treatment, while keeping the nitrogen percentage constant. The maximum level of nitrogen doping of graphene achieved was 5.6%. Additionally, a short-term plasma treatment increased the sp²/sp³ area ratio, which is apparently related to both C-O bonds formation (at the expense of sp³ carbon) and N doping (which increases the amount of sp² carbon via formation of pyridine- and graphitic-like structures).

On the other hand, it was also possible to verify the influence of nitrogen content in N₂-Ar surface wave plasma treatment on the samples scaffold. Both TEM and Raman spectroscopy results revealed the graphene-like character of the samples is unchanged after plasma treatment and defects were added with the plasma processing to the graphene sheets. XPS analysis showed significant modifications in the graphene sheets structure, mostly at the sample surface, as the nitrogen concentration in the gas mixture increases. The XPS results also revealed that the percentage of doping increased from 2.7 to 25 at.% with the nitrogen concentration in the plasma gas. A doping level of around 12 at.% was achieved without changing the few-layer graphene structure, for the concentration of N₂ of 30 % in the plasma gas mixture, which is much higher than reported for arc-discharge plasma methods [267].

In addition, considering the case of 5 % of nitrogen in the N₂-Ar plasma gas, the nitrogen was incorporated in the graphene structure predominantly in the form of imide group and graphitic bonds (~70 %) and as N bound to sp³ carbon (~30 %). Moreover, the increase of the nitrogen content in the gas mixture was found to significantly contribute to the formation of carbon-nitride structures. The effect of accelerated ions impinging the graphene surface should also be taken into consideration at these conditions.

Further work should focus on identification of these carbon-nitride structures.

II.3. Graphene applications using plasma-based methods

Graphene functionalization as well as graphene-polymer nanocomposites are some of the key topics in materials research, since they find extensive application in polymer science and technology due to its extraordinary mechanical, thermal, electrical, optical, and chemical properties[21], [22]. Recently, graphene-based composites have attracted both academic and industrial attention since it can produce a significant improvement in properties at very low filler content. The modification of graphene and its usage in the fabrication of graphene-polymer nanocomposites have been studied. These nanocomposites due to their extraordinary properties[268], [269] can be used in many applications in lithium ion battery with high energy, supercapacitor, catalysts, solar cells, nanodevices, chemical sensors, biosensors and biomedical fields.[270] Besides, active bio-functionalized graphene devices, like electrical graphene biosensors, have been studied and revealed high performance on detecting large-sized biological analytes as cancer cells[271]. To realize these applications, it is necessary to transfer the FSG films to target substrate with large-area, clean, and low defect surface, which are crucial to the performances of large-area graphene devices and this remains still a challenge.

Therefore, one of the aims of this work is to find a simple method for deposition and plasma post-treatment that do not change the nature of FSG, allowing its usage for a wide range of applications, including biosensing ones[24], [25] and coating inks [26], [27].

Material characterization techniques

The morphology graphene, functionalized graphene and graphene nanocomposites were studied by Scanning Electron Microscopy (SEM) using a Zeiss-Supra device. The SEM images were made with extraction voltage ranging from 3 to 10 kV, with a 20 μ m shutter and a typical current of 160 μ A. The elemental composition was identified by means of X-ray Photoelectron spectroscopy (XPS). XPS analysis were performed at synchrotron radiation source facility BESSY II (Berlin, Germany), HE-SGM beamline storage ring (PREVAC end station provided by Professor Ch. Wöll). The elemental depth information was 2.1 nm by keeping the photoelectron peaks of different elements at the same constant kinetic energy[272], [273]. The beamline monochromator allows fast scanning over the energy ranges of interest (100 eV - 700 eV). NEXAFS measurements

were performed considering different incident angles (20-90°) relative to the substrate surface. The data was collected in respect to the C K-edge to characterize the carbon chemistry of the produced free-standing graphene, in the partial electron yield (PEY) mode (few nm depth), using a home built double channel plate detector. The energy resolution was ≈ 0.40 eV. The raw NEXAFS spectra were corrected for the beam line transmission by division through a spectrum of a clean, freshly sputtered Au sample. Alignment of the energy scale was accomplished by using an I0 feature referenced to a C 1s $\rightarrow \pi^*$ resonance at 284.9 eV from a fresh surface of a graphite foil standard sample[215]. Vibrational Raman spectroscopy studies were performed using a Renishaw Invia Reflex spectrometer at ambient conditions. The spectra were collected under a Leica DM2500 optical microscope (50 objectives/N.A. $\frac{1}{4}$ 0.75) and a grating of 1800 l/mm. Very low incident power (~ 1 mW) was used to avoid any modification of the analysed samples. The laser excitation wavelength used was 532 nm.

II.3.1. Samples preparation for plasma treatment/polymerization

Nowadays, there is an urgent need to develop a method to transfer the FSG films to target substrate with large-area, clean, and low defect surface, which are crucial to the performances of large-area graphene devices and this remains still a challenge.

The collected FSGs (synthesised as described in section II.1.1 - Mass production of high-quality free-standing graphene and N-graphene sheets using an Argon-Ethanol microwave plasma) were deposited, without the need for exfoliation, using a simple dispersion method, which enable deposition on various substrates. Two solvents were tested, distilled water and methanol. Both suspensions were submitted to sonication process to disperse the graphene sheets, turning possible its deposition. As it can be seen to the naked eye (see Figure II.50) the suspension done with methanol is stable for a while at least for 4h30 after the process of sonication, living the possibility to be used for inkjet-printing as an example. After one day it's possible to verify that the mixture presents already two phases, one with very small particles on top and the other with bigger particles, supposedly graphene sheets, on the bottom (see Figure II.50).

Figure II.50 – graphene-methanol suspension preparation. (a) FSG as produced. (b) graphene and methanol. (c) graphene-methanol suspension after 30 min sonication, (d) after 1h30min, (e) after 4h30, (f) after 1 day, (g) after 2 days and (h) after 3 days.

On the other hand, the water-graphene suspension was not very successful for that purpose, since we always obtained a two phases preparation. Clearly a thin film of graphene was on top and water at the bottom (see Figure II.51). This reveals very roughly that graphene with low level of oxygen is highly hydrophobic.

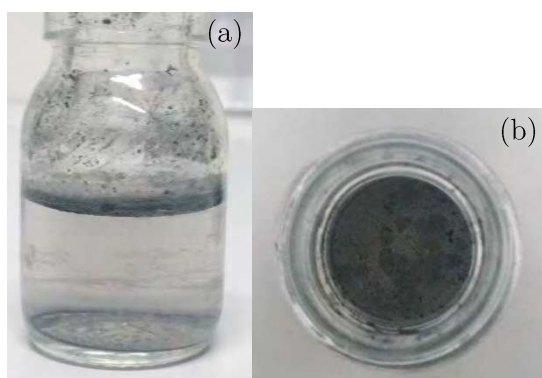


Figure II.51 – graphene-water suspension preparation. After one day of sonication. (a) Side view. (b) top view.

Considering these two phases in both suspensions it was deposited the bottom preparation for methanol one and top for water one over separate silicon oxide substrates in order to perform Raman spectroscopy of the samples and the results can be seen in Figure II.52. Considering the results present in Figure II.52 it is possible to see that for the methanol-graphene preparation, taken from the bottom of the vessel (see Figure II.50), the ratio of intensities of 2D to G peaks increases from 1.1 to 1.3, and at the same time the FWHM of the 2D peak decreases. In conclusion, a selection of material is achieved, where we are able to separate the graphene sheets

with less monolayers per sheet from others, considering the Raman spectrum from the untouched graphene sample (graphene as produced).

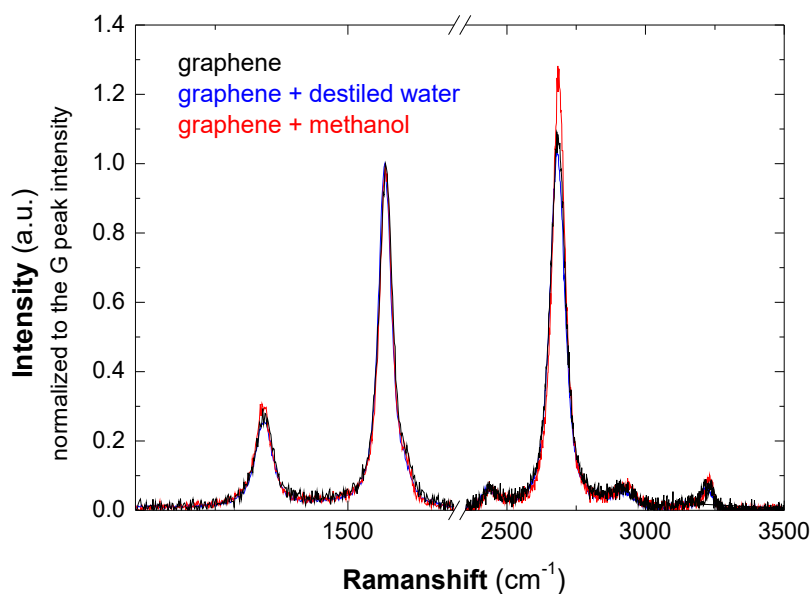


Figure II.52 – Raman spectra for three different samples. One is graphene as produced (black line), the other two correspond to graphene samples in suspension with methanol (red line) and with distilled water (blue line).

On the contrary, considering the water-graphene preparation no changes are observed in the Raman spectra (see Figure II.52), as expected, since in fact no mixture is verified along the preparation process (see Figure II.51).

Afterwards, the stability of the methanol-graphene suspension was tested performing UV-visible spectroscopy on the samples (see Figure II.53). The UV-visible absorption process occurs when a molecule absorbs ultraviolet or visible light, inducing excitation of the electrons from ground state.

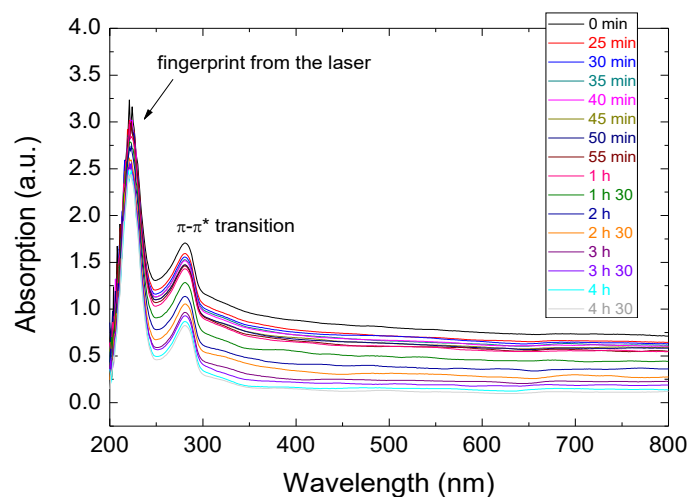


Figure II.53 – UV-visible absorption spectra showing the evolution of methanol-graphene suspension with time. The observation was performed at the bottom of the vessel.

The spectra obtained are in agreement with the previously reported results with characteristic sharp absorption peak at about 270 nm, which has been assigned to the $\pi\text{-}\pi^*$ transition of the C=C bonds in the previously reported results[274]. Also analysing the UV-visible spectra it can be seen that the suspension is quite stable for the first 4h30. Nevertheless, the separation is gradually being established since it is observed a drop in intensity of the laser signal from 3.25 to 2.5 confirming the conclusion retrieved from the brief analysis of the images present in Figure II.50.

Furthermore, NEXAFS spectroscopy was performed on both methanol-graphene and water-graphene preparations (see Figure II.54).

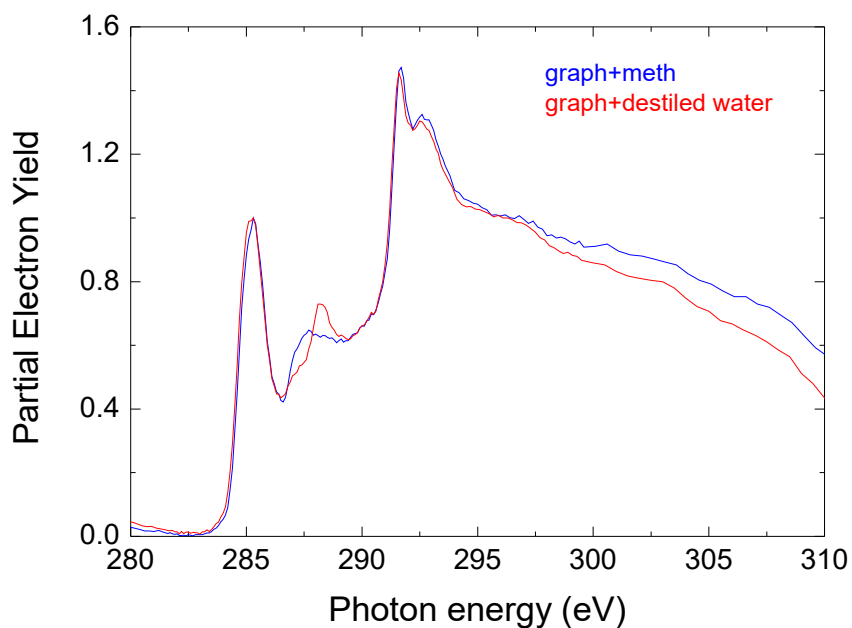


Figure II.54 – NEXAFS spectra of two different graphene samples. One corresponds to the methanol-graphene preparation (blue line) and the other one corresponds to the water-graphene one (red line).

The NEXAFS spectrum of the water-graphene suspension reveals a very sharp peak at around 288 eV, which is commonly assigned to O-containing functional groups (e.g. carbonyl π^* resonance of C=O, resulting from oxidation of defects in the graphene structure)[203]. Besides, for the methanol-graphene suspension very residual almost not perceptible presence of impurities in the fingerprint region between 286 and 290 eV is observed. Therefore, considering all the previous results reveal that the most promising suspension to be used for graphene deposition on different substrates is the methanol-graphene preparation.

Moreover, several substrates were used to test adhesion of the graphene in suspension, including Kapton, Mylar, PA, PLLA and PET of different thicknesses (see Figure II.55).

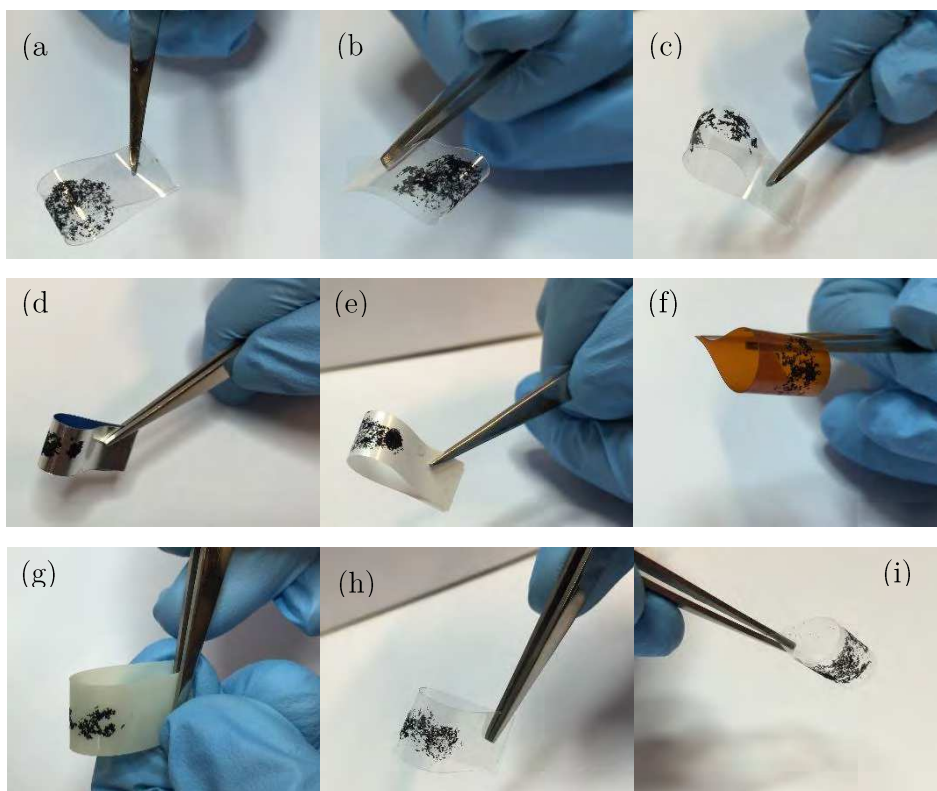


Figure II.55 – graphene suspension deposited on different polymers. (a) PET 125; (b) PA 6; (c); (d) Al on PET; (e) PET50 (f) Kapton; (g) Mylar; (h) PET 100; (i) PLLA.

The graphene adhesion to different substrates was successfully achieved but improvements concerning the homogeneity of material displacement should be carried out, since it does not spread equally along the surface. The heterogeneous displacement of the graphene sheets is mainly due to Van der Waals forces and it can be avoided by adding some organic solvents or by simple functionalization of the graphene sheets.

II.3.2. Polymer-graphene nanocomposites using a plasma polymerization method

After graphene sheets deposition on silicon oxide wafers by means of graphene-methanol suspension process aniline polymerization was performed over the respective samples using a Ar-ANI plasma deposition method[275]. The plasma polymer deposition consists on placing the graphene samples in a remote zone of the capacitively coupled radiofrequency (RF) plasma for different processing times (see Figure II.56). The reactor is a cylindrical, stainless steel chamber with a diameter of 85 cm and a height of 85 cm. A RF power of 5 W was applied, while maintaining 0.18 mbar pressure in the chamber, i.e. constant flow of Ar (20 sccm) and ANI (1 sccm). A turbo molecular pump (Adixen ATH 500 M, Pfeiffer Vacuum) in combination with a primary pump (Duo 20M, Pfeiffer Vacuum) were used for the vacuum system. The reactor was pumped to a pressure of 10^{-6} mbar before each process. The samples were submitted to a RF discharge at 13.56 MHz, with 5.5 cm of distance between the circular stainless-steel electrodes. The lower electrode was grounded while the upper electrode was powered with 5 W with a pulsed frequency from 25 to 200 Hz by a frequency generator (SMC 100 A, 9 kHz-1.16 GHz, Rohde & Schwarz) and amplifier (BBA 100, 0-160 W, Rohde & Schwarz).

Figure II.56 – Experimental setup used for PANI films deposition.

The aniline vapor is generated from liquid aniline (Sigma Aldrich 242284), with *Omicron Technologies Nano Source* device. The volume polymerization of the aniline growth on the graphene samples was monitored by means of in-situ multi-pass FTIR spectrometry (developed with Bruker from the Vertex 70/70v system, with a white cell, passing through the plasma approximately 40 times, with 2 cm² of beam cross section) and plasma ion mass spectrometry (HIDEN EQP 1000) (see Figure II.57).

The graphene-polymer nanocomposites characterization was done by means of SEM (Zeiss Supra 40), NEXAFS and Raman spectroscopy.

Figure II.57 – FTIR in-situ (developed with Bruker from the Vertex 70/70v system) and mass spectrometry (HIDEN EQP 1000) apparatus.

Firstly, in order to identify the species involved on the polymerization process an RGA spectrum was collected. As expected, several neutral species were observed, including mass 40 that corresponds to Argon and mass 93 assigned to aniline. Afterwards, when Ar-ANI plasma is ignited mass spectrometry of positive ions was performed, and it is possible to observe plasma polymerization, where the monomer molecule is dissociated initially by electron impact, leading to a partial fragmentation of the monomer into different kinds of radicals and ions (see Figure II.58(b)). The species observed in the positive ions spectrum includes the single ionized aniline molecule (93 amu) as well as species with higher masses than the original ones, which confirms

volume plasma polymerization, leading to the nanoparticles or thin films formation.[276], [277] In the spectrum it was possible to identify several ions, such as $C_{12}H_{13}N_2^+$ at 185 amu, $C_6H_6^+$ at 78 amu, C_4H_2 at 50 amu and $C_2H_2^+/CN^+$ at 26 amu.

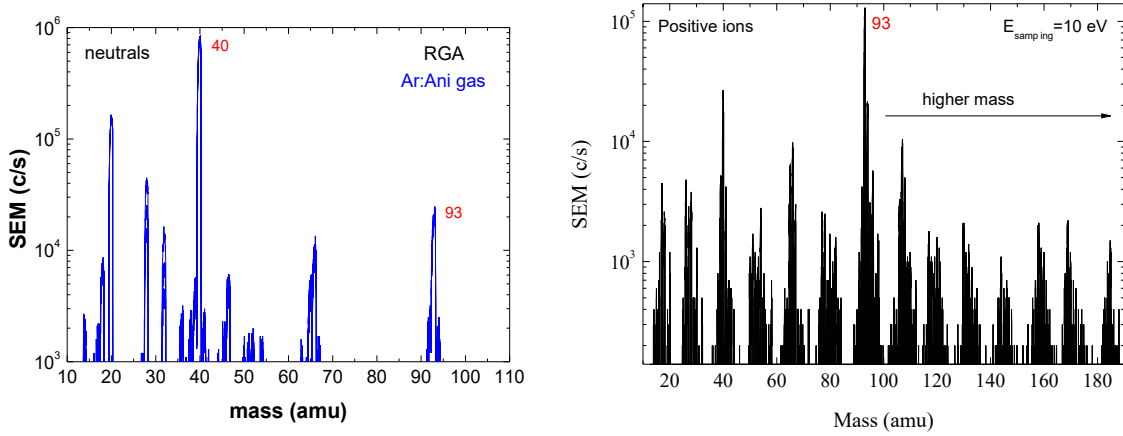


Figure II.58 – (a) RGA spectrum of Ar-ANI gas mixture before plasma ignition ($Q_{Ar}=20$ sccm and $Q_{ANI}=1$ sccm at $p=0.18$ mbar). (b) Mass spectrum of positive ions when the plasma is ignited with a 5 W of applied power.

Since the main propose of this work consists on depositing a very thin film over the graphene sheets (previously displayed on a SiO_2 wafer), it was of high importance to perform in-situ FTIR spectroscopy. FTIR measurements can provide information about nanoparticles formation, because when they are formed Rayleigh/Mie scattering phenomena are observed at higher wavenumbers see Figure II.59(a) [277], [278].

Figure II.59(b) illustrates clearly film formation for pulsed discharges at low frequencies (below 100Hz). Therefore, in our case a frequency of 25 Hz has been used to easily control the thickness of the deposited film.

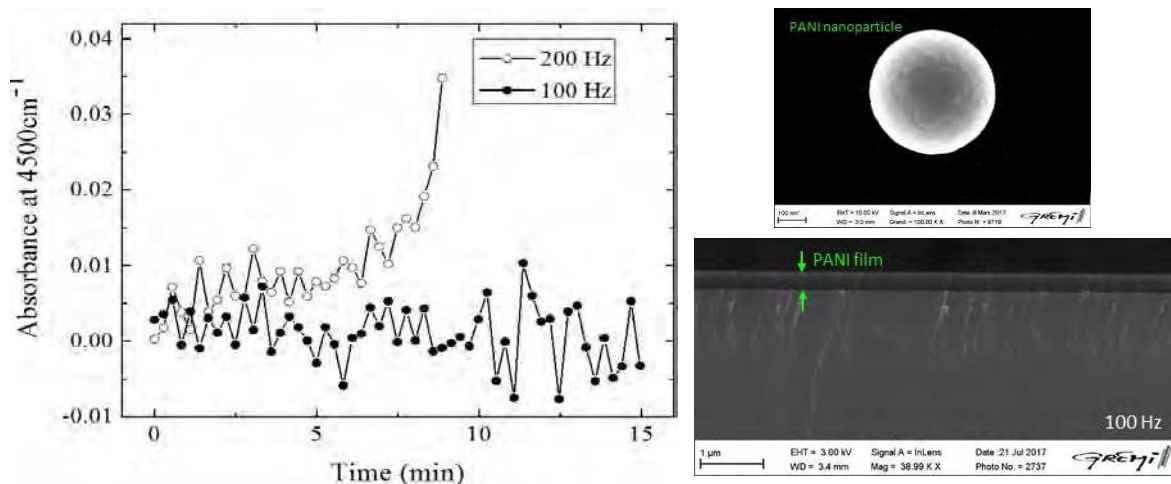


Figure II.59 – (a) Temporal behaviour of the IR absorbance at 4500 cm⁻¹ considering two discharges with different pulsing frequencies (100 Hz and 200 Hz) at 0.18 mbar, AR-ANI mixture 20-1 sccm and applied power of 5 W, without monomer vaporization while measuring. (b) SEM images of two different structures formed considering two different pulsed discharges (nanoparticle - pulsing frequency of 200Hz, PANI film – pulsing frequency of 100 Hz).

In Figure II.60(a) we can see SEM images of graphene before and after plasma polymerization. Analysing the SEM images graphene sheets were not damaged and their conformal coverage with PANI was successfully achieved. Moreover, to confirm this observation Raman spectra of graphene and graphene-PANI composite was collected (see Figure II.60(b)).

Both spectra show the three main features, D, G and 2 D peak at ~1333 cm⁻¹, ~1585 cm⁻¹, 2D and at ~ 2663 cm⁻¹, respectively, illustrating the conformal coverage of graphene with destroying the graphene sheets. Just a small decrease in the intensity ratio of the 2D to G peaks from 1.05 to 1.2, evidencing the presence of PANI over graphene.

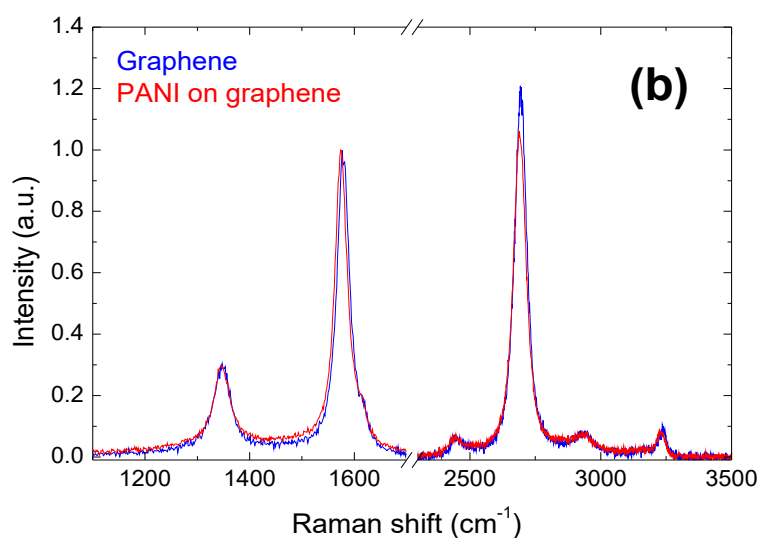
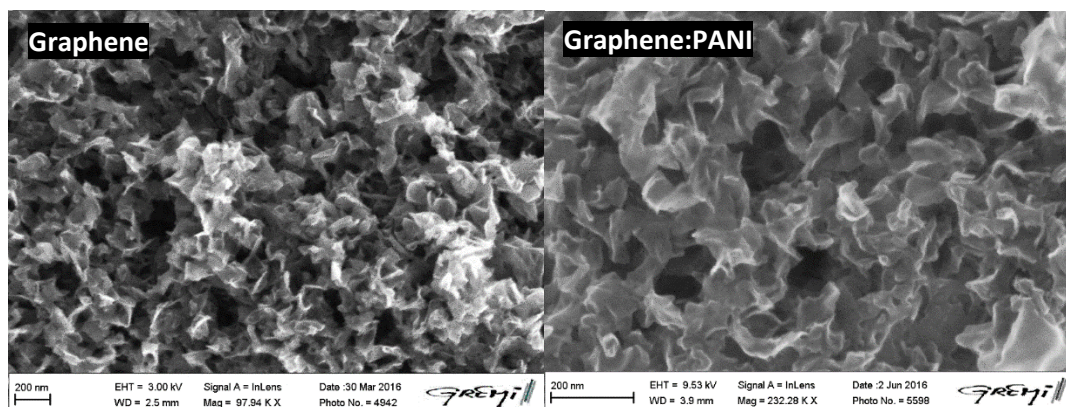


Figure II.60 – SEM images of graphene before and after plasma polymerization and respective Raman spectra. PANI plasma polymerization $P= 5W$, $f= 25$ Hz, $p= 0.18$ mbar, $Q_{Ar}= 20$ sccm and $Q_{ANI}=1$ sccm.

It was also important to perform XPS spectroscopy on the different graphene samples. The overview XPS spectra (see Figure II.61(a)) show the collected spectrum of graphene, PANI and graphene-PANI nanocomposite. A small trace of O 1s, around 1.2 at.%, was detected for the graphene sample. On the other hand, PANI and graphene-PANI spectra revealed three spectral lines at ~ 284.5 eV, ~ 398.9 eV and at ~ 531.5 eV, which correspond to C 1s, N 1s and O 1s, respectively. Since the penetration depth of XPS in this case is near 2.1 nm[273], these information concerns only PANI. The N 1s spectrum was deconvoluted into three peaks (see Figure II.61(b)). Two main peaks at binding energies of ~ 398.2 eV and ~ 399.4 eV, which are generally assigned to quinoid imine ($=N-$) and benzinoid amine ($-NH-$) structures, respectively. The presence of a third peak at a binding energy of 400.65 eV is most probably due to positively charged nitrogen (N^+).

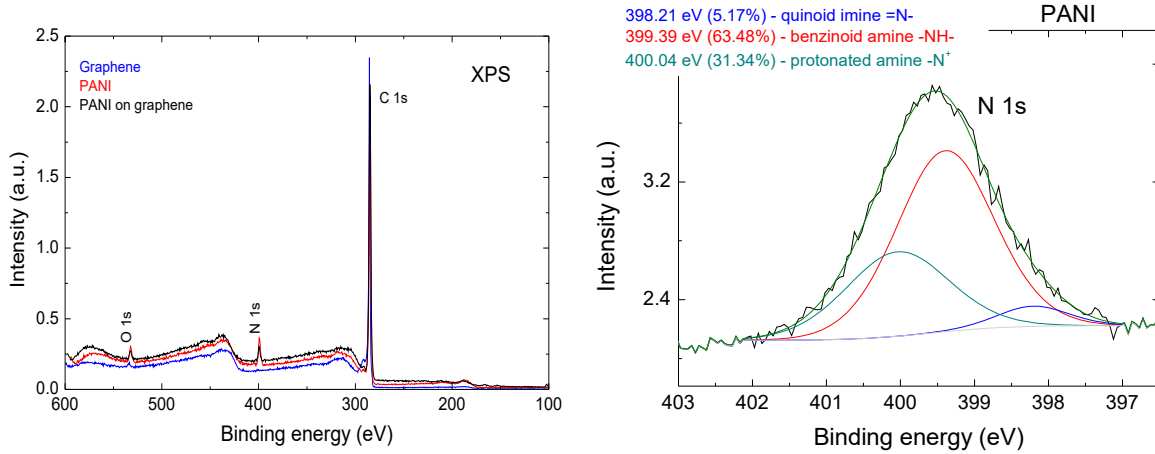


Figure II.61 – (a) XPS overview spectra of three different samples. Graphene, PANI and graphene-PANI. (b) N 1s deconvoluted spectrum of PANI.

II.3.2.1. Summary

This plasma-based method allowed to control polymerization process, avoiding nanoparticles formation. Manipulating plasma parameters, such as pulsing frequency (lower than 100 Hz), it was possible to induce thin film formation, which was the main propose of this work. SEM and Raman spectroscopy analysis also revealed a very interesting result, that a conformal coating of graphene was achieved for low frequency RF CCP. Further work must be done, namely electrical conductivity measurements and bench tests for FET biosensors as well as polymer doping trials in order to improve nanocomposites conductivity.

II.3.3. Graphene functionalization for biosensing applications

Since graphene sheets are hydrophobic, they have to be submitted to a nitrogen plasma treatment[275] in order to obtain a hydrophilic surface that enables for example adhesion of biomolecules. The same set up has been used for the plasma treatment only with some slightly changes. The nitrogen plasma treatment consists on placing the samples (dried graphene-methanol/distilled water suspension on SiO₂) in a remote zone of the capacitively coupled radiofrequency (RF) plasma for different processing times. A RF power of 8 W was applied, while maintaining 0.1 mbar pressure in the chamber, i.e. constant flow of N₂ (50 sccm). The samples were functionalized in a RF discharge at 13.56 MHz, where the circular stainless-steel electrodes have a diameter of 120 mm and a distance between them of 14 cm. The lower electrode is

grounded while the upper electrode is powered with 8 W. The background gas (50 sccm) was injected using a high-pressure cylinder ALPHAGAZ™ 1 from Air Liquide and controlled by a system of gas flow controllers (MKS).

After N₂ plasma treatment, contact angle measurements were performed, since it is one of the simplest diagnostics to demonstrate functionalization. Hydrophilic behaviour after functionalization is mostly due to addition of -OH (hydroxyl) and -COOH (carboxyl) hydrophilic groups to the graphene structure. Before functionalization graphene has a very strong hydrophobic behaviour, contact angle of ~147° (see Figure II.62 (a)), comparable with previously reported values.[279]

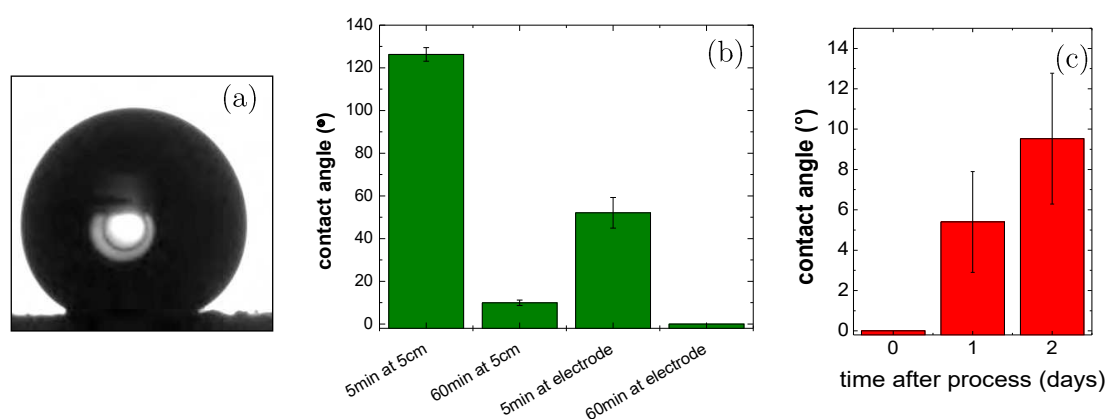


Figure II.62 - Contact angle measurements after N₂ plasma treatment. (a) contact angle image - distilled water droplet of >8μl of volume over dried graphene-methanol on SiO₂ sample, $\theta_c = 147.1^\circ \pm 6.7^\circ$. (b) Contact angle in function of plasma processing time and distance from plasma. (c) Contact angle evolution with sample aging, for the sample treated at the ground electrode for 60 min with N₂ CCP.

The best results were obtained for the situation where the samples were functionalized at the ground electrode for 60 min, where the contact angle was the lowest possible (~ 0°), see Figure II.62 (b). The aging of functionalized samples at the electrode for 60 min revealed impressive results, since the contact angle only changed 10°, hydrophilic behaviour remained the same (Figure II.62 (c)).

Moreover, Raman spectra showed an increase in the D/G intensities ratio, i.e. defect density, which in this case could not only be related with the edges but also point defects, such as vacancies, substitutional impurities or interstitial impurities.[280], [281] N₂ plasma treatment yields some structural imperfections and changes of the crystallinity, changing the electronic and vibrational properties of the material.

Meanwhile, the 2D to G peak intensities ratio decreased with the functionalization, which can imply a very small decrease in the crystallinity of the graphitic lattice, since the difference is not very significant as it is possible to see in Figure II.63. The quality of the graphene sheets remains almost intact, since the FWHM is $\sim 52\text{ cm}^{-1}$ and the 2D to G peak intensities ratio is around 1.1, indicating few-layer graphene.

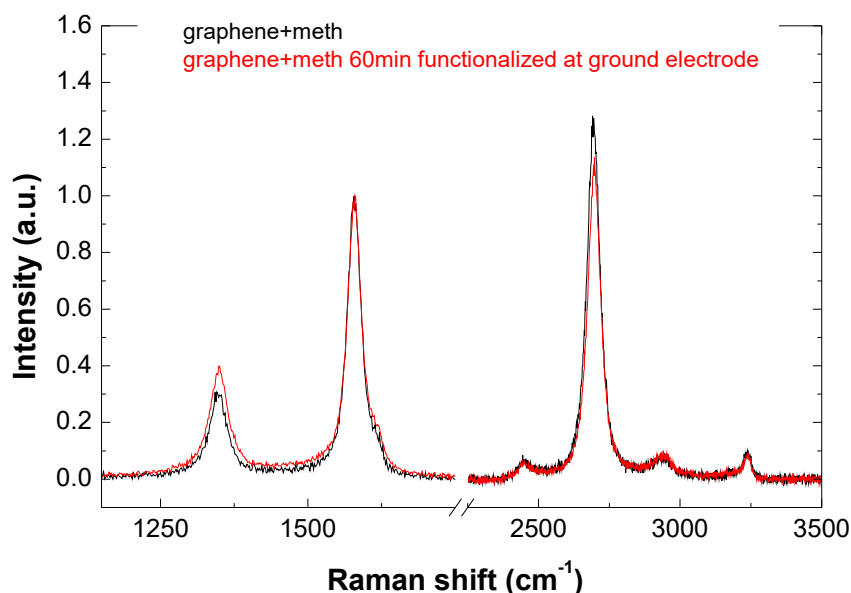


Figure II.63 - Raman spectra of (black line) graphene-methanol suspension on SiO₂ and (red line) functionalized graphene-methanol on SiO₂ at the ground electrode for 60 min

The incorporation of nitrogen into the graphene structure creates C–N bonds at the expense of the C–C bonds. Nevertheless, the C–N vibration modes, which should appear between the G and D bands, cannot be clearly identified due to the insensitivity of Raman excitation to distinguish between the cross sections of carbon and nitrogen atoms.

Therefore, XPS and NEXAFS analysis were performed on the samples to examine the local geometric and electronic structure of the incorporated species after deposition and functionalization.

XPS is a technique particularly useful in providing information on the chemistry of graphene and modified graphene structures, i.e. N-functionalized graphene. The effects of N₂ plasma functionalization were first evaluated from the evolution of elemental (C, N and O) concentrations determined from the XPS survey spectra analysis (see Table II-6). From the spectra, in Figure II.64, it is possible to conclude that after nitrogen plasma treatment of graphene

sheets, nitrogen is incorporated in the structure (nitrogen relative amount ~ 7.7 at%) and the oxygen presence also increases with the functionalization process. The relative amount of oxygen increases from ~ 4.6 to ~ 15.4 at%, which most probably is related with oxygen impurities that remain inside the chamber.

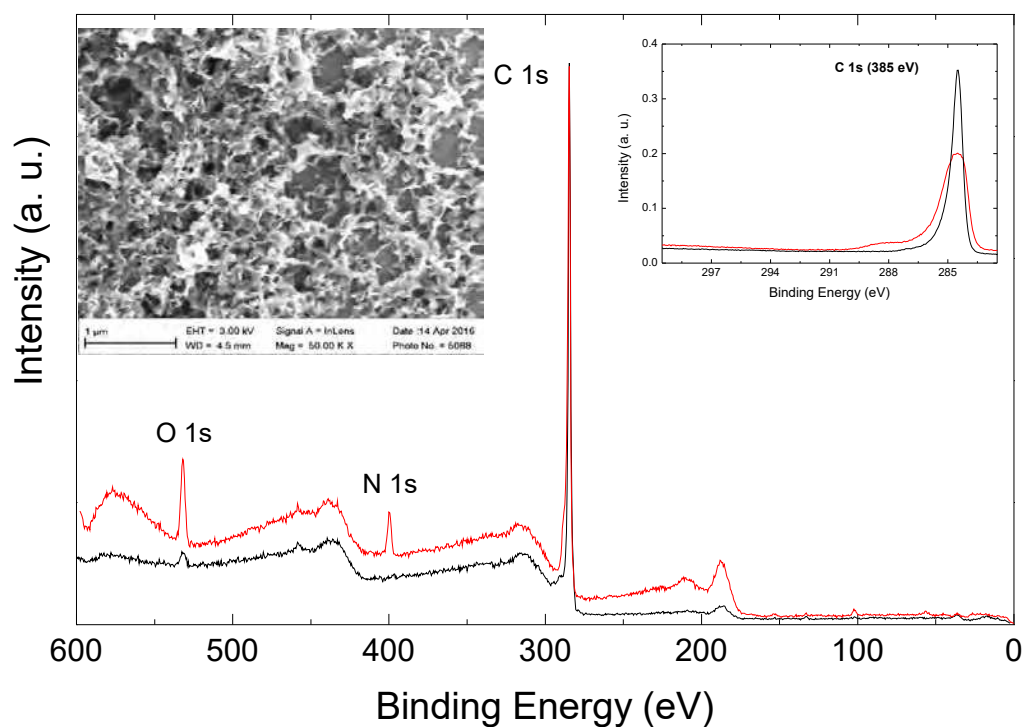


Figure II.64 - XPS spectra of (black line) graphene and (red line) N_2 plasma functionalized graphene for 60 minutes at ground electrode. (Inset) C_{1s} spectra of both graphene samples. (up left) SEM image of the N_2 plasma functionalized graphene.

Samples	C [at%]	O [at%]	N [at%]
Graphene	95.39	4.61	-
N-functionalized graphene	76.89	15.44	7.67

Table II-6 - Element concentrations obtained with the analysis of the XPS spectra of the functionalized and non-functionalized graphene samples.

In typical spectrum of graphene, the curve fitting of C 1s peak (see Figure II.65(a)) generally comprises three components (labelled C_1 , C_2 and C_3). Several different attributions can be found in the literature. For graphene, typically C_1 (~ 284.5 eV) is assigned to sp^2 C=C[282], C_2 (~ 285.1

eV) to sp^3 C-C/C-H[282] and C_3 (~286 eV) to bonds of carbon with oxygen groups (C-O, -C-OH, C-O-C≡, -OH).[226], [283], [284]

After functionalization C 1s photoelectron emission spectral line (see Figure II.65(b)), as expected, showed presence of N- and O-containing functional groups, confirming the wettability and Raman spectroscopy results. The fitting shows a successful functionalization of FSGs. Therefore, the C_4 peak appears at ~288.5 eV commonly assigned either to -C=N, -N=C-O-, COO-[272], [283], [284] and also other contribution is observed at ~284 eV (C_0) that usually is assigned to sp C.[226]

In Figure II.66 (c) the N 1s core level XPS spectrum was fitted and revealed three contributions, C_1 at ~398.8 eV corresponding to pyridinic N (N-6), C_2 at ~399.8 eV to pyrrolic N (N-5) and C_3 at ~400.9 eV to graphitic N (N-Q).[283] Both pyrrolic and pyridinic N contributions are predominant in N 1s spectrum.

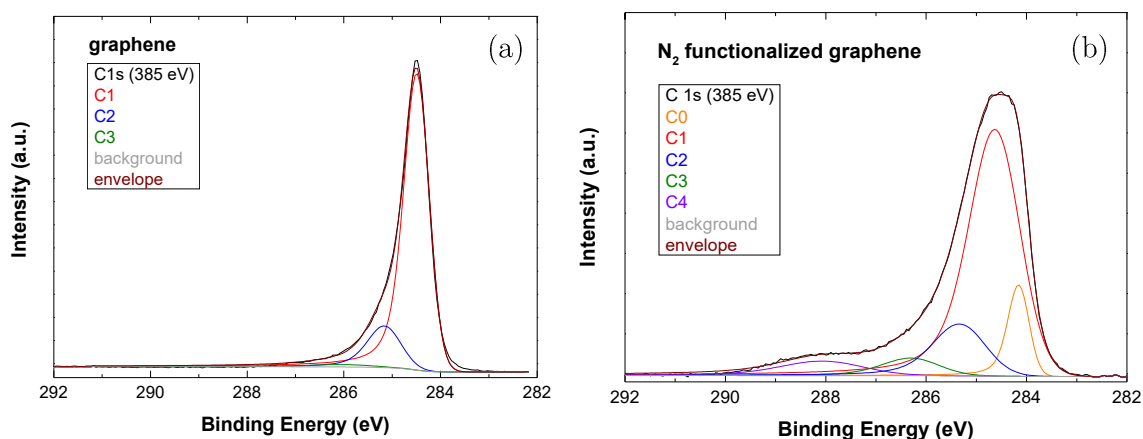


Figure II.65 - XPS C 1s photoelectron emission line spectra of (a) graphene and (b) N_2 plasma functionalized graphene. C 1s peak fitted with a Gaussian-Lorentzian product peak shape parameter set to 30 and Shirley background (CasaXPS software).

N_2 plasma treatment of graphitic structures can influence their NEXAFS signatures, can induce physical modification by creation of point and line defects, additional chemical modification by incorporation of N and O atoms on the graphene matrix. The hybridization of C atoms may change from sp^2 to sp^3 and also the chemical environment will be influenced, resulting in the observation of new spectral features in the NEXAFS spectra at ~288 eV (see Figure II.67(a)), in agreement with the observations in the C 1s spectra (Figure II.65(b)). This feature can be

assigned either to carboxylic ($-\text{C}=\text{O}$) coming from oxidation defects[285], to pyrrolic $\text{C}-\text{N}-\text{C}$ and pyridinic $-\text{C}\equiv\text{N}$ species.[286]

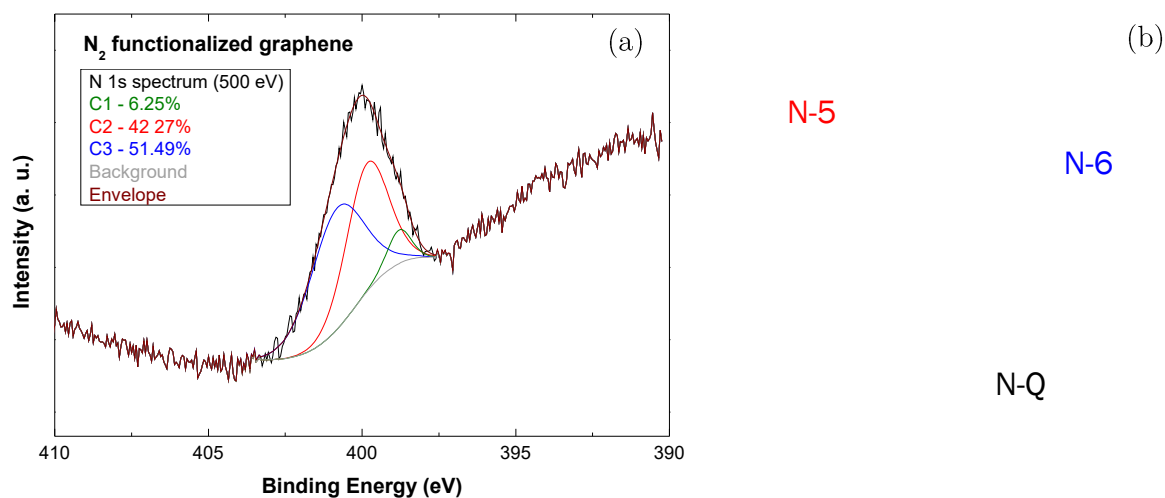


Figure II.66 - (a) XPS N 1s photoelectron emission line spectra of functionalized graphene and (b) Schematically presented nitrogen functional groups: pyridine N-6, pyrrolic N-5 and quaternary nitrogen N-Q. N 1s peak fitted with a Gaussian-Lorentzian product peak shape parameter set to 30 and Shirley background (CasaXPS software).

O K-edge NEXAFS spectra for pristine and N_2 plasma treated graphene are reproduced in Figure II.67(b). A significant increase of oxygenated functional groups after plasma treatment is observed. A sharp feature arises at ~ 532.1 eV, commonly assigned to the π^* state of $\text{C}=\text{O}$, which may be related to carbonyl groups bonded to an aromatic ring[287] or to $-\text{COOH}$ groups attached at the graphene oxide edge sites[288], [289]. This feature is more prominent for the N-functionalized graphene sample, which confirms the previous XPS results. At ~ 539.8 eV there is another broadened feature assigned to $\text{C}-\text{OH}$ σ^* states.[290]

N k-edge spectrum has a similar shape to the C k-edge, which indicates well succeeded incorporation of nitrogen atoms in the carbon sp^2 network.

At ~ 400 eV and ~ 408 eV in the NEXAFS spectrum (Figure II.67(c)) arise the $1s$ to π^* and σ^* transitions, respectively. The spectrum has a peak at ~ 398.7 eV that may correspond to $\text{C}=\text{N}$ imine, other at ~ 399.7 eV to heterocycles ($\text{C}-\text{N}=\text{C}$) and/or nitrile ($\text{C}\equiv\text{N}$) and another peak at ~ 400.8 eV that may related to amide, pyrrolic and/or amine nitrogen[291], which corroborates with the XPS results for the N-functionalized graphene.

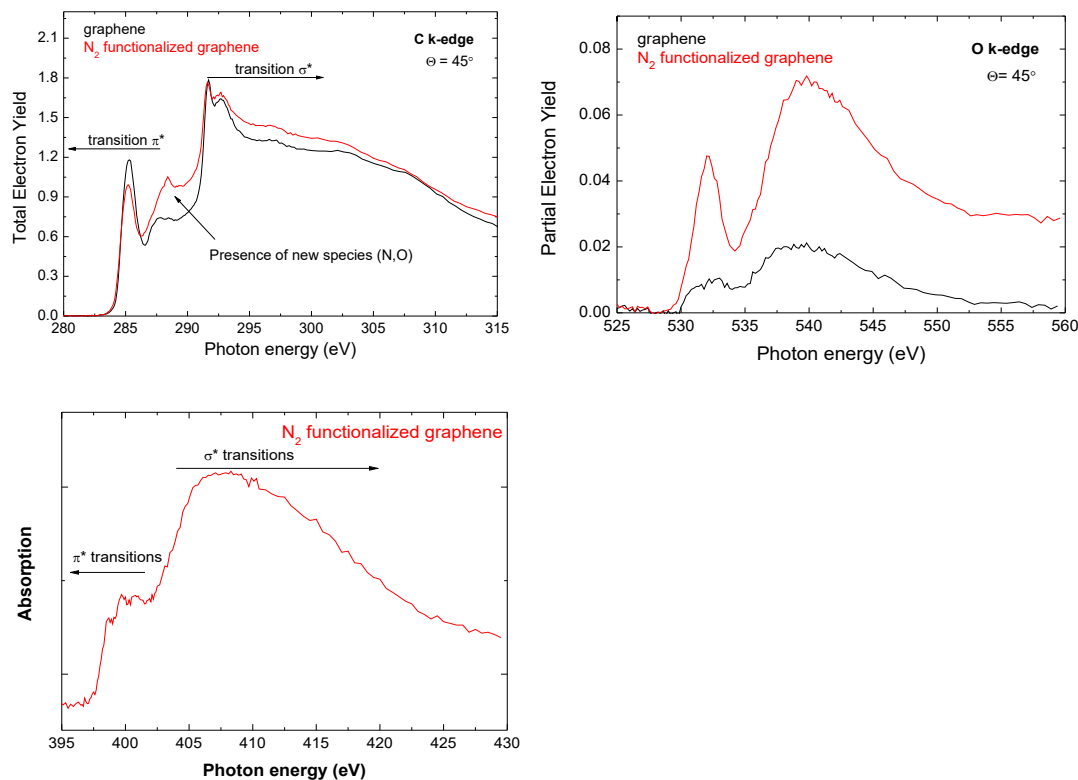


Figure II.67 – NEXAFS spectra of graphene and N_2 -functionalized graphene. (a) C k edge. (b) O k-edge (c) N k-edge

II.3.3.1. Summary

In conclusion, it was possible to demonstrate after graphene's functionalization the few-layered structure was conserved, only altering electronic and vibrational properties, as expected. Therefore, graphene functionalization was successfully achieved using a capacitively coupled N_2 plasma.

Contact angle measurements demonstrated that graphene, as a hydrophobic material, after N_2 plasma functionalization becomes hydrophilic, being the best results achieved for the plasma-treated samples at the ground electrode for 60 min.

XPS and NEXAFS results showed that no impurities were added after the deposition was performed. After N_2 plasma functionalization, sp^2/sp^3 decreases, and the relative amount of nitrogen and oxygen increase. Graphitic N is predominant in the N_2 plasma treated graphene samples, as the N 1s and N K-edge spectra demonstrate, showing that this RF plasma treatment gives preference to functionalization over doping.

Chapter III. Conclusions

This study allowed to prove that microwave plasma technologies can be used as a competitive and disruptive alternative route to produce different types of self-standing advanced carbon nanostructures.

- **Microwave plasma-based method used for 2D and 3D carbon nanostructures synthesis**
 - **Mass production of high-quality free-standing graphene and N-graphene sheets using an Argon-Ethanol microwave plasma**

Microwave-driven plasmas were successfully applied for the first time in the selective synthesis of high-quality graphene and N-graphene sheets via a single step process at atmospheric pressure. A high level of control over oxygen functionalities and sp^2/sp^3 carbons ratio (~ 15) has been achieved. For a randomly chosen samples, the percentage of counts of monolayers in all graphene sheets is about 40%. The method is rapid, highly cost-efficient and environmentally friendly, since it does not require the use of catalysts and noxious chemicals. It is also customizable and versatile, allowing the synthesis of different types of 2D nanostructures (e.g. N-graphene,) in the same reactor. Furthermore, the high energy density of the generated plasma environment allows the use of gaseous or liquid precursors. Moreover, self-organisation of the graphene sheets in respect to the supporting surface after mechanical treatment was observed.

The presented key enabling technology provides a rapid, single-step, cost-efficient and environmentally friendly method for selective synthesis of tailored graphene/N-graphene sheets at high yield and at atmospheric ambient. The main advantage of our approach is the achievement of a very high and extremely controllable energy density in the plasma reactor, which allows effective control over the energy and material fluxes towards growing nanostructures at the atomic level via proper reactor design and tailoring of the plasma environment in a synergistic way. The ability to control the amount and localization of energy and matter delivered

from the plasma to the developing nanostructures is the key to achieve the desired morphological, structural and functional properties of targeted materials.

Further scale-up along with better understanding of nucleation/growth processes in a multiphase environment will certainly lead to a substantial increase of the yield and a reduction of the production costs. Besides, mastering should be focused on reducing the multilayer (5–10 single layers) sheets percentage below 1%, controllable increasing of N-doping and optimization of collecting system for extraction of nanoparticles with dimensions less than 20 nm, i.e. graphene quantum dots. The use of large-scale configurations of wave-driven discharges paves the way for further scale-up and a higher level of customization. The exclusive plasma mechanisms that rule the distributions of energy and matter at atomic scale endow the method significant potential for the synthesis of other 2D materials (e.g. boron-doped graphene, hBN, etc). The method has also a potential for producing unique graphene-metal nanocomposites with well-designed nanoarchitecture. The expanding pool of prospect applications will most certainly continue to drive forward the research in this cutting-edge field.

Some studies have already started concerning investigation of other carbon-nitrogen-containing precursors, such as pyridine and methylamine, for direct synthesis of N-graphene, revealing very promising results, namely higher doping levels when using methylamine as precursor, approximately 5.4 at.%.

○ **Synthesis of complex carbon structures using different precursors**

Free-standing carbon nanostructures were produced by injecting different carbon precursors, i.e. CH₄ and CO₂, into a Ar microwave generated plasma environment. Selective synthesis of different carbon allotropes, i.e., few atomic layers graphene sheets and diamond-like nanostructures, is achieved by tailoring the plasma environment and thermodynamic conditions in the assembly zone of the reactor in a synergistic way. The ability to fine-tune the density and energy of the building units in the high energy-density plasma environment, which translates in an effective control over the energy and material fluxes towards growing nanostructures, constitutes this method's most crucial advantage. The method is also very adaptable, since different types of nanostructures can be synthesized using one and the same plasma reactor. The increase of the background gas flow and hydrogen decreases sp² carbons presence leading to 3D structures

formations, namely diamond-like structures, including hexagonal diamond (lonsdaleite), cubic diamond and n-diamond.

Additional work is required to relate the plasma specific properties and specific structural qualities of assembled nanostructures that, in turn, determine their electronic, mechanical, photonic properties, etc. The results about carbon precursor's flows will be further used as input data for mechanistic models to simulate the nucleation and growth processes of carbon nanostructures.

- **N-doping of graphene using a Ar-N₂ microwave remote plasma treatment**

N-graphene production was demonstrated using a microwave N₂-Ar plasma. Free standing graphene sheets were subjected to the remote region of the plasma for different exposure times and nitrogen concentrations in the N₂-Ar gas mixture at fixed applied power (Power =600 W), pressure (p=1 mbar) and total gas flow (Q_{TOTAL}= 50 sccm). Optical emission spectroscopy has been applied to monitor the nitrogen atoms, gas temperature and electron density at the graphene sheets' position. Raman and X-ray photoelectron spectroscopy (XPS) techniques have been applied to characterize the produced N-graphene, along with transmission electron microscopy (TEM) to study the morphology and structure of the samples.

The results demonstrate that the level of doping and type of functional groups attached to graphene scaffold can be controlled by changing both the exposure time to the plasma treatment, as well as the nitrogen percentage. The maximum level of nitrogen doping of graphene achieved was ~25 at.%.

Additionally, a short-term plasma treatment increased the sp²/sp³ area ratio, which is apparently related to both C-O bonds formation (at the expense of sp³ carbon) and N doping (which increases the amount of sp² carbon via formation of pyridine- and graphitic-like structures).

On the other hand, it was also possible to verify the influence of nitrogen content in N₂-Ar surface wave plasma treatment on the samples scaffold as well. Both TEM and Raman spectroscopy results revealed the graphene-like character of the samples is unchanged after plasma treatment and defects were added with the plasma processing to the graphene sheets. XPS analysis showed significant modifications in the graphene sheets structure, mostly at the sample surface, as the

nitrogen concentration in the gas mixture increases. The XPS results also revealed that the percentage of doping increased from 2.7 at.% to 25 at.% with the nitrogen concentration in the plasma gas. A doping level of around 12% was achieved without changing the few-layer graphene structure, for the concentration of N₂ of 30% in the plasma gas mixture, which is much higher than reported for arc-discharge plasma methods [267].

In addition, considering the case of 5 % of nitrogen in the N₂-Ar plasma gas, the nitrogen was incorporated in the graphene structure predominantly in the form of imide group and graphitic bonds (~70 %) and as N bound to sp³ carbon (~30 %). Moreover, the increase of the nitrogen content in the gas mixture was found to significantly contribute to the formation of new types of carbon-nitride structures. The effect of accelerated ions impinging the graphene surface should also be taken into consideration at these conditions.

Work is in progress to further clarify the plasma processes that are in play and to identify the carbon nitride structures.

- **Graphene applications using plasma-based methods**

- **Polymer-graphene nanocomposites using a plasma polymerization method**

In respect to the plasma polymerization method it was possible to control polymerization process, avoiding nanoparticles formation. Manipulating plasma parameters, such as pulsing frequency (lower than 100 Hz), inducing thin film formation, which was the main propose of this work. SEM and Raman spectroscopy analysis also revealed a very interesting result, that a conformal coating of graphene was achieved for low frequency RF CCP. Further work must be done, namely electrical conductivity measurements and bench tests for FET biosensors as well as polymer doping trials in order to improve nanocomposites conductivity.

- **Graphene functionalization for biosensing applications**

Concerning plasma functionalization with a capacitively coupled plasma, it was possible to demonstrate after graphene's functionalization the few-layered structure was conserved, only altering electronic and vibrational properties, as expected. Therefore, graphene functionalization was successfully achieved using a capacitively coupled N₂ plasma. Contact angle measurements

demonstrated that graphene, as a hydrophobic material, after N₂ plasma functionalization becomes hydrophilic, being the best results achieved for the plasma-treated samples at the ground electrode for 60 min. XPS and NEXAFS results showed that no impurities were added after the deposition method was performed. After N₂ plasma functionalization, sp²/sp³ decreases, and the relative amount of nitrogen and oxygen increase. N 1s and N K-edge spectra of N₂ plasma treated graphene samples demonstrate that Graphitic N is predominant, showing that this RF CC plasma method gives preference to functionalization over doping.

Part of the results shown in this PhD thesis were published in prestigious peer-reviewed journals as well as in two book chapters, and were presented in renowned conferences in the plasma physics and materials domains, including as Gaseous Electronics Conference (GEC), Europhysics Conference on Atomic and Molecular Physics of Ionized Gases (ESCAMPIG), International Conference on Phenomena in Ionized Gases (ICPIG), International microwave discharges workshop (MD), Symposium on Plasma Physics and Technology (SPPT) and European Physical Society (EPS) Conference on Plasma Physics.

References

- [1] M. Xu, T. Liang, M. Shi, and H. Chen, “Graphene-Like Two-Dimensional Materials,” *Chem. Rev.*, vol. 113, no. 5, pp. 3766–3798, May 2013.
- [2] Q. Wang, X. Wang, Z. Chai, and W. Hu, “Low-temperature plasma synthesis of carbon nanotubes and graphene based materials and their fuel cell applications,” *Chem. Soc. Rev.*, vol. 42, pp. 8821–8834, 2013.
- [3] A. Dias, “Microwave plasmas applied for graphene synthesis,” Universidade de Lisboa, 2013.
- [4] E. Tatarova *et al.*, “Microwave plasma based single step method for free standing graphene synthesis at atmospheric conditions,” *Appl. Phys. Lett.*, vol. 103, no. 13, 2013.
- [5] I. Levchenko, M. Keidar, S. Xu, H. Kersten, and K. (Ken) Ostrikov, “Low-temperature plasmas in carbon nanostructure synthesis,” *J. Vac. Sci. Technol. B, Nanotechnol. Microelectron. Mater. Process. Meas. Phenom.*, vol. 31, no. 5, p. 050801, Sep. 2013.
- [6] K. K. (Ken) K. Ostrikov, U. Cvelbar, and A. B. Murphy, “Plasma nanoscience: setting directions, tackling grand challenges,” *J. Phys. D Appl. Phys.*, vol. 44, no. 17, p. 174001, 2011.
- [7] A. K. Geim and K. S. Novoselov, “The rise of graphene,” *Nat. Mater.*, vol. 6, pp. 183–191, 2007.
- [8] H. Choi, S. Jung, J. Seo, D. W. Chang, L. Dai, and J.-B. Baek, “Graphene for energy conversion and storage in fuel cells and supercapacitors,” *Nano Energy*, vol. 1, no. 4, pp. 534–551, 2012.
- [9] N. Li, Z. Wang, K. Zhao, and Z. Shi, “Large scale synthesis of N-doped multi-layered graphene sheets by simple arc-discharge method,” *Carbon N. Y.*, vol. 48, no. 1, pp. 255–259, 2010.

- [10] J. C. Meyer, A. K. Geim, M. I. Katsnelson, K. S. Novoselov, T. J. Booth, and S. Roth, "The structure of suspended graphene sheets," *Nature*, vol. 446, no. 7131, pp. 60–63, Mar. 2007.
- [11] E. Tatarova, N. Bundaleska, J. P. Sarrette, and C. M. Ferreira, "Plasmas for environmental issues: from hydrogen production to 2D materials assembly," *Plasma Sources Sci. Technol.*, vol. 23, no. 6, p. 063002, Oct. 2014.
- [12] D. H. Seo, A. E. Rider, S. Kumar, L. K. Randeniya, and K. Ostrikov, "Vertical graphene gas- and bio-sensors via catalyst-free, reactive plasma reforming of natural honey," *Carbon N. Y.*, vol. 60, pp. 221–228, Aug. 2013.
- [13] I. Levchenko, O. Volotskova, A. Shashurin, Y. Raitses, K. Ostrikov, and M. Keidar, "The large-scale production of graphene flakes using magnetically-enhanced arc discharge between carbon electrodes," *Carbon N. Y.*, vol. 48, no. 15, pp. 4570–4574, Dec. 2010.
- [14] Y. Lin, C. Lin, P. Chiu, Y. Lin, C. Lin, and P. Chiu, "Controllable graphene N-doping with ammonia plasma," *Appl. Phys. Lett.*, vol. 96, no. 133110, pp. 1–3, 2010.
- [15] Y. Shao *et al.*, "Nitrogen-doped graphene and its electrochemical applications," *J. Mater. Chem.*, vol. 20, no. 35, p. 7491, Aug. 2010.
- [16] X. Wang *et al.*, "N-doping of graphene through electrothermal reactions with ammonia.," *Science*, vol. 324, no. 5928, pp. 768–71, May 2009.
- [17] X. Li, H. Wang, J. T. Robinson, H. Sanchez, G. Diankov, and H. Dai, "Simultaneous Nitrogen Doping and Reduction of Graphene Oxide," *J. Am. Chem. Soc.*, vol. 131, no. 43, pp. 15939–15944, Nov. 2009.
- [18] L. Qu, Y. Liu, J.-B. Baek, and L. Dai, "Nitrogen-Doped Graphene as Efficient Metal-Free Electrocatalyst for Oxygen Reduction in Fuel Cells," *ACS Nano*, vol. 4, no. 3, pp. 1321–1326, Mar. 2010.
- [19] Y. Wang, Y. Shao, D. W. Matson, J. Li, and Y. Lin, "Nitrogen-Doped Graphene

- and Its Application in Electrochemical Biosensing,” *ACS Nano*, vol. 4, no. 4, pp. 1790–1798, Apr. 2010.
- [20] W. Yang *et al.*, “Nitrogen plasma modified CVD grown graphene as counter electrodes for bifacial dye-sensitized solar cells,” *Electrochim. Acta*, vol. 173, pp. 715–720, Aug. 2015.
- [21] D. R. Cooper *et al.*, “Experimental review of graphene,” *ISRN Condens. Matter Phys.*, vol. 2012, no. 501686, pp. 1–56, 2012.
- [22] K. Hu, D. D. Kulkarni, I. Choi, and V. V. Tsukruk, “Graphene-polymer nanocomposites for structural and functional applications.pdf,” *Prog. Polym. Sci.*, vol. 39, pp. 1934–1972, 2014.
- [23] E. Tatarova *et al.*, “Microwave plasmas applied for the synthesis of free standing graphene sheets,” *J. Phys. D. Appl. Phys.*, vol. 47, no. 38, 2014.
- [24] T. Kuila, S. Bose, P. Khanra, A. K. Mishra, N. H. Kim, and J. H. Lee, “Recent advances in graphene-based biosensors,” *Biosens. Bioelectron.*, vol. 26, no. 12, pp. 4637–4648, 2011.
- [25] S. Viswanathan *et al.*, “Graphene-protein field effect biosensors: Glucose sensing,” *Mater. Today*, vol. 18, no. 9, pp. 513–522, 2015.
- [26] Y. Su, V. G. Kravets, S. L. Wong, J. Waters, A. K. Geim, and R. R. Nair, “Impermeable barrier films and protective coatings based on reduced graphene oxide,” *Nat. Commun.*, vol. 5, p. 4843, 2014.
- [27] J. Ren *et al.*, “Environmentally-friendly conductive cotton fabric as flexible strain sensor based on hot press reduced graphene oxide,” *Carbon N. Y.*, vol. 111, pp. 622–630, 2017.
- [28] O. A. Shenderova and D. M. Gruen, *Ultrananocrystalline diamond: synthesis, properties and applications*. William Andrew, 2012.
- [29] H. Terrones and A. L. Mackay, “From C60 to negatively curved graphite,” *Prog. Cryst. Growth Charact. Mater.*, vol. 34, no. 1–4, pp. 25–36, Jan. 1997.

- [30] A. V. Rode, S. T. Hyde, E. G. Gamaly, R. G. Elliman, D. R. McKenzie, and S. Bulcock, “Structural analysis of a carbon foam formed by high pulse-rate laser ablation,” *Appl. Phys. A Mater. Sci. Process.*, vol. 69, no. 7, pp. S755–S758, Dec. 1999.
- [31] G. Benedek, E. Galvani, S. Sanguinetti, and S. Serra, “Hallow diamonds: stability and elastic properties,” *Chem. Phys. Lett.*, vol. 244, no. 5–6, pp. 339–344, Oct. 1995.
- [32] C. W. J. Beenakker, “Colloquium: Andreev reflection and Klein tunneling in graphene,” *Rev. Mod. Phys.*, vol. 80, no. 4, p. 1337, 2008.
- [33] K. S. Novoselov *et al.*, “Two-Dimensional Gas of Massless Dirac Fermions in Graphene K.S.,” *Nature*, vol. 438, pp. 197–200, 2005.
- [34] Y. Zhang, Y. Tan, H. L. Stormer, and P. Kim, “Experimental Observation of Quantum Hall Effect and Berry’s Phase in Graphene,” *Nature*, vol. 438, no. November, pp. 201–204, 2005.
- [35] M. I. Katsnelson, K. S. Novoselov, and A. A. K. Geim, “Chiral tunnelling and the Klein paradox in graphene,” 2006.
- [36] N. Stander and B. Huard, “Evidence for Klein Tunneling in Graphene p - n Junctions,” *Phys. Rev. Lett.*, vol. 026807, pp. 1–4, 2009.
- [37] A. Rycerz, J. Tworzydło, and C. W. J. Beenakker, “Valley filter and valley valve in graphene,” Aug. 2006.
- [38] K. Ziegler, “Minimal conductivity of graphene: Nonuniversal values from the Kubo formula,” *Phys. Rev. B*, vol. 75, no. 233407, pp. 1–4, 2007.
- [39] E. Mccann, K. Kechedzhi, V. I. Fal, H. Suzuura, T. Ando, and B. L. Altshuler, “Weak-Localization Magnetoresistance and Valley Symmetry in Graphene,” *Phys. Rev. Lett.*, vol. 97, no. 146805, pp. 1–4, 2006.
- [40] M. Orlita *et al.*, “Approaching the Dirac Point in High-Mobility Multilayer Epitaxial Graphene,” *Phys. Rev. Lett.*, vol. 101, no. 26, p. 267601, Dec. 2008.

- [41] C. W. J. Beenakker, “Specular Andreev Reflection in Graphene,” *Phys. Rev. Lett.*, vol. 97, no. 6, p. 067007, Aug. 2006.
- [42] X. Du, I. Skachko, A. Barker, and E. Y. Andrei, “Approaching ballistic transport in suspended graphene,” *Nat. Nanotechnol.*, vol. 3, no. 8, pp. 491–495, Aug. 2008.
- [43] G. W. Semenoff, “Condensed-Matter Simulation of a Three-Dimensional Anomaly,” *Phys. Rev. Lett.*, vol. 53, no. 26, pp. 2449–2452, Dec. 1984.
- [44] V. P. Gusynin and S. G. Sharapov, “Unconventional Integer Quantum Hall Effect in Graphene,” *Phys. Rev. Lett.*, vol. 95, no. 14, p. 146801, Sep. 2005.
- [45] Y. H. Wu, T. Yu, and Z. X. Shen, “Two-dimensional carbon nanostructures: Fundamental properties, synthesis, characterization, and potential applications,” *J. Appl. Phys. Appl.*, vol. 108, no. 071301, pp. 1–38, 2010.
- [46] K. Nakada, M. Fujita, G. Dresselhaus, and M. S. Dresselhaus, “Edge state in graphene ribbons: Nanometer size effect and edge shape dependence,” *Phys. Rev. B*, vol. 54, no. 24, pp. 17954–17961, Dec. 1996.
- [47] M. Ezawa, “Peculiar width dependence of the electronic properties of carbon nanoribbons,” *Phys. Rev. B*, vol. 73, no. 4, p. 045432, Jan. 2006.
- [48] L. Brey and H. A. Fertig, “Electronic states of graphene nanoribbons studied with the Dirac equation,” *Phys. Rev. B*, vol. 73, no. 23, p. 235411, Jun. 2006.
- [49] K.-I. Sasaki, S. Murakami, and R. Saito, “Gauge Field for Edge State in Graphene,” 2006.
- [50] Y.-W. Son, M. L. Cohen, and S. G. Louie, “Energy Gaps in Graphene Nanoribbons,” *Phys. Rev. Lett.*, vol. 97, no. 21, p. 216803, Nov. 2006.
- [51] L. Yang, C.-H. Park, Y.-W. Son, M. L. Cohen, and S. G. Louie, “Quasiparticle Energies and Band Gaps in Graphene Nanoribbons,” *Phys. Rev. Lett.*, vol. 99, no. 18, p. 186801, Nov. 2007.
- [52] Y. Imry, *Introduction to mesoscopic physics*. Oxford University Press, 2009.
- [53] V. F. GANTMAKHER, *THE INTERNATIONAL SERIES OF MONOGRAPHS*

ON PHYSICS SERIES EDITORS. Oxford: Oxford University Press, 2005.

- [54] H. Suzuura and T. Ando, “Crossover from Symplectic to Orthogonal Class in a Two-Dimensional Honeycomb Lattice,” *Phys. Rev. Lett.*, vol. 89, no. 26, p. 266603, Dec. 2002.
- [55] A. F. Morpurgo and F. Guinea, “Intervalley Scattering, Long-Range Disorder, and Effective Time-Reversal Symmetry Breaking in Graphene,” *Phys. Rev. Lett.*, vol. 97, no. 19, p. 196804, Nov. 2006.
- [56] T. Ando, T. Nakanishi, and R. Saito, “Berry’s Phase and Absence of Back Scattering in Carbon Nanotubes,” *J. Phys. Soc. Japan*, vol. 67, no. 8, pp. 2857–2862, Aug. 1998.
- [57] F. V. Tikhonenko, A. A. Kozikov, A. K. Savchenko, and R. V. Gorbachev, “Transition between Electron Localization and Antilocalization in Graphene,” *Phys. Rev. Lett.*, vol. 103, no. 22, p. 226801, Nov. 2009.
- [58] X.-Z. Yan and C. S. Ting, “Weak Localization of Dirac Fermions in Graphene,” *Phys. Rev. Lett.*, vol. 101, no. 12, p. 126801, Sep. 2008.
- [59] S. V. Morozov *et al.*, “Strong Suppression of Weak Localization in Graphene,” *Phys. Rev. Lett.*, vol. 97, no. 1, p. 016801, Jul. 2006.
- [60] F. Miao, S. Wijeratne, Y. Zhang, U. C. Coskun, W. Bao, and C. N. Lau, “Phase-coherent transport in graphene quantum billiards,” *Science*, vol. 317, no. 5844, pp. 1530–3, Sep. 2007.
- [61] J. Tworzydło, B. Trauzettel, M. Titov, A. Rycerz, and C. W. J. Beenakker, “Sub-Poissonian Shot Noise in Graphene,” *Phys. Rev. Lett.*, vol. 96, no. 24, p. 246802, Jun. 2006.
- [62] S. Adam, E. H. Hwang, V. M. Galitski, and S. Das Sarma, “A self-consistent theory for graphene transport,” *Proc. Natl. Acad. Sci. U. S. A.*, vol. 104, no. 47, pp. 18392–7, Nov. 2007.
- [63] J.-H. Chen, C. Jang, S. Adam, M. S. Fuhrer, E. D. Williams, and M. Ishigami,

- “Charged-impurity scattering in graphene,” *Nat. Phys.*, vol. 4, no. 5, pp. 377–381, May 2008.
- [64] P. M. Ostrovsky, I. V. Gornyi, and A. D. Mirlin, “Electron transport in disordered graphene,” *Phys. Rev. B*, vol. 74, no. 23, p. 235443, Dec. 2006.
- [65] K. I. Bolotin *et al.*, “Ultrahigh electron mobility in suspended graphene,” *Solid State Commun.*, vol. 146, no. 9–10, pp. 351–355, Jun. 2008.
- [66] K. I. Bolotin, K. J. Sikes, J. Hone, H. L. Stormer, and P. Kim, “Temperature-Dependent Transport in Suspended Graphene,” *Phys. Rev. Lett.*, vol. 101, no. 096802, 2008.
- [67] T. Stauber, N. M. R. Peres, and A. H. Castro Neto, “Conductivity of suspended and non-suspended graphene at finite gate voltage,” *Phys. Rev. B*, vol. 78, no. 8, p. 085418, Aug. 2008.
- [68] Z. H. Ni *et al.*, “Probing Charged Impurities in Suspended Graphene Using Raman Spectroscopy,” *ACS Nano*, vol. 3, no. 3, pp. 569–574, 2009.
- [69] A. Zurutuza and C. Marinelli, “Challenges and opportunities in graphene commercialization,” *Nat. Nanotechnol.* 2014 910, Oct. 2014.
- [70] N. Mishra, J. Boeckl, N. Motta, and F. Iacopi, “Graphene growth on silicon carbide: A review,” *Phys. Status Solidi*, vol. 213, no. 9, pp. 2277–2289, Sep. 2016.
- [71] S. Stankovich *et al.*, “Synthesis of graphene-based nanosheets via chemical reduction of exfoliated graphite oxide,” *Carbon N. Y.*, vol. 45, pp. 1558–1565, 2007.
- [72] Y. Hernandez *et al.*, “High yield production of graphene by liquid phase exfoliation of graphite,” May 2008.
- [73] W. Gannett, W. Regan, K. Watanabe, T. Taniguchi, M. F. Crommie, and A. Zettl, “Boron nitride substrates for high mobility chemical vapor deposited graphene,” *Appl. Phys. Lett.*, vol. 98, no. 24, p. 242105, Jun. 2011.
- [74] A. Reina *et al.*, “Large Area, Few-Layer Graphene Films on Arbitrary Substrates by Chemical Vapor Deposition,” *Nano Lett.*, vol. 9, no. 1, pp. 30–35, Jan. 2009.

- [75] N. Zhan, M. Olmedo, G. Wang, and J. Liu, “Layer-by-layer synthesis of large-area graphene films by thermal cracker enhanced gas source molecular beam epitaxy,” *Carbon N. Y.*, vol. 49, no. 6, pp. 2046–2052, May 2011.
- [76] N. Zhan, G. Wang, and J. Liu, “Cobalt-assisted large-area epitaxial graphene growth in thermal cracker enhanced gas source molecular beam epitaxy,” *Appl Phys A*, vol. 105, pp. 341–345, 2011.
- [77] G. Jo, M. Choe, S. Lee, W. Park, Y. H. Kahng, and T. Lee, “The application of graphene as electrodes in electrical and optical devices,” *Nanotechnology*, vol. 23, no. 11, p. 112001, Mar. 2012.
- [78] X. Wang, G. Sun, P. Routh, D.-H. Kim, W. Huang, and P. Chen, “Heteroatom-doped graphene materials: syntheses, properties and applications,” *Chem. Soc. Rev.*, vol. 43, no. 20, pp. 7067–7098, Sep. 2014.
- [79] D. Han Seo, S. Pineda, S. Yick, J. Bell, Z. Jun Han, and K. Ostrikov, “Plasma-enabled sustainable elemental lifecycles: honeycomb-derived graphenes for next-generation biosensors and supercapacitors,” *Green Chem.*, vol. 17, 2015.
- [80] J. Ma, A. Michaelides, and D. Alfè, “Binding of hydrogen on benzene, coronene, and graphene from quantum Monte Carlo calculations,” *J. Chem. Phys.*, vol. 134, no. 13, p. 134701, Apr. 2011.
- [81] J. J. Wang *et al.*, “Free-standing subnanometer graphite sheets,” *Appl. Phys. Lett.*, vol. 85, no. 7, pp. 1265–1267, Aug. 2004.
- [82] K. Kobayashi *et al.*, “Nanographite domains in carbon nanowalls,” *J. Appl. Phys.*, vol. 101, no. 9, p. 094306, May 2007.
- [83] A. T. H. Chuang, J. Robertson, B. O. Boskovic, and K. K. K. Koziol, “Three-dimensional carbon nanowall structures,” *Appl. Phys. Lett.*, vol. 90, no. 12, p. 123107, Mar. 2007.
- [84] A. T. H. Chuang, B. O. Boskovic, and J. Robertson, “Freestanding carbon nanowalls by microwave plasma-enhanced chemical vapour deposition,” *Diam.*

- Relat. Mater.*, vol. 15, no. 4–8, pp. 1103–1106, Apr. 2006.
- [85] M. Li, D. Liu, D. Wei, X. Song, D. Wei, and A. T. S. Wee, “Controllable Synthesis of Graphene by Plasma-Enhanced Chemical Vapor Deposition and Its Related Applications,” *Adv. Sci.*, vol. 3, no. 11, p. 1600003, Nov. 2016.
- [86] J. Zhu, D. Yang, Z. Yin, Q. Yan, and H. Zhang, “Graphene and Graphene-Based Materials for Energy Storage Applications,” *Small*, vol. 10, no. 17, pp. 3480–3498, Sep. 2014.
- [87] Q. Ke and J. Wang, “Graphene-based materials for supercapacitor electrodes – A review,” *J. Mater.*, vol. 2, no. 1, pp. 37–54, Mar. 2016.
- [88] A. Dato, V. Radmilovic, Z. Lee, J. Phillips, and M. Frenklach, “Substrate-Free Gas-Phase Synthesis of Graphene Sheets 2008,” *Nano Lett.*, vol. 8, no. 7, pp. 2012–2016, 2008.
- [89] A. Dato and M. Frenklach, “Substrate-free microwave synthesis of graphene: experimental conditions and hydrocarbon precursors,” *New J. Phys.*, vol. 12, no. 125013, pp. 1–24, 2010.
- [90] I. M. MacKinnon and B. G. Reuben, “The Synthesis of Boron Carbide in an RF Plasma,” *J. Electrochem. Soc.*, vol. 122, no. 6, p. 806, Jun. 1975.
- [91] J. Phillips, C. C. Luhrs, and M. Richard, “Review : Engineering Particles Using the Aerosol-Through-Plasma Method,” *IEEE Trans. Plasma Sci.*, vol. 37, no. 6, pp. 726–739, 2009.
- [92] T. N. Lambert, C. C. Luhrs, C. A. Chavez, S. Wakeland, M. T. Brumbach, and T. M. Alam, “Graphite oxide as a precursor for the synthesis of disordered graphenes using the aerosol-through-plasma method,” *Carbon N. Y.*, vol. 48, no. 14, pp. 4081–4089, Nov. 2010.
- [93] E. Tatarova *et al.*, “Microwave Plasmas Applied for Synthesis of Free-Standing Carbon Nanostructures at Atmospheric Pressure Conditions,” in *Atmospheric Pressure Plasmas: Processes, Technology and Applications*, Nova Science

- Publishers, 2016.
- [94] Q. Wang, X. Wang, Z. Chai, and W. Hu, “Low-temperature plasma synthesis of carbon nanotubes and graphene based materials and their fuel cell applications,” *Chem. Soc. Rev.*, vol. 42, no. 23, p. 8821, Nov. 2013.
- [95] C. P. Ewels and M. Glerup, “Nitrogen Doping in Carbon Nanotubes,” *J. Nanosci. Nanotechnol.*, vol. 5, no. 9, pp. 1345–1363, Sep. 2005.
- [96] H. M. Jeong *et al.*, “Nitrogen-Doped Graphene for High-Performance Ultracapacitors and the Importance of Nitrogen-Doped Sites at Basal Planes,” *Nano Lett.*, vol. 11, no. 6, pp. 2472–2477, Jun. 2011.
- [97] T.-Z. Hou, H.-J. Peng, J.-Q. Huang, Q. Zhang, and B. Li, “The formation of strong-couple interactions between nitrogen-doped graphene and sulfur/lithium (poly)sulfides in lithium-sulfur batteries,” *2D Mater.*, vol. 2, no. 1, p. 014011, Mar. 2015.
- [98] Y. Zhao, Y. Zhang, Z. Bakenova, and Z. Bakenov, “Carbon/Sulfur Composite Cathodes for Flexible Lithium/Sulfur Batteries: Status and Prospects,” *Front. Energy Res.*, vol. 3, p. 2, Feb. 2015.
- [99] T.-Z. Hou, H.-J. Peng, J.-Q. Huang, Q. Zhang, and B. Li, “The formation of strong-couple interactions between nitrogen-doped graphene and sulfur/lithium (poly)sulfides in lithium-sulfur batteries,” *2D Mater.*, vol. 2, no. 1, p. 014011, Mar. 2015.
- [100] R. Yadav and C. K. Dixit, “Synthesis, characterization and prospective applications of nitrogen-doped graphene: A short review,” *J. Sci. Adv. Mater. Devices*, vol. 2, no. 2, pp. 141–149, Jun. 2017.
- [101] † Jordi Casanovas, † Josep Manel Ricart, ‡ Jaime Rubio, *, ‡ and Francesc Illas, and J. M. Jiménez-Mateos§, “Origin of the Large N 1s Binding Energy in X-ray Photoelectron Spectra of Calcined Carbonaceous Materials,” 1996.
- [102] F. M. Hassan, V. Chabot, J. Li, B. K. Kim, and L. Ricardez-sandoval, “Pyrrolic-

- structure enriched nitrogen doped graphene for highly efficient next generation supercapacitors,” *J. Mater. Chem. A*, vol. 1, pp. 2904–2912, 2013.
- [103] S. Kundu *et al.*, “Electrocatalytic Activity and Stability of Nitrogen-Containing Carbon Nanotubes in the Oxygen Reduction Reaction,” *J. Phys. Chem. C*, vol. 113, no. 32, pp. 14302–14310, Aug. 2009.
- [104] M. Aliofkhazraei, N. Ali, W. I. Milne, C. S. Ozkan, S. Mitura, and J. L. Gervasoni, Eds., *GRAPHENE SCIENCE HANDBOOK: Nanostructure and Atomic Arrangement*. CRC Press, 2016.
- [105] K. Ostrikov, E. C. Neyts, and M. Meyyappan, “Plasma nanoscience: from nanosolids in plasmas to nano-plasmas in solids,” *Adv. Phys.*, vol. 62, no. 2, pp. 113–224, Apr. 2013.
- [106] K. Ostrikov, E. C. Neyts, and M. Meyyappan, “Plasma nanoscience: from nanosolids in plasmas to nano-plasmas in solids,” *Adv. Phys.*, vol. 62, no. 2, pp. 113–224, Apr. 2013.
- [107] A. Dias *et al.*, “Production of N-graphene by microwave N₂-Ar plasma,” *J. Phys. D. Appl. Phys.*, vol. 49, no. 5, p. 55307, 2016.
- [108] J.-Y. Raty, G. Galli, C. Bostedt, T. van Buuren, and L. Terminello, “Quantum Confinement and Fullerenelike Surface Reconstructions in Nanodiamonds,” *Phys. Rev. Lett.*, vol. 90, no. 3, p. 037401, Jan. 2003.
- [109] A. V. Okotrub, L. G. Bulusheva, V. L. Kuznetsov, A. V. Gusel’nikov, and A. L. Chuvilin, “Electronic state of nanodiamond/graphite interfaces,” *Eur. Phys. J. D*, vol. 34, no. 1–3, p. 157, 2005.
- [110] Y. Lifshitz *et al.*, “Nanostructure: Epitaxial diamond polytypes on silicon,” *Nature*, vol. 412, no. 6845, pp. 404–404, Jul. 2001.
- [111] N. Dubrovinskaia, L. Dubrovinsky, and F. Langenhorst, “Synthesis of nanocrystalline diamond and 6H diamond polytype,” in *Large Meteorite Impacts*, 2003, p. 4065.

- [112] R. Kapil, B. R. Mehta, and V. D. Vankar, "Growth of 8H polytype of diamond using cyclic growth/etch oxy-acetylene flame setup," *Thin Solid Films*, vol. 312, no. 1-2, pp. 106-110, Jan. 1998.
- [113] R. Kapil, B. R. Mehta, and V. D. Vankar, "Synthesis of 15R polytype of diamond in oxy-acetylene flame grown diamond thin films," *Appl. Phys. Lett.*, vol. 68, no. 18, p. 2520, Aug. 1998.
- [114] S. Welz, Y. Gogotsi, and M. J. McNallan, "Nucleation, growth, and graphitization of diamond nanocrystals during chlorination of carbides.," *Phys., J. Appl.*, vol. 93, pp. 4207-4214, 2003.
- [115] J. . Wang, C. . Zhang, X. . Zhong, and G. . Yang, "Cubic and hexagonal structures of diamond nanocrystals formed upon pulsed laser induced liquid-solid interfacial reaction," *Chem. Phys. Lett.*, vol. 361, no. 1-2, pp. 86-90, Jul. 2002.
- [116] J. L. Peng, J. O. Orwa, B. Jiang, S. Praver, and L. A. Bursill, "Nano-crystals of c-diamond, n-diamond and i-carbon grown in carbon-ion implanted fused quartz," *Int. J. Mod. Phys. B*, vol. 15, no. 23, pp. 3107-3123, Sep. 2001.
- [117] M. Rossi, G. Vitali, M. L. Terranova, and V. Sessa, "Experimental evidence of different crystalline forms in chemical vapor deposited diamond films," *Appl. Phys. Lett.*, vol. 63, no. 20, pp. 2765-2767, Nov. 1993.
- [118] H. Shiomi, "Reactive Ion Etching of Diamond in O_2 and CF_4 Plasma, and Fabrication of Porous Diamond for Field Emitter Cathodes," *Jpn. J. Appl. Phys.*, vol. 36, no. Part 1, No. 12B, pp. 7745-7748, Dec. 1997.
- [119] E.-S. Baik, Y.-J. Baik, and D. Jeon, "Aligned Diamond Nanowhiskers," *J. Mater. Res.*, vol. 15, no. 04, pp. 923-926, Apr. 2000.
- [120] W. J. Zhang *et al.*, "Structuring nanodiamond cone arrays for improved field emission," *Appl. Phys. Lett.*, vol. 83, no. 16, pp. 3365-3367, Oct. 2003.
- [121] S. Okuyama, S. I. Matsushita, and A. Fujishima, "Periodic Submicrocylinder Diamond Surfaces Using Two-Dimensional Fine Particle Arrays," *Langmuir*, vol.

- 18, no. 22, pp. 8282–8287, 2002.
- [122] B. V. Derjaguin, D. V. Fedoseev, V. M. Lukyanovich, B. V. Spitzin, V. A. Ryabov, and A. V. Lavrentyev, “Filamentary diamond crystals,” *J. Cryst. Growth*, vol. 2, no. 6, pp. 380–384, Dec. 1968.
- [123] V. D. Zamozhskii and A. N. Luzin, “Growth of diamond whiskers observed in an electron microscope,” *Dokl. Akad. Nauk SSSR*, vol. 224, no. 369, 1975.
- [124] V. P. Butuzov, V. A. Laptev, B. I. Dunin, V. P., Zadneprovskii, and N. G. Sanzharlinskii, “Diamond whisker growth in a metal-carbon system at high pressures and temperatures,” *Dokl. Akad. Nauk SSSR*, vol. 225, no. 88, 1975.
- [125] H.-G. Chen and L. Chang, “Characterization of diamond nanoplatelets,” *Diam. Relat. Mater.*, vol. 13, pp. 590–594, 2004.
- [126] E. Ōsawa, M. Yoshida, and M. Fujita, “Shape and Fantasy of Fullerenes,” *MRS Bull.*, vol. 19, no. 11, pp. 33–36, Nov. 1994.
- [127] R. B. Heimann, S. E. Esvukov, and Y. Koga, “Carbon allotropes: a suggested classification scheme based on valence orbital hybridization,” *Carbon N. Y.*, vol. 35, no. 10–11, pp. 1654–1658, Jan. 1997.
- [128] A. Nikitin and Y. Gogotsi, *Nanostructured carbide-derived carbon*, *Encyclopedia of Nanoscience and Nanotechnology*, vol. 7, no. 553–574. CA: American Scientific Publishers, 2004.
- [129] S. K. Gordeev, “Nanoporous and Nanofragmental Carbon Composite Materials,” in *Nanostructured Carbon for Advanced Applications*, Dordrecht: Springer Netherlands, 2001, pp. 71–88.
- [130] S. K. Gordeev, P. I. Belobrov, E. A. Kiselev, N. I., Petrakovskaya, and T. C. Ekstrom, “Novel solid nano diamond/pyrocarbon semiconductor materials,” in *MRS Symp. Proc.*, 2001, p. 63, F14.16.1.
- [131] G. U. Ostrovidova, A. V. Makeev, A. V. Biryukov, and E. Al., “Carbon nanocomposite materials as medicinal depot,” *Mater. Sci. Eng. C*, vol. 23, no. 377,

2003.

- [132] V. Vaijayanthimala *et al.*, “Nanodiamond-mediated drug delivery and imaging: challenges and opportunities,” *Expert Opin. Drug Deliv.*, vol. 12, no. 5, pp. 735–749, May 2015.
- [133] W. Yang *et al.*, “DNA-modified nanocrystalline diamond thin-films as stable, biologically active substrates,” *Nat. Mater.*, vol. 1, no. 4, pp. 253–257, Dec. 2002.
- [134] P. Bajaj *et al.*, “Ultrananocrystalline diamond film as an optimal cell interface for biomedical applications,” *Biomed Microdevices.*, vol. 9, no. 6, pp. 787–794, 2007.
- [135] B. Shi, Q. Jin, L. Chen, and O. Auciello, “Fundamentals of ultrananocrystalline diamond (UNCD) thin films as biomaterials for developmental biology: Embryonic fibroblasts growth on the surface of (UNCD) films.,” *Diam Relat Mater.*, vol. 18, no. 2–3, pp. 596–600, 2009.
- [136] V. N. Mochalin, O. Shenderova, D. Ho, and Y. Gogotsi, “The properties and applications of nanodiamonds.,” *Nat. Nanotechnol.*, vol. 7, no. 1, pp. 11–23, 2012.
- [137] O. Auciello *et al.*, “Materials science and fabrication processes for a new MEMS technology based on ultrananocrystalline diamond thin films.,” *J Phys Condens Matter.*, vol. 16, no. 16, pp. R539–R552, 2004.
- [138] O. Auciello and A. V Sumant, “Status review of the science and technology of ultrananocrystalline diamond (UNCDTM) films and application to multifunctional devices.,” *Diam Relat Mater.*, vol. 19, no. 7–9, pp. 699–718, 2010.
- [139] K. Turcheniuk and V. N. Mochalin, “Biomedical applications of nanodiamond (Review),” 2017.
- [140] C.-C. Fu *et al.*, “Characterization and application of single fluorescent nanodiamonds as cellular biomarkers.,” *Proc. Natl. Acad. Sci. U. S. A.*, vol. 104, no. 3, pp. 727–32, Jan. 2007.
- [141] R. Kaur and I. Badea, “Nanodiamonds as novel nanomaterials for biomedical applications: Drug delivery and imaging systems,” *Int. J. Nanomedicine*, vol. 8,

- pp. 203–220, 2013.
- [142] M. F. Weng, S. Y. Chiang, N. S. Wang, and H. Niu, “Fluorescent nanodiamonds for specifically targeted bioimaging: application to the interaction of transferrin with transferrin receptor.,” *Diam Relat Mater*, vol. 18, no. 2–3, pp. 587–591, 2009.
- [143] Y.-R. Chang *et al.*, “Mass production and dynamic imaging of fluorescent nanodiamonds,” *Nat. Nanotechnol.* 2008 35, vol. 3, no. 5, p. 284, Apr. 2008.
- [144] F. Neugart *et al.*, “Dynamics of Diamond Nanoparticles in Solution and Cells,” *Nano Lett.*, vol. 7, no. 12, pp. 3588–3591, 2007.
- [145] S.-J. Yu, M.-W. Kang, H.-C. Chang, K.-M. Chen, and Y.-C. Yuş, “Bright Fluorescent Nanodiamonds: No Photobleaching and Low Cytotoxicity,” *J. Am. Chem. Soc.*, vol. 127, no. 50, pp. 17604–17605, 2005.
- [146] I. L. Medintz, H. T. Uyeda, E. R. Goldman, and H. Mattoussi, “Quantum dot bioconjugates for imaging, labelling and sensing,” *Nat. Mater.*, vol. 4, no. 6, pp. 435–446, Jun. 2005.
- [147] B. Cui *et al.*, “One at a time, live tracking of NGF axonal transport using quantum dots,” *Proc. Natl. Acad. Sci.*, vol. 104, no. 34, pp. 13666–13671, Aug. 2007.
- [148] D. Akin *et al.*, “Bacteria-mediated delivery of nanoparticles and cargo into cells,” *Nat. Nanotechnol.*, vol. 2, no. 7, pp. 441–449, Jul. 2007.
- [149] A. Gruber, A. Dräbenstedt, C. Tietz, L. Fleury, J. Wrachtrup, and C. Von, “Scanning Confocal Optical Microscopy and Magnetic Resonance on Single Defect Centers,” vol. 276, no. 5321, pp. 2012–2014, 1997.
- [150] F. Treussart, V. Jacques, E. Wu, T. Gacoin, P. Grangier, and J.-F. Roch, “Photoluminescence of single colour defects in 50 nm diamond nanocrystals,” *Phys. B Condens. Matter*, vol. 376–377, pp. 926–929, Apr. 2006.
- [151] R. Schirhagl, K. Chang, M. Loretz, and C. L. Degen, “Nitrogen-Vacancy Centers in Diamond: Nanoscale Sensors for Physics and Biology,” *Annu. Rev. Phys. Chem.*, vol. 65, no. 1, pp. 83–105, Apr. 2014.

- [152] M. W. Doherty, N. B. Manson, P. Delaney, F. Jelezko, J. Wrachtrup, and L. C. L. Hollenberg, “The nitrogen-vacancy colour centre in diamond,” *Phys. Rep.*, vol. 528, no. 1, pp. 1–45, Jul. 2013.
- [153] S. Osswald, G. Yushin, V. Mochalin, S. O. Kucheyev, and Y. Gogotsi, “Control of sp²/sp³ carbon ratio and surface chemistry of nanodiamond powders by selective oxidation in air,” *J. Am. Chem. Soc.*, vol. 128, pp. 11635–11642, 2006.
- [154] O. Shenderova *et al.*, “Surface chemistry and properties of ozone-purified detonation nanodiamonds,” *J. Phys. Chem. C* 115, 9827–9837, 2011.
- [155] P C I, “Nanodiamonds Bring Diamond Properties to Surface Coatings.” [Online]. Available: <http://www.pcimag.com/articles/99552-nanodiamonds-bring-diamond-properties-to-surface-coatings>.
- [156] Z. Pan, H. Sun, Y. Zhang, and C. Chen, “Harder than diamond: Superior indentation strength of wurtzite BN and lonsdaleite,” *Phys. Rev. Lett.*, vol. 102, no. 5, pp. 1–4, 2009.
- [157] D. Ugarte, “Curling and closure of graphitic networks under electron-beam irradiation,” *Nature*, vol. 359, no. 6397, pp. 707–709, Oct. 1992.
- [158] S. Iijima and T. Ichihashi, “Single-shell carbon nanotubes of 1-nm diameter,” *Nature*, vol. 363, no. 6430, pp. 603–605, Jun. 1993.
- [159] D. S. Bethune *et al.*, “Cobalt-catalysed growth of carbon nanotubes with single-atomic-layer walls,” *Nature*, vol. 363, no. 6430, pp. 605–607, Jun. 1993.
- [160] Thess *et al.*, “Crystalline Ropes of Metallic Carbon Nanotubes,” *Science*, vol. 273, no. 5274, pp. 483–7, Jul. 1996.
- [161] D. M. Gruen, “NANOCRYSTALLINE DIAMOND FILMS,” *Annu. Rev. Mater. Sci.*, vol. 29, no. 1, pp. 211–259, Aug. 1999.
- [162] T.-L. Wee, Y.-W. Mau, C.-Y. Fang, H.-L. Hsu, C.-C. Han, and H.-C. Chang, “Preparation and characterization of green fluorescent nanodiamonds for biological applications,” *Diam. Relat. Mater.*, vol. 18, no. 2–3, pp. 567–573, Feb. 2009.

- [163] Y. Wang *et al.*, “Raman Studies of Monolayer Graphene: The Substrate Effect,” *J. Phys. Chem. C*, vol. 112, pp. 10637–10640, 2008.
- [164] V. V. Danilenko, “On the history of the discovery of nanodiamond synthesis,” *Phys. Solid State*, vol. 46, no. 4, pp. 595–599, 2004.
- [165] P. D. Ownby, “Nano 6H Diamond Polytype Polycrystalline Powder.”
- [166] J. E. Field, *The Properties of Natural and Synthetic Diamond*. London: Academic Press, 1992.
- [167] J.-P. Boudou *et al.*, “High yield fabrication of fluorescent nanodiamonds.”
- [168] Y. Ma, G. Zou, H. Yang, and J. Meng, “Conversion of fullerenes to diamond under high pressure and high temperature,” *Appl. Phys. Lett.*, vol. 65, no. 7, pp. 822–823, Aug. 1994.
- [169] M. N. Regueiro, P. Monceau, and J.-L. Hodeau, “Crushing C60 to diamond at room temperature,” *Nature*, vol. 355, no. 6357, pp. 237–239, Jan. 1992.
- [170] H. Yusa, “Nanocrystalline diamond directly transformed from carbon nanotubes under high pressure,” *Diam. Relat. Mater.*, vol. 11, no. 1, pp. 87–91, Jan. 2002.
- [171] G. W. Yang, J. B. Wang, and Q. X. Liu, “Preparation of nano-crystalline diamonds using pulsed laser induced reactive quenching,” *J. Phys. Condens. Mat.*, vol. 10, pp. 7923–7927, 1998.
- [172] S. . Ogale, A. . Malshe, S. . Kanetkar, and S. . Kshirsagar, “Formation of diamond particulates by pulsed ruby laser irradiation of graphite immersed in benzene,” *Solid State Commun.*, vol. 84, no. 4, pp. 371–373, Oct. 1992.
- [173] C.-H. Nee, S.-L. Yap, T.-Y. Tou, H.-C. Chang, and S.-S. Yap, “Direct synthesis of nanodiamonds by femtosecond laser irradiation of ethanol,” *Sci. Rep.*, vol. 6, no. 1, p. 33966, Dec. 2016.
- [174] F. Banhart and P. M. Ajayan, “Carbon onions as nanoscopic pressure cells for diamond formation,” *Nature*, vol. 382, pp. 433–435, 1996.
- [175] É. Galimov *et al.*, “Experimental corroboration of the synthesis of diamond in the

- cavitation process,” *Dokl. Phys.*, vol. 49, no. 3, pp. 150–153, 2004.
- [176] T. L. Daulton, M. A. Kirk, R. S. Lewis, and L. E. Rehn, “Production of nanodiamonds by high-energy ion irradiation of graphite at room temperature,” *Nucl. Instrum. Meth. B*, vol. 175, pp. 12–20, 2001.
- [177] Y. G. Gogotsi, K. G. Nickel, D. Bahloul-Hourlier, T. Merle-Mejean, G. E. Khomenko, and K. P. Skjerlie, “Structure of carbon produced by hydrothermal treatment of β -SiC powder,” *J. Mater. Chem.*, vol. 6, no. 4, p. 595, 1996.
- [178] L. Chow, A. . Horner, H. Sakouri, B. Roughani, and S. Sundaram, “Growth of (100) oriented diamond thin films on ball structure diamond-like particles,” *J. Mater. Res.*, vol. 7, p. 1606, 1992.
- [179] D. Zhou *et al.*, “Synthesis and electron field emission of nanocrystalline diamond thin films grown from N₂/CH₄N₂/CH₄ microwave plasmas,” *J. Appl. Phys.*, vol. 82, p. 4546, 1997.
- [180] A. D. Zhou, D. M. Gruen, L. C. Qin, T. G. McCauley, and A. R. Krauss, “Control of diamond film microstructure by Ar additions to CH₄/H₂CH₄/H₂ microwave plasmas,” *J. Appl. Phys.*, vol. 84, p. 1981, 1998.
- [181] A. Stacey, I. Aharonovich, S. Praver, and J. E. Butler, “Controlled synthesis of high quality micro/nano-diamonds by microwave plasma chemical vapor deposition,” *Diam. Relat. Mater.*, vol. 18, no. 1, pp. 51–55, 2009.
- [182] J. E. Butler and A. V. Sumant, “The CVD of Nanodiamond Materials,” *Chem. Vap. Depos.*, vol. 14, no. 7–8, pp. 145–160, Jul. 2008.
- [183] L. Chow *et al.*, “Chemical vapor deposition of novel carbon materials,” *Thin Solid Films*, vol. 368, no. 2, pp. 193–197, 2000.
- [184] S. Gottlieb, N. Wöhrle, S. Schulz, and V. Buck, “Simultaneous synthesis of nanodiamonds and graphene via plasma enhanced chemical vapor deposition (MW PE-CVD) on copper,” *Springerplus*, vol. 5, no. 1, 2016.
- [185] M. Panda *et al.*, “Nano scale investigation of particulate contribution to diamond

- like carbon film by pulsed laser deposition,” *RSC Adv.*, vol. 6, pp. 6016–6028, 2016.
- [186] D. Ho, Ed., *Nanodiamonds: Applications in Biology and Nanoscale Medicine*. Springer US., 2010.
- [187] J. Kim, H. Sakakita, H. Ohsaki, and M. Katsurai, “Microwave-excited atmospheric pressure plasma jet with wide aperture for the synthesis of carbon nanomaterials,” *Jpn. J. Appl. Phys.*, vol. 54, no. 1S, p. 01AA02, 2015.
- [188] A. Kumar, P. Ann Lin, A. Xue, B. Hao, Y. Khin Yap, and R. M. Sankaran, “Formation of nanodiamonds at near-ambient conditions via microplasma dissociation of ethanol vapour,” *Nat. Commun.*, vol. 4, p. 2618, 2013.
- [189] Y. K. Liu, P. L. Tso, I. N. Lin, Y. Tzeng, and Y. C. Chen, “Comparative study of nucleation processes for the growth of nanocrystalline diamond,” *Diam. Relat. Mater.*, vol. 15, no. 2–3, pp. 234–238, Feb. 2006.
- [190] Y. Lifshitz *et al.*, “The mechanism of diamond nucleation from energetic species,” *Science*, vol. 297, no. 5586, pp. 1531–3, Aug. 2002.
- [191] A. Dias *et al.*, “ASSEMBLING AND ENGINEERING NANOSTRUCTURES BY MICROWAVE PLASMAS OF,” in *Microwave Discharges: Fundamentals and Applications*, Editorial., A. Gamero and A. Sola, Eds. 2015.
- [192] N. Bundaleska *et al.*, “Microwave plasma enabled synthesis of free standing carbon nanostructures at atmospheric pressure conditions,” *Phys. Chem. Chem. Phys.*, 2018.
- [193] R. F. Egerton, *Physical Principles of Electron Microscopy*. 2005.
- [194] J. Goldstein, *Scanning electron microscopy and x-ray microanalysis*. Kluwer Academic/Plenum Publishers, 2003.
- [195] L. Reimer, *Scanning Electron Microscopy*, vol. 45. Berlin, Heidelberg: Springer Berlin Heidelberg, 1998.
- [196] P. Zinin, “Advanced Techniques in Geophysics and Materials Science.” [Online]. Available:

- <http://www.soest.hawaii.edu/HIGP/Faculty/sksharma/GG711/GG711Lec05SEM.pdf>.
- [197] J. (Jens) Als-Nielsen and D. McMorrow, *Elements of modern X-ray physics*. Wiley, 2011.
- [198] B. E. Warren, *X-ray diffraction*. 1969.
- [199] B. D. Cullity, *Elements of X-RAY DIFFRACTION SECOND EDITION*, 2nd ed. California: Addison-Wesley Publishing Company, Inc., 1978.
- [200] B. D. Ratner, “Advances in the analysis of surfaces of biomedical interest,” *Surf. Interface Anal.*, vol. 23, no. 22, pp. 521–528, 1995.
- [201] Z. Cheng and S. Teoh, “Surface modification of ultra thin poly (epsilon-caprolactone) films using acrylic acid and collagen,” *Biomaterials*, vol. 25, no. 11, pp. 1991–2001, 2004.
- [202] K. E. Sohn, M. D. Dimitriou, J. Genzer, D. A. Fischer, C. J. Hawker, and E. J. Kramer, “Determination of the electron escape depth for NEXAFS spectroscopy,” *Langmuir*, vol. 25, no. 11, pp. 6341–6348, 2009.
- [203] J. Stöhr, *NEXAFS Spectroscopy*, 1st ed. Springer-Verlag Berlin Heidelberg, 1992.
- [204] G. Hähner, “Near edge X-ray absorption fine structure spectroscopy as a tool to probe electronic and structural properties of thin organic films and liquids,” *Chem. Soc. Rev.*, vol. 35, no. 12, pp. 1244–1255, 2006.
- [205] P. R. Griffiths and J. A. De Haseth, *Fourier transform infrared spectrometry*. Wiley-Interscience, 2007.
- [206] K. Nishikida, *Selected applications of modern FTIR techniques*. Gordon & Breach Science Pub, 1995.
- [207] “<https://www.sairem.com/>.” .
- [208] “Brooks instrument website.” [Online]. Available: <https://www.brooksinstrument.com/en/products/accessories-software/secondary-electronics/0250-power-supply>.

- [209] E. Tatarova *et al.*, “Towards large-scale in free-standing graphene and N-graphene sheets,” *Nat. Sci. Reports*, vol. 7, no. 10175, p. (16 pp), 2017.
- [210] “ACSystems.” [Online]. Available: <http://www.acsystems.pt>.
- [211] J. Henriques, E. Tatarova, F. M. Dias, and C. M. Ferreira, “Microwave N₂-Ar plasma torch,” *J. Phys. Conf. Ser.*, vol. 109, pp. 1–11, 2011.
- [212] D. Tsyganov *et al.*, “On the plasma-based growth of ‘flowing’ graphene sheets at atmospheric pressure conditions,” *Plasma Sources Sci. Technol.*, vol. 25, no. 1, p. 015013, 2016.
- [213] E. A. H. Timmermans *et al.*, “Behavior of molecules in microwave-induced plasmas studied by optical emission spectroscopy. 2. Plasmas at atmospheric pressure,” *Spectrochim. acta, Part B At. Spectrosc.*, vol. 54, pp. 1085–1098, 1999.
- [214] J. Luque and D. R. Crosley, “LIFBASE Version 2.0,” 1999. [Online]. Available: www.sri.com/psd/lifbase.
- [215] C. Schmidt, T. Breuer, S. Wippermann, W. G. Schmidt, and G. Witte, “Substrate Induced Thermal Decomposition of Perfluoro-Pentacene Thin Films on the Coinage Metals,” *J. Phys. Chem. C*, vol. 116, pp. 24098–24106, 2012.
- [216] S. Reich and C. Thomsen, “Raman spectroscopy of graphite,” *Phil. Trans. A*, vol. 362, pp. 2271–2288, 2004.
- [217] A. C. Ferrari and D. M. Basko, “Raman spectroscopy as a versatile tool for studying the properties of graphene,” *Nat. Technol.*, vol. 8, pp. 235–246, 2013.
- [218] L. M. Malard, M. A. Pimenta, G. Dresselhaus, and M. S. Dresselhaus, “Raman spectroscopy in graphene,” *Phys. Rep.*, vol. 473, pp. 51–87, 2009.
- [219] A. C. Ferrari, “Raman spectroscopy of graphene and graphite: Disorder, electron–phonon coupling, doping and nonadiabatic effects,” vol. 143, pp. 47–57, 2007.
- [220] G. Beamson and D. Briggs, *High Resolution XPS of Organic Polymers*. New York: Wiley, 1992.
- [221] S. Rondon and P. M. A. Sherwood, “Core level and valence band spectra of PbO

- by XPS,” *Surf. Sci. Spec.*, vol. 5, no. 97, 1998.
- [222] C. Ehlert, W. E. S. Unger, and P. Saalfrank, “C K-edge NEXAFS spectra of graphene with physical and chemical defects,” *Phys. Chem. Chem. Phys.*, vol. 16, pp. 14083–14095, 2014.
- [223] D. A. Fischer, R. M. Wentzcovitch, R. G. Carr, A. Continenza, and A. J. Freeman, “Graphitic interlayer states: A carbon K near-edge x-ray-absorption fine-structure study,” *Physical Review B*, vol. 44, no. 3, pp. 1427–1429, 1991.
- [224] V. Lee, R. V. Dennis, B. J. Schultz, C. Jaye, D. A. Fischer, and S. Banerjee, “Soft X-ray Absorption Spectroscopy Studies of the Electronic Structure Recovery of Graphene Oxide upon Chemical Defunctionalization,” *J. Phys. Chem. C*, vol. 116, no. 38, pp. 20591–20599, 2012.
- [225] R. A. Rosenberg, P. J. Love, and V. Rehn, “Polarization-dependent C(K) near-edge x-ray-absorption fine structure of graphite,” *Phys. Rev. B*, vol. 33, no. 6, 1986.
- [226] P. Girard-lauriault, R. Illgen, J. Ruiz, M. R. Wertheimer, and W. E. S. Unger, “Surface functionalization of graphite and carbon nanotubes by vacuum-ultraviolet photochemical reactions,” *Appl. Surf. Sci.*, vol. 258, no. 22, pp. 8448–8454, 2012.
- [227] W. Zhang, A. Nefedov, M. Naboka, L. Cao, and C. Wöll, “Molecular orientation of terephthalic acid assembly on epitaxial graphene: NEXAFS and XPS study,” *Phys. Chem. Chem. Phys.*, vol. 14, no. 29, p. 10125, 2012.
- [228] S. M. Sze and K. K. Ng, *Physics of semiconductor devices*. Wiley-Interscience, 2007.
- [229] M. Choucair, P. Thordarson, and J. A. Stride, “Gram-scale production of graphene based on solvothermal synthesis and sonication,” *Nat. Nanotech.*, vol. 4, pp. 30–33, 2009.
- [230] Y. Shen and A. C. Lua, “A facile method for the large-scale continuous synthesis of graphene sheets using a novel catalyst,” *Sci. Rep.*, vol. 3, no. 1, p. 3037, Dec.

- 2013.
- [231] J. Henriques, E. Tatarova, F. M. Dias, and C. M. Ferreira, “Microwave N₂-Ar plasma torch. II. Experiment and comparison with theory,” *J. Appl. Phys.*, vol. 109, no. 2, p. 023302, Jan. 2011.
- [232] R. Jung. and J.-K. Cheong, “Investigation of the dependence of the chemical states of the graphene surface on N₂ plasma treatment,” *J. Korean Phys. Soc.*, vol. 60, pp. 933–936, 2012.
- [233] A. Mourato, J. F. Cabrita, A. M. Ferraria, A. M. B. do Rego, and L. M. Abrantes, “Electrocatalytic activity of polypyrrole films incorporating palladium particles,” *Catal. Today*, vol. 158, pp. 2–11, 2010.
- [234] I. Bertoti, M. Mohai, and K. Laszlo, “Surface modification of graphene and graphite by nitrogen plasma: Determination of chemical state alterations and assignments by quantitative X-ray photoelectron spectroscopy,” *Carbon N. Y.*, vol. 84, pp. 185–196, 2015.
- [235] E. Choi *et al.*, “Noncovalent Functionalization of Graphene with End-Functional Polymers,” *J. Mater. Chem.*, vol. 20, pp. 1907–1912, 2010.
- [236] D. Du, P. Li, and J. Ouyang, “Nitrogen-doped reduced graphene oxide prepared by simultaneous thermal reduction and nitrogen doping of graphene oxide in air and its application as an electrocatalyst,” *ACS Appl. Mater. Interfaces*, vol. 7, no. 26952–26958, 2015.
- [237] D. Geng *et al.*, “Nitrogen doping effects on the structure of graphene,” *Appl. Surf. Sci.*, vol. 257, pp. 9193–9198, 2011.
- [238] S. Indrawirawan, H. Sun, X. Duan, and S. Wang, “Low temperature combustion synthesis of nitrogen-doped graphene for metal-free catalytic oxidation,” *J. Mater. Chem. A*, vol. 3, no. 7, pp. 3432–3440, 2015.
- [239] M. Khandelwal and A. Kumar, “One-pot environmentally friendly amino acid mediated synthesis of N-doped graphene–silver nanocomposites with an enhanced

- multifunctional behavior,” *Dalt. Trans.*, vol. 45, no. 12, pp. 5180–5195, 2016.
- [240] M. P. Kumar, T. Kesavan, G. Kalita, P. Ragupathy, T. N. Narayanan, and D. K. Pattanayak, “On the large capacitance of nitrogen doped graphene derived by a facile route,” *RSC Adv.*, vol. 4, pp. 38689–38697, 2014.
- [241] Y. Zhang, Z. Sun, H. Wang, Y. Wang, M. Lianga, and S. Xue, “Nitrogen-doped graphene as a cathode material for dye-sensitized solar cells: effects of hydrothermal reaction and annealing on electrocatalytic performance,” *RSC Adv.*, vol. 5, pp. 10430–10439, 2015.
- [242] J. Henriques, E. Tatarova, F. M. Dias, and C. M. Ferreira, “Microwave N₂-Ar plasma torch,” *J. Phys. Conf. Ser.*, vol. 516, no. 1, 2014.
- [243] N. Bundaleska, D. Tsyganov, R. Saavedra, E. Tatarova, F. M. Dias, and C. M. Ferreira, “Hydrogen production from methanol reforming in microwave ‘tornado’-type plasma,” *Int. J. Hydrogen Energy*, vol. 38, no. 22, pp. 9145–9157, 2013.
- [244] “NIST chemical kinetics database.” [Online]. Available: <http://kinetics.nist.gov>.
- [245] E. Goos, A. Burcat, and B. Ruscic, “Third millennium ideal gas and condensed phase thermochemical database for combustion. TAE Report #867,” Israel.
- [246] M. D. Allendorf and T. M. Besmann, “High temperature thermodynamics database.,” *Sandia National Laboratories*. .
- [247] A. D. McNaught and A. Wilkinson, *IUPAC compendium of chemical terminology*. Oxford: Blackwell Science, 1997.
- [248] M. A. Gigosos and V. J. Cardenoso, “New plasma diagnosis tables of hydrogen Stark broadening including ion dynamics,” *Phys. B At. Mol. Opt. Phys.*, vol. 29, no. 4795, 1996.
- [249] M. A. Gigosos, M. A. González, and V. Cardenoso, “Computer simulated Balmer-alpha, -beta and -gamma Stark line profiles for non-equilibrium plasmas diagnostics,” *Spectrochim. Acta Part B At. Spectrosc.*, vol. 58, no. 8, pp. 1489–1504, 2003.

- [250] A. C. Ferrari and R. John, “Raman spectroscopy of amorphous, nanostructured, diamond-like carbon and nanodiamond,” *Phil. Trans. R. Soc. Lond. A*, vol. 362, no. 1824, pp. 2477–2512, 2004.
- [251] J. K. McDonough and Y. Gogotsi, “Carbon Onions: Synthesis and Electrochemical Applications.”
- [252] E. Tatarova, J. Henriques, F. M. Dias, and C. M. Ferreira, “Large-scale Ar and N₂ – Ar microwave,” *J. Phys. D Appl. Phys.*, vol. 39, pp. 2747–2753, 2006.
- [253] J. Henriques *et al.*, “Spatial structure of a slot-antenna excited microwave N₂ – Ar plasma source,” *J. Appl. Phys.*, vol. 103, no. 103304, p. (12pp), 2008.
- [254] C. M. Ferreira, E. Tatarova, J. Henriques, and F. M. Dias, “A Large-Volume N₂-Ar Microwave Plasma Source Based on Surface Waves,” *Vacuum*, vol. 76, pp. 343–346, 2004.
- [255] E. Tatarova, F. M. Dias, J. Henriques, and C. M. Ferreira, “A large-scale Ar plasma source excited by a TM₃₃₀ mode,” *IEEE Trans. Plasma Sci.*, vol. 33, no. 2 III, pp. 866–875, 2005.
- [256] C. D. Wagner, L. E. Davis, V. M. Zeller, J. A. Taylor, R. H. Raymond, and L. H. Gale, “Empirical Atomic Sensitivity Factors for Quantitative Analysis by Electron Spectroscopy for Chemical Analysis,” *Surf. Interface analysis*, vol. 3, no. 5, 1981.
- [257] S. Doniach and M. Sunjic, “Many-electron singularity in X-ray photoemission and X-ray line spectra from metals,” *J. Phys. C Solid State Phys.*, vol. 3, pp. 285–291, 1970.
- [258] P. R. Kidambi *et al.*, “Observing Graphene Growth: Catalyst – Graphene Interactions during Scalable Graphene Growth on Polycrystalline Copper,” *Nano Lett.*, vol. 13, pp. 4769–4778, 2013.
- [259] P. J. Arias-Monje, S. K. Menon, H. Zea, S. Osswald, and C. C. Luhrs, “Nitrogen Doped Graphene Generated by Microwave Plasma and Reduction Expansion Synthesis,” *Nanosci. Nanotechnol. Lett.*, vol. 8, no. 2, pp. 120–128, 2016.

- [260] A. C. Ferrari *et al.*, “Raman Spectrum of Graphene and Graphene Layers,” vol. 187401, no. NOVEMBER, pp. 1–4, 2006.
- [261] M. A. Pimenta, G. Dresselhaus, M. S. Dresselhaus, and L. G. Canc, “Studying disorder in graphite-based systems by Raman spectroscopy,” *Phys. Chem. Chem. Phys.*, vol. 9, pp. 1276–1291, 2007.
- [262] N. Soin *et al.*, “No Title,” *J. Phys. Chem. C*, vol. 115, pp. 5366–5372, 2011.
- [263] C. Ronning, H. Feldermann, R. Merk, H. Hofsäss, and P. Reinke, “Carbon nitride deposited using energetic species: A review on XPS studies,” *Phys. Rev. B - Condens. Matter Mater. Phys.*, vol. 58, no. 4, pp. 2207–2215, 1998.
- [264] J. T. Titantah and D. Lamoen, “Carbon and nitrogen 1s energy levels in amorphous carbon nitride systems: XPS interpretation using first-principles,” *Diam. Relat. Mater.*, vol. 16, no. 3, pp. 581–588, 2007.
- [265] X. Cao and R. J. Hamers, “Molecular and dissociative bonding of amines with the Si-(7×7) surface,” *Surf. Sci.*, vol. 523, pp. 241–251, 2003.
- [266] D. W. Zeng and K. C. Yung, “XPS investigation on Upilex-S polyimide ablated by pulse TEA CO₂ laser,” *Appl. Surf. Sci.*, vol. 180, no. 3–4, pp. 280–285, 2001.
- [267] N. Li, Z. Wang, K. Zhao, Z. Shi, Z. Gu, and S. Xu, “Large scale synthesis of N-doped multi-layered graphene sheets by simple arc-discharge method,” *Carbon N. Y.*, vol. 48, no. 1, pp. 255–259, Jan. 2010.
- [268] T. Kuilla, S. Bhadra, D. Yao, N. H. Kim, S. Bose, and J. H. Lee, “Recent advances in graphene based polymer composites,” *Prog. Polym. Sci.*, vol. 35, pp. 1350–1375, 2010.
- [269] J. R. Potts, D. R. Dreyer, C. W. Bielawski, and R. S. Ruoff, “Graphene-based polymer nanocomposites,” *Polymer (Guildf.)*, vol. 52, no. 1, pp. 5–25, 2011.
- [270] J. Zheng, X. Ma, X. He, M. Gao, and G. Li, “Preparation, characterizations, and its potential applications of PANi/ graphene oxide nanocomposite,” *Procedia Eng.*, vol. 27, no. 2011, pp. 1478–1487, 2012.

- [271] D. J. Joe *et al.*, “Surface Functionalized Graphene Biosensor on Sapphire for Cancer Cell Detection,” *J Nanosci Nanotechnol.*, vol. 16, no. 1, pp. 144–151, 2016.
- [272] P. Girard-lauriault, T. Gross, A. Lippitz, and W. E. S. Unger, “Chemical and Elemental Depth Profiling of Very Thin Organic Layers by Constant Kinetic Energy XPS: A New Synchrotron XPS Analysis Strategy,” *Appl. Surf. Sci.*, vol. 258, no. May, pp. 8448–8454, 2012.
- [273] P.-L. Girard-Lauriault, J.-C. Ruiz, T. Gross, M. R. Wertheimer, and W. E. S. Unger, “Ultra-Shallow Chemical Characterization of Organic Thin Films Deposited by Plasma and Vacuum-Ultraviolet, Using Angle- and Excitation Energy-Resolved XPS,” *Plasma Chem Plasma Process*, vol. 31, pp. 535–550, 2011.
- [274] G. G. Wallace, R. B. Kaner, M. Muller, S. Gilje, D. Li, and D. Li, “Processable aqueous dispersions of graphene nanosheets Publication Details Processable aqueous dispersions of graphene nanosheets,” *Nat. Nanotechnol.*, vol. 3, no. 2, pp. 101–105, 2008.
- [275] E. Kovačević *et al.*, “Formation and material analysis of plasma polymerized carbon nitride nanoparticles,” *J. Appl. Phys.*, vol. 105, no. 10, p. 104910, 2009.
- [276] J. Berndt, H. Acid, E. Kovacevic, C. Cachoncinlle, T. Strunskus, and L. Boufendi, “Deposition and tuning of nanostructured hydrocarbon deposits: From superhydrophobic to superhydrophilic and back,” *J. Appl. Phys.*, vol. 113, no. 063302, 2013.
- [277] C. Pattyn, E. Kovacevic, S. Hussain, A. Dias, T. Lecas, and J. Berndt, “Nanoparticle formation in a low pressure argon / aniline RF plasma,” *Appl. Phys. Lett.*, vol. 013102, no. 112, 2018.
- [278] E. Kovacevic, I. Stefanovic, J. Berndt, and J. Winter, “Infrared fingerprints and periodic formation of nanoparticles in Ar/C₂H₂ plasmas,” *J. Appl. Phys.*, vol. 93, no. 2924, 2003.
- [279] Y. Wang *et al.*, “Surface-Energy Engineering of Graphene Surface energy

- engineering of graphene,” *Langmuir*, vol. 26, no. 6, pp. 3798–3802, 2010.
- [280] N. Mcevoy, T. Hallam, N. Mcevoy, H. Nolan, and G. S. Duesberg, “Functionalization of graphene surfaces with downstream plasma treatments plasma treatments,” no. February 2016, 2013.
- [281] P. T. Araujo, M. Terrones, and M. S. Dresselhaus, “Defects and impurities in graphene-like materials,” *Mater. Today*, vol. 15, no. 3, pp. 98–109, 2012.
- [282] M. J. Webb, P. Palmgren, P. Pal, O. Karis, and H. Grennberg, “A simple method to produce almost perfect graphene on highly oriented pyrolytic graphite,” *Carbon N. Y.*, vol. 49, p. 3242, 2011.
- [283] W. Shen, Z. Li, and Y. Liu, “Surface Chemical Functional Groups Modification of Porous Carbon,” *Recent Patents Chem. Eng. 2008*, vol. 1, pp. 27–40, 2008.
- [284] P.-L. Girard-Lauriault, P. Dietrich, T. Gross, and W. E. S. Unger, “Is quantitative chemical derivatization XPS of plasma deposited organic coatings a valid analytical procedure,” *Surf. Interface Anal.*, vol. 44, pp. 1135–1140, 2012.
- [285] J. W. Chiou *et al.*, “Nitrogen-Functionalized Graphene Nano flakes (GNFs : N) : Tunable Photoluminescence and Electronic Structures,” *J Phys Chem C*, vol. 116, no. 30, pp. 16251–16258, 2012.
- [286] Y. Zheng *et al.*, “Hydrogen evolution by a metal-free electrocatalyst Hydrogen evolution by a metal-free electrocatalyst,” *Nat. Commun.*, vol. 5, no. November, pp. 1–8, 2014.
- [287] J. T. Francis and A. P. Hitchcock, “Inner-shell spectroscopy of pbenzoquinone, hydroquinone, and phenol: distinguishing quinoid and benzenoid structures.,” *J Phys Chem*, vol. 96, pp. 6598–610, 1992.
- [288] H. K. Jeong, J. H. Noh, K. J Y, M. H. Jin, C. Y. Park, and Y. H. Lee, “X-ray absorption spectroscopy of graphite oxide.,” *Eur. Lett*, vol. 82, pp. 67004–1–5, 2008.
- [289] J. C. Meyer *et al.*, “Electronic properties and atomic structure of graphene oxide

- membranes,” *Carbon N. Y.*, vol. 49, pp. 966–972, 2011.
- [290] A. Ganguly, S. Sharma, P. Papakonstantinou, and J. Hamilton, “Probing the Thermal Deoxygenation of Graphene Oxide using High Resolution In Situ X-Ray based Spectroscopies,” *J. Phys. Chem. C*, vol. 115, no. 34, pp. 17009–17019, 2011.
- [291] H. Yabuta *et al.*, “X-ray absorption near edge structure spectroscopic study of Hayabusa category 3 carbonaceous particles X-ray absorption near edge structure spectroscopic study of Hayabusa category 3 carbonaceous particles,” *Earth, Planets Sp.*, vol. 66, no. 156, 2014.

List of Abbreviations

ATP – Aerosol-Through-Plasma
CCP – Capacitively Coupled Plasma
CVD – Chemical Vapor Deposition
DRX – Difração de Raios X
FSG(s) – Free-standing graphene (sheets)
FTIR – Fourier-transform Infrared Spectroscopy
GREMI - Groupe de Recherches sur l'Energétique des Milieux Ionisés
HOPG – Highly Oriented Pyrolytic Graphite
HRTEM – High-Resolution Transmission Electron Microscopy
IPFN – Instituto de Plasmas e Fusão Nuclear
MW – Microwaves
N-5 – Pyrrolic Nitrogen
N-6 – Pyridinic Nitrogen
N-Q – Quaternary Nitrogen
NG, N-graphene – Nitrogen-doped graphene
ND - Nanodiamond
NCD – Nanocrystalline Diamond
NEXAFS – Near Edge X-ray Absorption Fine Structure
N-V – Nitrogen Vacancy
OES – Optical Emission Spectroscopy
PECVD - Plasma Enhanced Chemical Vapor Deposition
PEL – Plasma Engineering Laboratory
PG – Pristine Graphene
RF – Radio Frequency
SAED – Selected Area Electron Diffraction
SEM – Scanning Electron Microscopy
TEM – Transmission Electron Microscopy
UNCD – Ultrananocrystalline Diamond
XPS – X-ray Photoelectron Spectroscopy
XRD – X-ray Diffraction

Ana Inês VIEITAS DE AMARAL DIAS

Plasmas appliqués à la production de nanostructures de carbone avancées

Résumé :

L'environnement réactif du plasma constitue un outil puissant dans la science des matériaux, permettant la création de matériaux innovatifs et l'amélioration de matériaux existants qui ne serait autrement pas possible. Le plasma fournit simultanément des fluxes de particules chargées, des molécules chimiquement actives, des radicaux, de la chaleur, des photons, qui peuvent fortement influencer les voies d'assemblage à différentes échelles temporelles et spatiales, y compris à l'échelle atomique.

Dans cette thèse de doctorat, des méthodes tenant pour base des plasmas micro-ondes ont été utilisées pour la synthèse de nanomatériaux de carbone, y compris graphène, graphène dopé à l'azote (N-graphène) et structures de type diamant.

À cette fin, ce travail est lié à l'optimisation de la synthèse de nanostructures 2D du carbone, comme graphène et N-graphène par la poursuite de l'élaboration et du raffinement de la méthode développée en *Plasma Engineering Laboratory* (PEL). La synthèse de graphène de haute qualité et en grandes quantités a été accomplie avec succès en utilisant des plasmas d'Ar-éthanol à ondes de surface dans des conditions de pression ambiante. De plus, le N-graphène a été synthétisé par un procédé en une seule étape, de l'azote a été ajouté au mélange d'Ar-éthanol, et par un procédé en deux étapes, en soumettant des feuilles de graphène préalablement synthétisées ont été exposées à un traitement plasma argon-azote à basse pression. Les atomes d'azote ont été incorporés avec succès dans le réseau de graphène hexagonal, formant principalement liaisons pyrroliques, pyridiniques et quaternaires. Un niveau de dopage de 25 at.% a été atteint. Différents types de nanostructures de carbone, y compris du graphène et des structures de type diamant, ont été synthétisées au moyen d'un plasma d'argon en utilisant du méthane et du dioxyde de carbone comme précurseurs du carbone.

De plus, des plasmas à couplage capacitif ont également été utilisés pour la fonctionnalisation du graphène et pour la synthèse de nanocomposites, tels que les composites de Polyaniline (PANI)-graphène. Les utilisations potentielles de ces matériaux ont été étudiées et les deux structures ont démontré avoir des attributs remarquables pour leur application aux biocapteurs.

Mots clés : Nanostructures de carbone, plasma à basse température, nanocomposites polymère-graphène, structures de type diamant, graphène

Plasma based assembly and engineering of advanced carbon nanostructures

Abstract:

Plasma environments constitute powerful tools in materials science by allowing the creation of innovative materials and the enhancement of long existing materials that would not otherwise be achievable. The remarkable plasma potential derives from its ability to simultaneously provide dense fluxes of charged particles, chemically active molecules, radicals, heat and photons which may strongly influence the assembly pathways across different temporal and space scales, including the atomic one.

In this thesis, microwave plasma-based methods have been applied to the synthesis of advanced carbon nanomaterials including graphene, nitrogen-doped graphene (N-graphene) and diamond-like structures.

To this end, the focus was placed on the optimization of the production processes of two-dimensional (2D) carbon nanostructures, such as graphene and N-graphene, by further elaboration and refinement of the microwave plasma-based method developed at the Plasma Engineering Laboratory (PEL). The scaling up of the synthesis process for high-quality graphene using surface-wave plasmas operating at atmospheric pressure and argon-ethanol mixtures was successfully achieved. Moreover, N-graphene was synthesized via a single-step process, by adding nitrogen to the argon-ethanol mixture, and via two-step process, by submitting previously synthesized graphene to the remote region of a low-pressure argon-nitrogen plasma. Nitrogen atoms were usefully incorporated into the hexagonal graphene lattice, mainly as pyrrolic, pyridinic and quaternary bonds. A doping level of 25% was attained.

Different types of carbon nanostructures, including graphene and diamond-like nanostructures, were also produced by using methane and carbon dioxide as carbon precursors in an argon plasma.

Additionally, capacitively-coupled radio-frequency plasmas have been employed in the functionalization of graphene and in the synthesis of Polyaniline (PANI)-graphene composites. The potential uses of these materials were studied, with both showing favourable characteristics for their applicability in biosensing applications.

Keywords: Free-standing carbon nanostructures, Low temperature plasma, Polymer-graphene nanocomposites, Diamond-like structures, Graphene.

